Generation of phase controlled single photons

Travers Ward

Submitted for the degree of Doctor of Philosophy

University of Sussex

September 2022

Declaration

I hereby declare that this thesis has not been and will not be submitted in whole or in part to another University for the award of any other degree.

Signature:

Travers Ward

UNIVERSITY OF SUSSEX

Travers Ward, Doctor of Philosophy

Generation of phase controlled single photons

Summary

Quantum computing and networking is a rapidly evolving area of research. Quantum computing has many potential uses ranging from material science to biology as well as developing new forms of intelligent AI. Quantum networking meanwhile, is needed to link these future processors together. Furthermore, it is the next big step in terms of digital security, with the very real possibility that current encryption methods are close to being broken, quantum networking allows us to develop protocols that are resistant to the flaws to classical techniques. A promising candidate for quantum networking platform is the trapped ion. Quantum states are easily manipulated and stored in the electronic states of ions, meanwhile, coupling the ion to an optical cavity allows us to map these states onto photons and transfer this information over great distances. In this thesis a brief overview of the ion trap and associated systems, such as frequency references and laser stabilisation techniques are described. The general theory for a Calcium ion coupled to a bimodal cavity is also presented. Furthermore, the necessary theoretical descriptions to understand experimental results is also given.Two experiments are performed, the first of which aims to drastically improve the indistinguishability of generated single photons by implementing a novel scheme that reduces the detrimental effects of spontaneous emission, this result directly links to the fidelity of performed operations. The second experiment demonstrates the systems use as a source of time-bin encoded photons, and compares the new scheme introduced in experiment one against a typically implemented one, to show this technique is only plausible with trapped ions using our novel scheme. These two experiments represent significant progress towards building a quantum network with trapped ions and are pre-requisites for future experiments involving entanglement of photons and ions, as well as ion-ion entanglement between remote traps.

For Nan and Grandad

Acknowledgements

Completing a PhD is one of the most challenging experiences many people will face throughout their lifetime. For me, this was two-fold, a global pandemic seriously hindered progress for a large portion of time. I also became a father (twice!). With these delays and extra responsibilities, finishing my doctoral work on time is one of my proudest achievements. This wouldn't have been possible without my amazing family, friends and colleagues.

I would first like to thank my supervisor, Matthias Keller. He has been an excellent guiding hand and mentor, who I have learnt much from. I am especially grateful for his patience and understanding, allowing me to put my family first when they needed me most. It has been an absolute pleasure working with you.

Next, I'd like to thank all my colleagues at ITCM. Every one of you has helped me at some point in this journey, which I an truly grateful for. I would like to say special thanks to both Samir Vartabi Kashanian and Tom Walker, who took me in and taught me everything I needed to know. I hope you both are enjoying the journeys you set out on.

I would also like to thank my mother, Irene. I wouldn't be the person I am today without you. Your care, love and attention meant far more to me than anything ever could. My grandparents, John and Olive Ward deserve special thanks. There selflessness and love for everyone is a true inspiration and drives me to be a better person every single day. I love you both dearly, you are sorely missed.

Finally, I would like thank my amazing wife, Agathe. You kept me going through the rough times, giving me a reason to push forward. You have given me the single best gift anyone could receive, two beautiful daughters, Alice and Tiffany, with a baby boy on the way in a couple of months! Thank you for being with me during this journey, none of this would be possible without you. Here's to the next adventure together!

Contents

List of Figures

Chapter 1

Introduction

The emergence of quantum mechanics over the last century has had a profound impact on many and very different disciplines, and is one of the most significant developments in modern scientific history. Areas of study that were once thought of as purely classical have been redefined with many new discoveries, such as in astrophysics [5, 6], biology [7] and material science [8]. Pioneering new technologies have also broken through, with just a few examples being quantum sensors, such as brain scanning magnetometers [9], quantum dot displays [10] and the application of quantum physics in the design of new computer processors and memory [11] is essential to continue shrinking process nodes.

The idea of quantum computers was first constructed in the 1980s [12] and has since accelerated as a field of research. Quantum computation builds off the idea of using small quantum systems to form quantum bits (qubits) analogous to a classical bit. These qubits however, can exist in a superposition of its two states unlike their classical counterparts. Many qubits may then be entangled with each other and gate operations implemented in order to perform computations. The intrinsically quantum properties allow access to a rich space of algorithms that are not performable on a regular computer. An early example of this, and arguably the source of the rapid expansion of the field is the demonstration of a quantum algorithm for factorising primes by Peter Shor [13]. Factorising algorithms like this, implemented using quantum computers provide a path for breaking digital security such as RSA encryption. Since this, many more quantum algorithms have been developed, including simulating chemical reactions [14] and advances in protein folding simulation [15].

Another important aspect of the field is quantum networking, which allows the transmission of quantum information over large distances [16, 17] or between interconnected processors allowing for larger qubit arrays [18]. To be a viable node, a system must fulfil certain requirements as described by DiVincenzo in 2000 [19]. Firstly, it must be a physical system that can be isolated from the surrounding environment and contain well defined two-level quantum systems (qubits), which can represent computational basis states $|0\rangle$ and $|1\rangle$. Secondly, it must be possible to initialise or state prepare the system into a well defined initial state. Third, the qubit decoherence times must be longer than the gate operational times. Next, the system must be able to perform a set of universal gates on the qubits or sets of qubits for larger qubit sized gates. Lastly, the qubit state should be readout with high accuracy. These features are most commonly used to benchmark a systems use as a quantum processor. However, in addition to these criteria, quantum nodes used for networking must also fulfil two extra conditions. You must be able to convert between a stationary qubit and a flying qubit, as well as transmitting the flying qubit while maintaining coherence.

Trapped ion cavity quantum electrodynamics (CQED) is one of only a few qubit modalities that satisfy all of the above criteria. Quantum information can be stored in trapped ions through their internal electronic state, this has been demonstrated with preparation and readout fidelities of ($> 99.9\%$) and has been performed in less than 1 ms with coherence times on the order of minutes [20, 21, 22]. Universal high fidelity quantum gates have also been demonstrated, including single and two qubit gates [23, 24]. Trapped ions are also useful for producing and converting flying qubits, in this case photons, which can have quantum information encoded in their polarisation, frequency, phase or arrival time. The photons are easily coupled into standard optical fibres and can be transported to other systems to be read out or used to perform other tasks, such as entangling ions between remote traps. To improve the efficiency and control over the photon collection process, optical cavities can be used. By using a high-finesse optical cavity, the ion-cavity coupling strength can greatly increase photon collection rates while granting greater control, such as frequency selection. The cavity can be used to perform cavity assisted Raman transitions for single photon generation. The output mode of the cavity can then be easily matched to a single-mode fibre, allowing transport. For photons produced in the optical part of the spectrum, the attenuation of optical fibres leads to significant losses, it is therefore essential that for long distance communication, protocols exist to convert optical photons to the telecom band to alleviate this loss, this has already been shown in different systems with little to no loss of the desired quantum properties [25, 26, 27].

Deterministic networking, where quantum information can be transferred between nodes with near unity probability [28] would require access to the strong coupling regime of ion-cavity interactions. The dielectric mirrors significantly affect the trapping potential seen by the ion, causing the mirrors to be placed further from the ion's position and reducing the coupling strength into the weakly coupled regime. While strong coupling in an ion-cavity system has been shown [29], it remains technically challenging and weakly coupled systems remain easier to use and implement. For neutral atoms, where strong coupling is easier to achieve, quantum state transfer has already occurred [30]. For this reason, probabilistic entanglement schemes have been developed, where unity efficiency is no longer required and may be retried until an entanglement is heralded by photon detection [16, 31]. In these protocols, speed is sacrificed for simplicity and high fidelities can be achieved with systems that have low success probabilities. Recently, 94% entanglement fidelity between two strontium ions [32] has been achieved. In this case, the photons were collected with high numerical aperture lenses before being coupled into the fibre. The efficiency of this setup is restricted by the solid angle of the lens and difficult mode matching to the fibre. With an ion-cavity experiment, this loss of efficiency is negated and better coupling efficiencies to the fibre can also be obtained.

In this thesis, a trapped ion CQED system is described and its use as a node in a quantum network is discussed. Two experiments were performed, one seeking to improve the indistinguishability of the single photons generated using a novel single-photon generation scheme and another to demonstrate the possibility of using this generation scheme in time-bin-phase encoding, useful in many communication protocols, including quantum key distribution [33, 34, 35]. In chapter two, the system Hamiltonian is derived along with the dissipative processes necessary for simulating the system. The correlation functions needed to assess the photon statistics in both experiments are also described. Chapter three describes the experimental setup, this includes the ion trap and its associated parameters, the laser systems and the frequency stabilisation techniques used. Chapter four covers the first experiment, whereby careful selection of our initial state can lead to drastic improvements in the indistinguishability of the single photons generated. This indistinguishability directly relates to the fidelity of networking operations and entanglements. Chapter five describes the implementation of a time-bin-phase encoding technique, where the ion trap system replaces the typical Mach-Zehnder interferometer for producing time-bins in single photons. By measuring an applied phase to one of the time-bins, we can demonstrate the ability to produce arbitrary qubit states, typically used by Quantum key distribution protocols. The final chapter summarises these findings and introduces future work.

Chapter 2

Theory

In this chapter the dynamics of the $^{40}\mathrm{Ca}^{+}$ ion and its interaction with a bimodal optical cavity are described. In-depth descriptions of two and three-level systems, cavity-QED (Jaynes-Cummings model) and single photon generation can be found in the previous theses for this trap [3, 4, 1] as well as many textbooks. This chapter will focus on forming the Hamiltonian's required for numerical simulations and how they are performed. The simulations are written in Python using the Quantum Optics Toolbox (QuTiP) [36]. A short explanation of photon correlation functions is also discussed. These are later used to describe the interference patterns observed in the two experiments presented in this thesis.

2.1 $^{40}\mathrm{Ca}^{+}$

In this section the necessary level scheme for understanding the generation of single photons in $^{40}\mathrm{Ca}^{+}$ is described. The reduced level scheme for $^{40}\mathrm{Ca}^{+}$ is shown in Fig. 2.1, this simplified scheme contains all the necessary levels to describe the single photon generation processes. The metastable $\mathrm{D}_{3/2}$ state has a lifetime of approximately one second and is therefore of no consequence to the generation schemes used in this thesis. The cavity is designed for use with the $\mathrm{D}_{3/2} \leftrightarrow \mathrm{P}_{1/2}$ transition. This transition is chosen because high-finesse UV cavities are far more difficult to produce and use than IR ones. Choosing this transition also gives us access to the rich Zeeman structure of the $\mathrm{D}_{3/2}$ level.

Taking the dipole approximation, a classical monochromatic electric field polarised along $\boldsymbol{\epsilon}$ may be written as

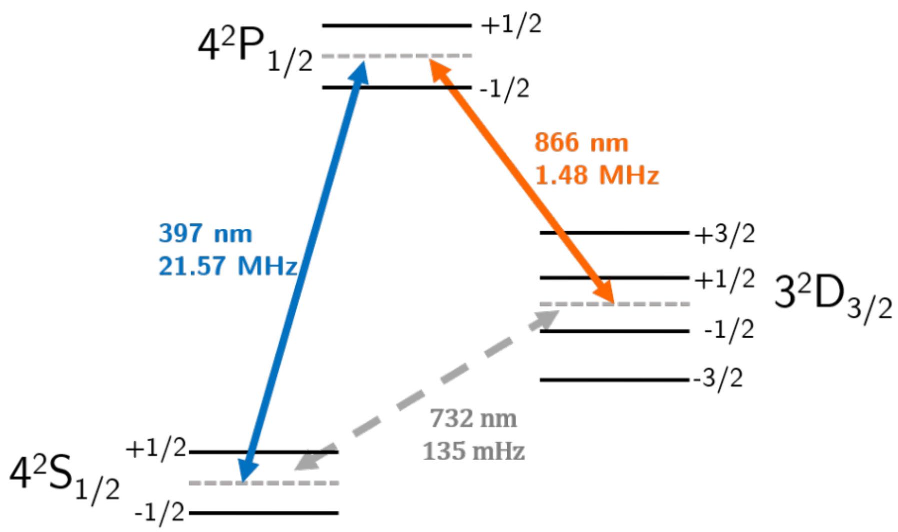

Figure 2.1: 8-Level energy scheme for $^{40}Ca^+$. An applied magnetic field causes splitting between the Zeeman sublevels. Transition wavelengths and linewidths ($\Gamma/2\pi$) are shown. Image from [1].

$$\boldsymbol{E}(t) = \boldsymbol{\epsilon} E_0 (e^{i\omega_L t} + e^{-i\omega_L t}) \tag{2.1}$$

where E_0 is the amplitude of the field at the position of the atom and ω_L is the angular frequency of the light. The electric dipole interaction between the ion and a laser is

$$\hat{H}_I = -\hat{\mathbf{d}} \cdot \mathbf{E}(t) \tag{2.2}$$

where the dipole $\hat{\boldsymbol{d}} = -q\hat{\boldsymbol{r}}$, with the elementary charge q and the dipole position operator $\hat{\boldsymbol{r}}$.

As the experiments performed in this thesis require magnetic fields to lift the degeneracy of the Zeeman sublevels, it is necessary to describe the amount of splitting with relation to the strength of the magnetic field. For the levels shown in Fig.2.1, each contains 2J + 1 Zeeman sublevels $|J, m_j\rangle$. The splitting between each level is then

$$\Delta E_{J,m_j} = m_J g_J \mu_B B \tag{2.3}$$

where μ_B is the Bohr magneton and g_J is the Landé g-factor. When $\Delta E_{J,m_j}$ is greater than the sum of the cavity, laser and transition linewidths, Raman transitions between individual Zeeman sublevels are achievable.

When a magnetic field is applied to the ion and the Zeeman sublevels are split, the electric dipole interaction has to be modified. This factor depends on both J and m_J and are called Clebsch-Gordan coefficients. This factor governs what polarisation of light may

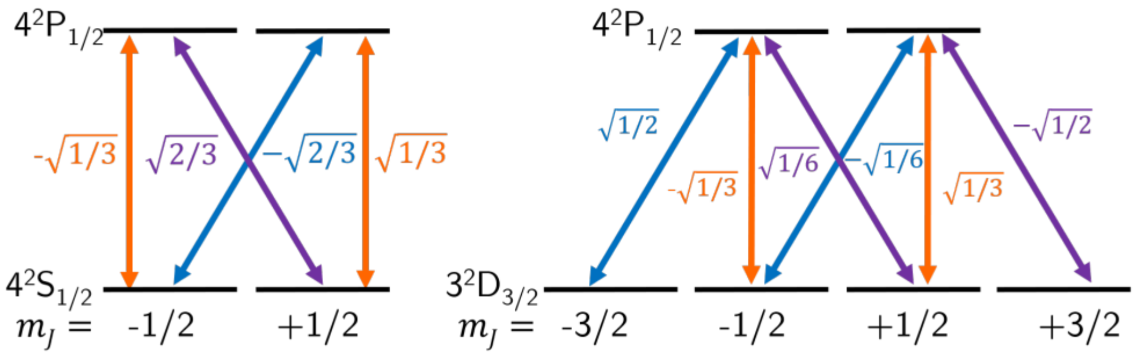

Figure 2.2: Clebsch-Gordan coefficients for relevant transitions in $^{40}\mathrm{Ca}^+$. Transition polarisation indicated by colour: blue = σ^+, purple = σ^- and orange = π. Data originally obtained from [2]. Image from [1].

interact with a transition as well as the relative strength. The relevant Clebsch-Gordan coefficients for $^{40}\mathrm{Ca}^+$ are shown in Fig 2.2. The polarisation of light depends on the atomic frame of reference. In this thesis, the magnetic field is aligned along the cavity axis (z-direction), as such the cavity only couples to $\sigma^{\pm}$ transitions.

2.2 Ion-Cavity Interaction Hamiltonian

In this section the interaction Hamiltonian for the eight level system coupled to a bimodal cavity will be described. The relevant dissipation processes will also be presented.

For a two level system, the cavity field Hamiltonian is

$$\hat{H}_{\text{cavfield}} = \hbar\omega_c \left(\hat{a}^\dagger \hat{a} + \frac{1}{2}\right) \tag{2.4}$$

Where ω_c is the frequency. This is the form of a quantum harmonic oscillator. The factor of $\frac{1}{2}$ is known as the vacuum energy and can removed by shifting our reference energy by $\frac{\hbar\omega_c}{2}$.

We can write the electric field as a function of position

$$\hat{\boldsymbol{E}}(\boldsymbol{r},t) = \sum_{\boldsymbol{k},\nu} \sqrt{\frac{\hbar}{2\omega_{\boldsymbol{k}}\varepsilon_0 V}} \boldsymbol{\epsilon}_\nu u(\boldsymbol{r}) \left(\hat{a}_{\boldsymbol{k}} e^{-i(\omega_{\boldsymbol{k}} t - \boldsymbol{k}\cdot\boldsymbol{r})} + \hat{a}^\dagger_{\boldsymbol{k}} e^{i(\omega_{\boldsymbol{k}} t - \boldsymbol{k}\cdot\boldsymbol{r})}\right) \tag{2.5}$$

where V is the mode volume, $\hat{a}_k^\dagger$ and $\hat{a}_k$ are the creation and annihilation operators for a wavevector k. u($\boldsymbol{r}$) is the spatial profile of the field and ν gives the polarisation mode of the field.

The interaction Hamiltonian between this field and a two level atom can be written

$$\hat{H}_c = -\hat{\boldsymbol{d}} \cdot \boldsymbol{E}(t) = \hbar \sum_{\boldsymbol{k}} g_{\boldsymbol{k}}(\boldsymbol{r}) \left(\hat{\sigma}^+ + \hat{\sigma}^-\right) \left(\hat{a}_{\boldsymbol{k}} e^{-i\omega_k t} + \hat{a}^\dagger_{\boldsymbol{k}} e^{-i\omega_k t}\right) \tag{2.6}$$

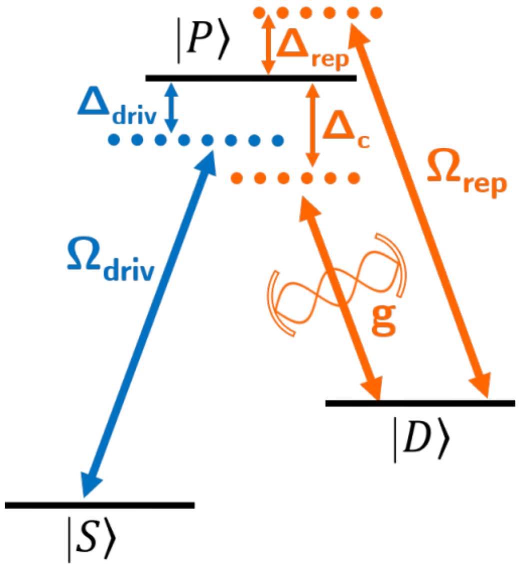

Figure 2.3: Three level atom with states $|S\rangle$ and $|P\rangle$ coupled by a laser with Rabi frequency Ω_{driv} and detuning Δ_{driv}, and states $|P\rangle$ and $|D\rangle$ coupled by a cavity with coupling strength g and detuning Δ_c as well as a laser with Rabi frequency Ω_{rep} and detuning Δ_{rep}. Image from [1].

with a mode coupling strength

$$g_{\boldsymbol{k}}(\boldsymbol{r}) = u(\boldsymbol{r})\sqrt{\frac{k\omega_{\boldsymbol{k}}^2}{2\hbar\varepsilon_0 cV}}\boldsymbol{d}\cdot\boldsymbol{\epsilon} \tag{2.7}$$

By using an optical cavity we can reduce the effective mode volume and significantly increase the coupling of the atom to a single mode of the electric field. By considering only one mode and assuming the atom always sits at the peak of field intensity the interaction Hamiltonian reduces to

$$\hat{H}_c = \hbar g\left(\hat{\sigma}^+ + \hat{\sigma}^-\right)\left(\hat{a}e^{-i\omega_c t} + \hat{a}^\dagger e^{-i\omega_c t}\right) \tag{2.8}$$

As shown in [1] the Hamiltonian for a three-level Λ system (Figure 2.3) composed of ground states $|S\rangle$ and $|D\rangle$ and short lived excited state $|P\rangle$ can be separated as follows

$$\hat{H} = \hat{H}_0 + \hat{H}_{\text{driv}} + \hat{H}_{\text{rep}} + \hat{H}_c \tag{2.9}$$

where $\hat{H}_0$ is the bare Hamiltonian for the system, $\hat{H}_{\text{driv}}$ and $\hat{H}_{\text{rep}}$ are the interaction Hamiltonians between laser and ion for the $|S\rangle \leftrightarrow |P\rangle$ and $|D\rangle \leftrightarrow |P\rangle$ respectively and $\hat{H}_c$ is the cavity interaction.

Using the rotating wave approximation the Hamiltonians can be written as

$$\hat{H}_0 = \hbar\left(\Delta_{\text{driv}}\hat{\sigma}_{SS} + \Delta_{\text{rep}}\hat{\sigma}_{DD} + (\Delta_c - \Delta_{\text{rep}})\,\hat{a}^\dagger\hat{a}\right) \tag{2.10}$$

$$\hat{H}_{\text{driv}} = \frac{\hbar\Omega_{\text{driv}}}{2}\hat{\sigma}_{SP} + \text{ h.c.} \tag{2.11}$$

$$\hat{H}_{\text{rep}} = \frac{\hbar\Omega_{\text{rep}}}{2}\hat{\sigma}_{DP} + \text{ h.c.} \tag{2.12}$$

$$\hat{H}_{c} = \hbar g\left(\hat{a}^{\dagger}\hat{\sigma}_{DP} + \hat{a}\hat{\sigma}^{\dagger}_{PD}\right) \tag{2.13}$$

where the atomic raising and lowering operators $\sigma_{i,j} = |i\rangle\langle j|$ have been introduced and Ω_{driv}, Ω_{rep} and g represent the coupling strength. Δ_{driv}, Δ_{rep} and Δ_{c} represent the laser and cavity detunings. In this case the Hamiltonian has been referenced to the energy of the excited state E_p.

We now include the effect of an applied magnetic field splitting the Zeeman sublevels. Firstly, we shall split the bare Hamiltonian $\hat{H}_0$ into it's atomic and cavity components.

$$\hat{H}_0 = \hat{H}_{0,\text{ atom}} + \hat{H}_{0,\text{ cav}} \tag{2.14}$$

The bare ion Hamiltonian with added Zeeman splitting then becomes

$$\hat{H}_{0,\text{ atom}} = \hat{H}_S + \hat{H}_D + \hat{H}_P \tag{2.15}$$

To describe the Zeeman sublevels we introduce new atomic operators $\sigma_{A,m_a;B,m_b} = |A, m_a\rangle\langle B, m_b|$ so

$$\hat{H}_S = \hbar\sum_{m_J}\left(\Delta_{\text{driv}} + m_J g_S \mu_B B\right)\hat{\sigma}_{S,m_J;S,m_J} \tag{2.16}$$

and

$$\hat{H}_D = \hbar\sum_{m_J}\left(\Delta_{\text{driv}} + m_J g_D \mu_B B\right)\hat{\sigma}_{D,m_J;D,m_J} \tag{2.17}$$

and

$$\hat{H}_P = \hbar\sum_{m_J}\left(m_J g_P \mu_B B\right)\hat{\sigma}_{P,m_J;P,m_J} \tag{2.18}$$

where $g_{S,D,P}$ are the Landé g-factors for the respective levels. It is important to include the splitting of the $\text{P}_{1/2}$ levels as it changes the detuning Δ_{driv} between the transitions.

To describe the cavity accurately we need to explicitly include the two cavity polarisations $\boldsymbol{\epsilon}_{L,R}$. Each mode has an annihilation operator $\hat{a}$ or $\hat{b}$ that can only act on its corresponding Fock space $|n\rangle_a$ and $|n\rangle_b$. The modes are degenerate and share a cavity coupling strength g because the birefringence in the cavity is negligible. The bare cavity Hamiltonian then becomes

$$\hat{H}_{0,cav} = \hbar\left(\Delta_c - \Delta_{\text{rep}}\right)\left(\hat{a}^{\dagger}\hat{a} + \hat{b}^{\dagger}\hat{b}\right) \tag{2.19}$$

Next, we need to alter the interaction Hamiltonians. For the laser interaction, the dipole operator is expanded in terms of the atomic operators describing the Zeeman sub-levels.

$$\hat{\boldsymbol{d}} = \frac{1}{2}\sum_{A,B}\sum_{m_a,m_b} \boldsymbol{d}_{A,m_a}^{B,m_b}\left(\hat{\sigma}_{A,m_a;B,m_b} + \hat{\sigma}_{B,m_b;A,m_a}\right) \tag{2.20}$$

here A, B represent the levels $S_{1/2}$, $P_{1/2}$ and $D_{3/2}$. The dipole moment for a transition $\mathbf{d}_{A,m_a}^{B,m_b}$ between states A, $m_a \leftrightarrow$ B, m_b is proportional to the Clebsch-Gordon coefficient for that transition

$$\boldsymbol{d}_{A,m_a}^{B,m_b} \propto C_{A,m_a}^{B,m_b} \tag{2.21}$$

We can now build the individual interaction Hamiltonian for each laser

$$\hat{H}_{SP} = \frac{\hbar\Omega_{\text{driv}}}{2}\sum_{m_S}\sum_{m_P}\left[\boldsymbol{\epsilon}_{\text{driv}} \cdot \boldsymbol{d}_{S,m_S}^{P,m_p}\hat{\sigma}_{P,m_P;S,m_S} + \text{ h.c. }\right] \tag{2.22}$$

and

$$\hat{H}_{DP} = \frac{\hbar\Omega_{\text{rep}}}{2}\sum_{m_D}\sum_{m_P}\left[\boldsymbol{\epsilon}_{\text{rep}} \cdot \boldsymbol{d}_{D,m_D}^{P,m_p}\hat{\sigma}_{P,m_P DS,m_D} + \text{ h.c. }\right] \tag{2.23}$$

The interaction Hamiltonian for the cavity can be written in a similar manner. The two modes, which represent σ^+ and σ^- transitions in the cavity ($\Delta m_{\text{j}} \pm 1$) are as follows

$$\hat{H}_a = \hbar g \sum_{m_D}\sum_{m_P}\left[\boldsymbol{\epsilon}_L \cdot \boldsymbol{d}_{D,m_D}^{P,m_p}\hat{\sigma}_{P,m_P;D,m_D}\hat{a} + \text{ h.c. }\right]. \tag{2.24}$$

and

$$\hat{H}_b = \hbar g \sum_{m_D}\sum_{m_P}\left[\boldsymbol{\epsilon}_R \cdot \boldsymbol{d}_{D,m_D}^{P,m_p}\hat{\sigma}_{P,m_P;D,m_D}\hat{b} + \text{ h.c. }\right]. \tag{2.25}$$

with the combined Hamiltonian being

$$\hat{H}_c = \hat{H}_a + \hat{H}_b \tag{2.26}$$

With this, the Hamiltonian required to fully simulate the system for the two main experiments in this thesis has been acquired. For future experiments, such as ion-photon entanglement, it is necessary to expand this Hamiltonian further to the full eighteen level scheme that includes the $P_{3/2}$ and $D_{5/2}$ levels.

2.3 Dissipation Processes

To model the system in a realistic way, the quantum system's interaction with the environment must be accounted for. This coupling acts as a way for energy to be lost from the system but not gained and for decoherence or relaxation of the qubit state to occur. It is now best to describe the state of this open quantum system in terms of ensemble averaged states using density matrices.

$$\rho_{\text{tot}} = \sum_n p_n \left|\psi_n\right\rangle \left\langle\psi_n\right| \tag{2.27}$$

which describes a probability distribution of states $|\psi_n\rangle$ with probability p_n. The time evolution of this density matrix is given by the von Neumann equation

$$\frac{\mathrm{d}}{\mathrm{d}t}\hat{\rho}_{\text{tot}} = -\frac{i}{\hbar}\left[\hat{H}_{\text{tot}}, \hat{\rho}_{\text{tot}}\right] \tag{2.28}$$

where $\left[\hat{H}_{\text{tot}}, \hat{\rho}_{\text{tot}}\right]$ is a commutator and the total Hamiltonian is

$$\hat{H}_{\text{tot}} = \hat{H}_{\text{sys}} + \hat{H}_{\text{env}} + \hat{H}_{\text{int}} \tag{2.29}$$

with $\hat{H}_{\text{sys}}$ describing the system dynamics, $\hat{H}_{\text{env}}$ describing the dynamics of the environment and $\hat{H}_{\text{int}}$ describing the interaction between them. We can simplify the total density matrix by taking the partial trace to remove the elements describing the environment. This can only be done if we can make several approximations. The first is the Born approximation, the environment acts as a bath and the interaction between the bath and the system does not significantly change the state of the environment. The system and environment must also stay separable throughout the evolution. The second is the Markov approximation, environment dynamics decay much faster than that of the system, and finally that all fast rotating terms in the interaction picture can be neglected i.e the secular approximation. Doing this results in the Lindblad form of the master equation [37]

$$\frac{\mathrm{d}\hat{\rho}}{\mathrm{d}t} = -\frac{i}{\hbar}[\hat{H}, \rho] + \frac{1}{2}\sum_n \left[2\hat{C}_n \rho \hat{C}_n^{+} - \hat{\rho}\hat{C}_n^{\dagger}\hat{C}_n - \hat{C}_n^{\dagger}\hat{C}_n\hat{\rho}\right] \tag{2.30}$$

$\hat{H}$ and ρ are the Hamiltonian and density matrix for the system and C is any number of collapse operators $C_n = \sqrt{2\gamma_n}A_n$ and A_n are the operators which couple the environment to the system with corresponding rates γ_n.

In modelling the system described in this thesis, only two dissipation processes are relevant, as shown in Figure 2.4. The first is the process of spontaneous emission. Here

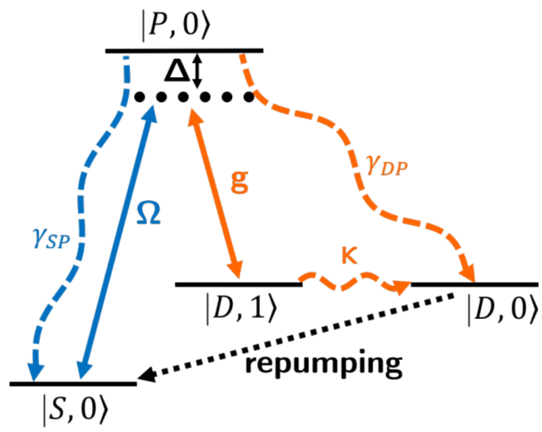

Figure 2.4: Level diagram indicating various decay channels. The combined atom cavity systems state is coherently transferred from $|S,0\rangle$ to $|D,1\rangle$ via a laser with Rabi frequency Ω and a cavity with coupling strength g. Dissipation occurs through three channels, spontaneous decay to either $|S\rangle$ or $|D\rangle$ with associated rates γ, or emission of photons out of the cavity with rate κ. Image from [1].

the atom couples to the many modes of the vacuum field, releasing photons into the bath with a negligible chance of re-absorption. The corresponding collapse operator is

$$C_{\text{spon}} = \sqrt{2\gamma}\hat{\sigma}^{-} \tag{2.31}$$

where σ^{-} is the atomic lowering operator and γ is the spontaneous emission rate, given by

$$\gamma = \frac{\omega_0^3 d_{eg}^2}{3\pi\varepsilon_0\hbar c^3} \tag{2.32}$$

taking into account the Clebsch-Gordon coefficients for each transition, a decay from A to B can be written

$$\hat{C}_{\boldsymbol{\epsilon},AB} = \sqrt{2\gamma_{AB}\left(\boldsymbol{\epsilon}\cdot\boldsymbol{d}_{A,m_a}^{B,m_b}\right)}\hat{\sigma}_{A,m_a;B,m_b} \tag{2.33}$$

The second dissipation process in the system is through the optical cavity. Energy may be lost to the bath through photons leaving the cavity, this can happen by transmission through the mirrors or scattering/absorption by the mirror itself. The operator describing this loss is the photon annihilation operator $\hat{a}$ or $\hat{b}$ for each cavity mode. The rate of loss from the cavity is typically denoted κ and in this case is split into two parts $\kappa = \kappa_c + \kappa_l$, where κ_c is the rate of decay via mirror transmission i.e photons that we can detect or run experiments with, and κ_l is the rate of loss through other means such as scattering or absorption. The collapse operators for the cavity decay are therefore

$$\hat{C}_a = \sqrt{2\kappa}\hat{a} \tag{2.34}$$

and

$$\hat{C}_b = \sqrt{2\kappa}\hat{b} \tag{2.35}$$

2.4 Photon Statistics

The two experiments presented in this thesis rely on the use of two-time correlation functions that describe the statistical properties of light and can be used to simulate interference patterns produced by two identical single photons. The functions we are most interested in are the first- and second-order two-time correlation functions

$$G^{(1)}_{cd}(t, t+\tau) = \left\langle \hat{c}(t)\hat{d}^{\dagger}(t+\tau) \right\rangle \tag{2.36}$$

and

$$G^{(2)}_{cd}(t, t+\tau) = \left\langle \hat{c}^{\dagger}(t)\hat{d}^{\dagger}(t+\tau)\hat{d}(t+\tau)\hat{c}(t) \right\rangle \tag{2.37}$$

which describe correlations between fields $\hat{c}$ and $\hat{d}$ with a relative delay τ between the fields. Equation 2.36 is the first order correlation between the fields and describes the correlations between the amplitudes. Equation 2.37 is the second order correlation function and describes the correlations between the intensity of the fields, this essentially describes the probability of detecting a photon in field $\hat{d}$ at time $(t+\tau)$ after the detection of a photon in field $\hat{c}$ at time t. Both of these functions can be integrated over a period T to obtain functions only in terms of the delay τ

$$G^{(1)}_{cd}(\tau) \equiv \int_T \left\langle \hat{c}(t)\hat{d}^{\dagger}(t+\tau) \right\rangle dt \tag{2.38}$$

and

$$G^{(2)}_{cd}(\tau) = \int_T \left\langle \hat{c}^{\dagger}(t)\hat{d}^{\dagger}(t+\tau)\hat{d}(t+\tau)\hat{c}(t) \right\rangle dt \tag{2.39}$$

2.4.1 Degrees of Coherence

The degrees of coherence of a field are found by normalising the first- and second-order correlation functions to the expectation value of the photon number $\langle \hat{n}(t) \rangle = \left\langle \hat{c}^{\dagger}(t)\hat{c}(t) \right\rangle$. These values are used to characterise fields in terms of their statistical and coherence properties.

First-order coherence

First order coherence describes a fields ability to interfere with itself and gives the visibility of interference fringes seen in a number of interferometer experiments. The first order coherence is given by

$$g^{(1)}(\tau) = \int \frac{\langle \hat{c}(t)\hat{c}^{\dagger}(t+\tau)\rangle}{\langle \hat{n}(t)\rangle} dt \tag{2.40}$$

The value of $g^{(1)}$ can range from 0 (incoherent) to 1 (fully coherent i.e ideal laser). The length of time a source is deemed coherent is called the coherence time τ_c, and is defined as the time taken for the field correlation function to decay. It can be written as

$$\tau_c = \int_{-\infty}^{\infty} \left| g^{(1)}(\tau) \right|^2 d\tau \tag{2.41}$$

for an arbitrary shape of the coherence function. In the case of an ideal laser, the light is of a single frequency and the first order coherence function has the form

$$g^{(1)}(\tau) = e^{-i\omega_0 \tau} \tag{2.42}$$

The magnitude of this function is equal to one at all τ, this gives an infinite coherence time. For any other non-ideal source, broadening of the frequency spectrum of the light leads to a reduction in the coherence time and a non-unity coherence function. For homogeneous broadening (i.e collision broadening) the coherence function takes a Lorentzian shape, for inhomogeneous broadening (i.e thermal broadening) the coherence function has a Gaussian profile.

Second-order Coherence

Second order coherence describes a source's probability of emitting a photon at some time τ conditioned on the emission of an earlier photon. It can be written as

$$g^{(2)}(\tau) = \int dt \frac{\langle \hat{c}^{\dagger}(t)\hat{c}^{\dagger}(t+\tau)\hat{c}(t+\tau)\hat{c}(t)\rangle}{\langle \hat{n}\rangle^2} \tag{2.43}$$

A coherent source such as an ideal laser exhibits Poissonian statistics and there are no correlations in its emission. The second order coherence is therefore unity for all times τ. Broadened sources however have a second order coherence function defined as

$$g^{(2)}(\tau) = 1 + \left| g^{(1)}(\tau) \right|^2 \tag{2.44}$$

A thermal source has super-Poissonian statistics, this means the emitted photons exhibit bunching. A photon is more likely to be emitted shortly after the emission of a previous photon. This results in a second order coherence function that is at maximum amplitude at $\tau = 0$ therefore $g^{(2)}(0) > g^{(2)}(\tau)$.

A non-classical source such as a single atom follows sub-Poissonian statistics, and exhibit photon anti-bunching $\left(g^{(2)}(0) < g^{(2)}(\tau)\right)$. This means the emitted photons are more equally spaced in time than a coherent source and $\left(g^{(2)}(\tau) < 1\right)$. For a pure single-photon source, $g^{(2)}(0) = 0$ as there is no possibility of a second photon being generated. Measuring $g^{(2)}$ is typically the first step in characterising single-photon emitters.

2.5 Numerical Simulations

The simulations performed in this thesis were written in Python and use the Quantum Optics Toolbox (QuTiP). Using this toolbox allows us to use in-built functions for evolving quantum systems, solved numerically by providing the systems Hamiltonian and the collapse operators derived earlier in this chapter. To simulate the system we rewrite the Lindblad master equation in terms of a single superoperator, the Liouvillian $\mathcal{L}$

$$\frac{\mathrm{d}\hat{\rho}}{\mathrm{d}t} = \hat{\mathcal{L}}\hat{\rho} \tag{2.45}$$

Given a Liouvillian and initial density matrix of the system $\rho(0)$, the system can be solved as an ODE, and the density matrix of the system at any time t, $\rho(t)$ can be found. The system may also be evolved to find the steady state solution. To extract useful information out of the simulations, we can obtain the expectation values of observables as a function of time. To do this we take the trace of the operator acting on the density matrix at time t

$$\langle \hat{A}(t) \rangle = \mathrm{Tr}[\hat{A}\hat{\rho}(\mathrm{t})] \tag{2.46}$$

For example, we can plot the population of the atomic states using the relevant projection operator $\langle \hat{\sigma}_A, m_a; A, m_a \rangle$, or using the input-output formalism, we can view the output mode of the cavity $\hat{a}_{\mathrm{out}}(t) = \sqrt{2\kappa}\hat{a}(t)$. Both the temporal shape of the photon and single photon efficiency

$$n_{\mathrm{out}} = 2\kappa \langle \hat{n}(t) \rangle \tag{2.47}$$

$$\eta_{\mathrm{emit}} = 2\kappa \int \langle \hat{n}(t) \rangle dt \tag{2.48}$$

can be found using the photon number operator $\langle \hat{n}(t) \rangle$.

Correlation Functions

The first and second order correlation functions can also be found by the evolving the system in a similar way. Two-time correlation functions of the form $\langle \hat{A}(t+\tau)\hat{B}(t) \rangle$ can be calculated by using the quantum regression theorem to write

$$\langle A(t+\tau)B(t) \rangle = \mathrm{Tr}[AV(t+\tau,t)\{B\rho(t)\}] = \mathrm{Tr}[AV(t+\tau,t)\{BV(t,0)\{\rho(0)\}\}] \tag{2.49}$$

where $V(t+\tau, t)$ is a propagator and defined

$$\hat{\rho}\left(t_2\right)=\hat{V}\left(t_2, t_1\right) \hat{\rho}\left(t_1\right) \tag{2.50}$$

First we calculate $\rho(t) = V(t,0)\{\rho(0)\}$ using the same Master equation solver as before, with $\rho(0)$ the initial density matrix. The same solver is then used to calculate $V(t+\tau, t)\{B\rho(t)\}$ with $\rho(t)$ as the initial state. The functions for doing this for all times τ is built into QuTiP.

For the two experiments presented in this thesis, only the reduced eight-level scheme coupled to an optical cavity is simulated for simplicity.

Chapter 3

Experimental Setup

A linear Paul trap with an integrated high-finesse optical cavity is the basis for the work presented in this thesis. While originally designed to trap and couple a string of ions simultaneously to the cavity, only single ions are necessary for the experiments performed here. The trap and cavity system was designed by Matthias Keller and built by Nicolas Seymour-Smith, Peter Blythe and Dan Crick. Further work to improve trap confinement and the finesse of the cavity was carried out by Stephen Begley and Markus Vogt. In this chapter, a brief description of the ion-trap and associated systems will be given. The parameters of the optical cavity, along with details on how it is locked to stable frequency source will be given. Finally, the laser systems will be described, including a brief overview of both the stabilised frequency reference system and the scanning cavity lock, used to the lock the experimental lasers wavelength. A more in-depth description of these systems can be found in [4]. A detailed look at the trap's construction and characterisation can be found in [4],[3],[38].

3.1 The Ion Trap

The ion trap consists of four rf blade-shaped electrodes and two dc endcap electrodes providing radial and axial confinement respectively. An optical cavity is formed by recessing cavity mirrors inside the endcap electrodes, this is further explained in section 3.3. A resistively heated oven below the centre of the trap, produces a collimated beam of neutral calcium atoms. After photo-ionization of these neutral atoms, $^{40}Ca^{+}$ can then be trapped and cooled. A vacuum chamber, shown in Figure 3.1 surrounds the trap. Nine windows are built into the chamber to allow optical access for lasers, ion imaging and collection of cavity emission. All electrical connections are made via feedthroughs. All components are

UHV (ultra-high vacuum) compatible.

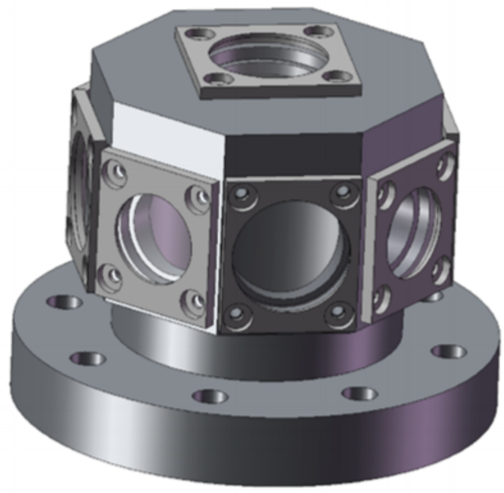

Figure 3.1: Vacuum chamber 3D CAD model. Designed by Matthias Keller, originally from [3].

The ion trap is a monolithic design, the blade-shaped rf electrodes and trap mount structure are machined from one piece of stainless steel using the electrical discharge machining (EDM) technique. The distance from trap centre to rf electrode edge is $r_0 = 0.465$ mm. The separation between endcap electrodes is $2z_0 = 5$ mm.

Figure 3.2 shows both a photo and a schematic of the trap without the cavity mirror assembly. The rf voltage for the blade electrodes is supplied via copper screws, isolated from the rest of the trap via ceramic sleeves. The copper screws are connected to the outside of the trap via copper feedthroughs.

The dc endcap electrodes are glued to PEEK (polyether ether ketone) mounts, which are glued inside holes of the trap mount. The endcap electrodes are hollow and house the optical cavity mirrors behind a 1 mm hole drilled in the end-face. The high-voltage DC is connected via feedthroughs to each electrode with spot-welded tantalum wire.

An oven is mounted below the trap structure, containing a tube filled with grated calcium. The oven is resistively heated by tantalum wires spot-welded to electrical connections via feedthroughs. An aluminium plate is mounted above the oven with a 1 mm drilled hole, acting as a collimator for the neutral atomic beam. Another plate is mounted to the aluminium to act as a source of excitation for taking secular frequency measurements.

The vacuum chamber (Figure 3.1) is octagonal with nine UV and IR anti-reflection coated windows, this decreases the amount of laser light lost to reflections, this increases the lifetime of the lasers and other optical components by reducing the total amount of power needed. The two windows along the cavity axis are used for locking the cavity to a frequency reference (see section 3.2.1) and collecting cavity emission. The other six sides are where lasers for photoionisation, cooling, re-pumping and manipulating the ions state all enter the trap. The window on top is used to image the ion or detect its fluorescence. A diagram of the trap layout can be seen in Figure 3.3.

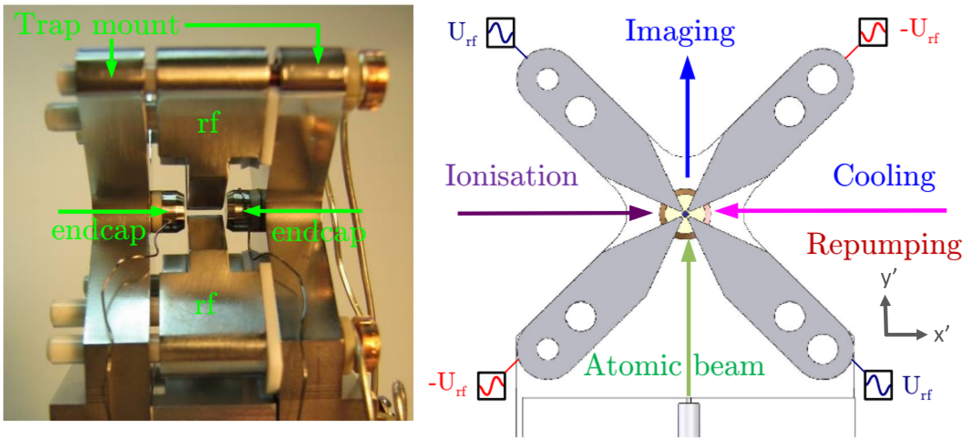

Figure 3.2: Left: Photograph of ion trap, electrodes and mounting system are labelled. Right: Schematic of the trap. Purple and pink arrows indicate general directions for incoming lasers for photoionisation and ion interactions. Taken from [4].

Ions are usually detected in the trap by the 397 nm or 393 nm fluorescence via a CCD camera or a PMT (photo-multiplier tube). Light from the trap is magnified 10x by an objective lens mounted on a 3D micrometer. A periscope mirror then directs the light horizontally through an iris and a bandpass filter centred at 397 nm to remove background scatter. The light is then re-focused by a lens pair. A flip-able mirror then directs the light towards either the CCD camera or PMT. Individual ions can be resolved by the CCD camera, their brightness, position and motion can then be monitored. The PMT outputs a TTL pulse for each photon detected, a computer controlled DAQ can then count these pulses, allowing fluorescence monitoring, spectroscopy or state detection to be carried out. Both the CCD and the PMT are used in micromotion compensation techniques (see section 3.1.3).

3.1.1 Rf driving circuit

The resonant circuit shown in Figure 3.4 supplies rf voltages to the blade electrodes. A function generator supplies an rf frequency to a copper coil via a 5W amplifier. An rf transformer is formed between this coil and another coil with a coil turn ratio of approximately 10:1. The resonator coil is centre-tapped to ground. The rf voltages at opposite

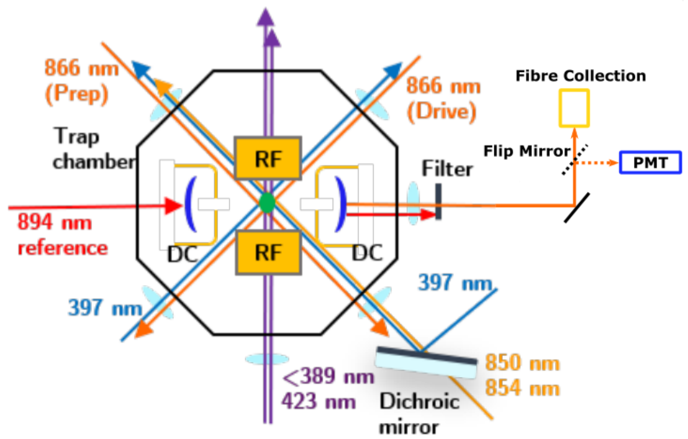

Figure 3.3: Top down view of the trap indicating laser and cavity emission directions. Image modified from [1].

ends of the coil are now in anti-phase. Each terminal provides the rf potential for a pair of opposite electrodes. A variable capacitor is placed in series with each arm to allow the amplitude on each blade to be independently adjusted. With this, the pseudopotential minimum can be shifted with micrometer precision without disturbing the potential shape or increasing micromotion [39], this allows us to optimise the ions position in the cavity field along the x and y directions, increasing the ion-cavity coupling. A DC voltage for micromotion compensation can be supplied to each electrode via a resistor placed in parallel. The capacitors before the resistor isolate the DC from the rest of the circuit.

3.1.2 Parameters

Following [1], the equations of motion in the x and y direction for a particle of mass m and charge Q can be written

$$\frac{\mathrm{d}^2 x}{\mathrm{d}\tau^2} - (a - 2q\cos(2\tau))x = 0 \tag{3.1}$$

and

$$\frac{\mathrm{d}^2 y}{\mathrm{d}\tau^2} - (a + 2q\cos(2\tau))y = 0 \tag{3.2}$$

where

$$q = \frac{2QU_{\mathrm{rf}}}{m\Omega_{\mathrm{rf}}^2 r_0^2} \tag{3.3}$$

and

$$a = \frac{4\eta QU_{\mathrm{dc}}}{m\Omega_{\mathrm{rf}}^2 z_0^2} \tag{3.4}$$

and

$$\tau = \frac{\Omega_{\mathrm{rf}} t}{2} \tag{3.5}$$

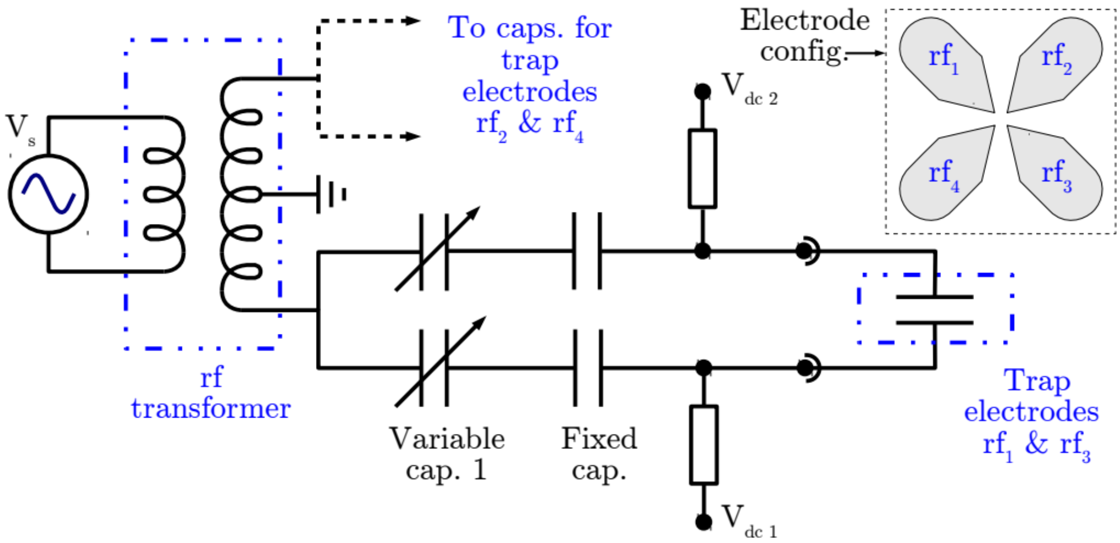

Figure 3.4: The resonant driving circuit. An RF transformer steps up the supply voltage, while a variable capacitor on each output line allows manual adjustment of the psuedo-potential minimum. Image from [4].

with r_0 the distance from trap centre to the blade electrodes, $2z_0$ the distance between endcap electrodes and η a geometric factor. Equations (3.1, 3.2) only have stable solutions for certain values of q and a, fittingly named the stability parameters. Three physical parameters determine these values, the amplitude and frequency of the rf voltage, U_{rf} and Ω_{rf}, and the dc voltage U_{dc}. The radial and secular confinement is then described in terms of the secular frequencies ω_r and ω_a. Deviations in the traps' geometry lead to a geometric factor in the radial secular frequency and a splitting of the radial secular frequency into two components ω_{rx} and ω_{ry}. The secular frequencies are easily measured. An excitation of the ion at one of its secular frequencies causes large oscillations along the corresponding axis. This can be observed via the CCD camera or by monitoring for a drop in fluorescence. As mentioned in Section 3.1 an aluminium plate is mounted within the trap. An adjustable rf field can be applied to this plate via a function generator. The secular frequencies are then measured by the scanning the frequency of the additional rf and monitoring the camera or PMT. For the trap voltages used in this thesis, secular frequencies of $\omega_{ax} = 0.858$ MHz and $\omega_{rx,ry}$ =0.94 MHz and 0.95 MHz were measured. The q and a parameters can then be found by repeating this measurement for a range of values for U_{rf} and U_{dc} and fitting the data. This is performed in [3].

Another important parameter of the trap is the trap depth. An ion can only remain trapped if its kinetic energy is less than the effective potential depth of the trap. The trap depth in a direction $i = x, y, z$ is given by

$$\phi_i = \frac{1}{2} m \omega_i^2 i_0^2 \tag{3.6}$$

where m is the ion mass and i_0 is the electrode to trap centre distance. Only the lowest depth in any direction is important, for this trap it is in the radial direction with a depth of $\phi_r = 2eV$, equivalent to an ion temperature of $10^{-6}K$. Doppler cooling of the ion takes it down to hundreds of microkelvin, significantly reducing the likelihood that the ion has enough energy to escape the potential well. The ion lifetime (several hours) for this trap is therefore limited by the background gas collision rate, proportional to the pressure inside the trap.

3.1.3 Micromotion Compensation

A theoretical description of micromotion is shown in [1]. Micromotion is the ion's driven motion at the frequency of the trap drive. Intrinsic micromotion, a natural consequence of the rf trapping fields, cannot be compensated. Extrinsic micromotion is comprised of two parts, arising from a phase mismatch of the rf trapping field, along with stray dc fields. The phase mismatch cannot be compensated for, and must be addressed by careful consideration of the trap electronics. Excess micromotion from stray dc fields can be minimised by applying compensating dc voltages to the rf blade electrodes. These dc voltages can be described by decomposing the radial trap plane into orthogonal horizontal and vertical axes, H and V (these correspond to the x' and y' axes defined in Figure 3.2). The compensating dc voltages then become:

$$H = (U_1 + U_2) - (U_3 + U_4) \tag{3.7}$$

$$V = (U_1 + U_4) - (U_2 + U_3) \tag{3.8}$$

where U_i is the voltage applied to electrode i.

There are several ways of detecting excess micromotion, these include using the CCD camera, a photon correlation technique and looking directly at the cavity emission while scanning the frequency away from resonance. The amplitude of the radial potential directly affects the offset of the ion from the trap centre when micromotion is caused by stray dc fields. This allows for a detection technique using the CCD camera. The rf potential is swept through a range of values, the value of H (the horizontal component of the compensation field) is then changed until the ion's position is fixed on the camera. The horizontal component has now been coarsely compensated, limited mainly by camera

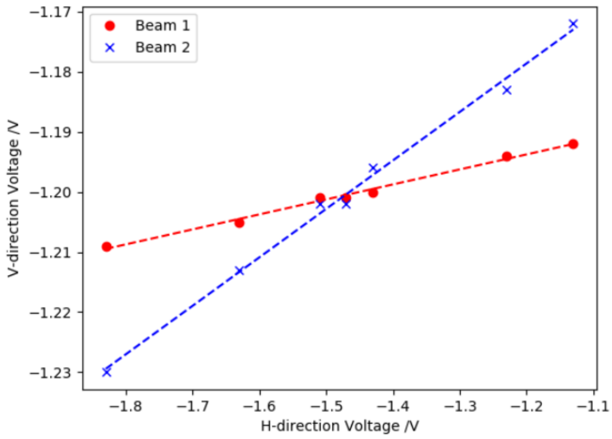

Figure 3.5: A plot showing the best effective micromotion compensation voltages applied in the Horizontal (H) and Vertical (V) directions. The crossing point of the fitted lines indicate the optimal voltages for which micromotion is compensated in both directions.

resolution. The vertical component can also be compensated for in this way, however, due to the trap layout, micromotion in this direction cannot be seen by the camera in its current position. A second technique is therefore required to fully compensate micromotion in two directions.

A correlation technique originally described in [40] is used to compensate the micromotion with finer control and in two directions. This technique can be used to measure micromotion in n dimensions, requiring n laser beams to do so. For this trap, only two dimensions need to be compensated as any micromotion in the axial direction is assumed to be negligible. [1] Due to the Doppler effect, micromotion in the direction of a laser beam modulates the lasers' frequency seen by the ion at the trap drive frequency. By taking the cross-correlation between the PMT signal and the trap drive frequency a sinusoidal relationship can be seen. Using a time-to-digital converter the cross-correlation of PMT counts and the trap drive trigger pulse can be taken. A sinusoidal function can then be fitted, with values of the amplitude and phase extracted. A more detailed description of the method used on this trap is found in [38]. The visibility of the fitted sine wave has a direct relationship to the micromotion amplitude. With perfect compensation the amplitude of this curve will be zero.

A linear relationship between H (Eq.3.7) and V (Eq.3.8) exists. For any value of H, there is a value of V which minimises micromotion in the direction of that laser. There

[1]This is not strictly true and performance of the system would likely be improved by a redesign to allow room for a cooling laser along that direction.

still exists however, a component of micromotion in the direction perpendicular to the applied laser. It is therefore necessary to use a second beam, at some angle from the first, to compensate for this extra component. To determine optimal values for H and V, a scan is performed. For each beam, H is set to a range of values, the optimal value of V is then found for each case. These two lines are then plotted, the intersection of which determines the optimum values for H and V for micromotion compensation in 2D. An example plot is shown in Figure 3.5. Zero amplitude and therefore perfect compensation is not possible due to a small amount of residual micromotion caused by the phase mismatch of the electrodes. The amount of which is not significant to impact the experiment.

The final measurement of micromotion that can be performed using this trap uses the optical cavity. The cavity frequency can be scanned as explained in Section 3.3. The Raman resonance occurs when the cavity detuning Δ_c is equal to the laser detuning Δ_l. When the detunings meet this condition, the single photon rate is maximal. Excess micromotion causes a modulation of the laser frequency and as such the Raman resonance condition is now met when $\Delta_c = \Delta_l \pm n\Omega_{rf}$ where n is an integer. The amplitude of these micromotion sidebands indicate the strength of the remaining micromotion. For well compensated micromotion using the correlation method outlined above, the ratio of the first sideband to the carrier resonance is less than 5 %. This is small enough to not have a measurable influence on the experiments performed in this thesis and does not greatly affect cavity coupling.

3.1.4 Magnetic Field

The electronic states of $^{40}Ca^+$ used in this thesis have magnetic sublevels, whose degeneracy is lifted by the presence of a magnetic field. This is exploited in the experiments presented in Chapters 4 and 5, where specific transitions within the D manifold are targeted. This kind of selectivity is especially important in quantum information and computing experiments, which is discussed in further detail later. The strength and direction of the magnetic field the ion experiences is critical, while the strength determines the splitting of the sublevels, the direction defines the quantisation axis, which in turn determines the relative polarisation of incoming laser light and outgoing cavity emission. To accurately control the magnetic field the ion experiences, the ambient field must be measured and compensated.

Three pairs of Helmholtz coils surround the trap applying magnetic fields in the x-, y- and z-directions. Each coil pair is centred on the trap centre. For each coil pair, the

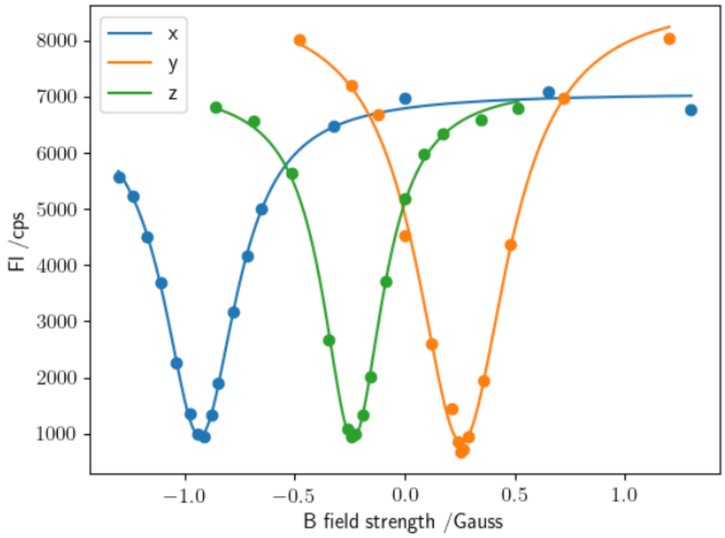

Figure 3.6: Ion fluorescence vs magnetic field strength in x, y and z directions. For each measurement, the other two directions are fully compensated. Lorentzian curves are fitted and minima of −0.93, 0.26 and −0.24 G are found.

current-field strength gradient is measured using a magnetometer and confirmed using an optical cavity scan and observing the splitting in the emission spectrum. A low noise ($<$ 1% of maximum current) power supply is used to supply current to each set of coils, with estimated fluctuations of the magnetic field strength on the order of a few milligauss, i.e a few kilohertz of zeeman splitting.

The experiments performed in this thesis require the ambient field to be nullified and a strong magnetic field to be applied in a particular direction. To do this, the ions' fluorescence can be used. Using an 866 nm beam as a repumper, a superposition $|\Psi\rangle = \sum_m \alpha_m |\mathrm{D}_{3/2}, m\rangle$ state exists for any polarisation of repumper where the ion is dark. This allows us to nullify the ambient field by minimising the ion fluorescence while repumping with a particular polarisation.

In our case, the easiest way to perform this field nulling, is to have an 866 nm repumper aligned perpendicular to the cavity axis. A polarising beam splitter cube is placed in front of the fibre collimator to filter the polarisation of the beam, the transmitted light which reaches the ion is p-polarised with reference to the cube and is π-polarised light with respect to the ion. For this polarisation the dark states are $|\mathrm{D}_{3/2}, m_J = \pm 3/2\rangle$. The magnetic fields coils perpendicular to the laser propagation direction are then scanned to find the fluorescence minimum. The polarisation of the laser is then rotated 90° using a half-waveplate and the magnetic field coil parallel to the laser direction is scanned. The magnetic field is now fully compensated, results of these scans can be found in Figure 3.6.

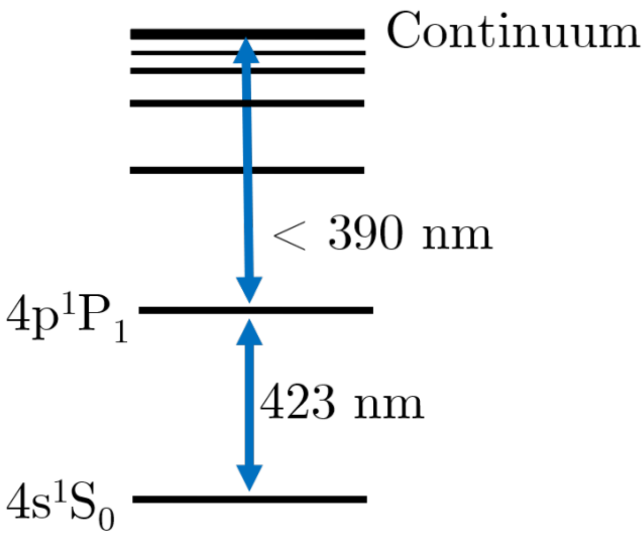

Figure 3.7: Level scheme for the two-stage photoionisation process of neutral calcium. The atom is first excited by a laser at 423 nm, before a laser at 375 nm excites a single electron.

An extra magnetic field can also be applied to any of the magnetic field coils, allowing us to control the exact direction and strength the ion feels.

3.2 Lasers

Many lasers are required to cool and manipulate ions. All lasers used are external-cavity diode lasers with linewidths on the order of a hundred kilohertz.

Neutral calcium is first photoionised in a two-step process pictured in Figure 3.7. The neutral atoms are first excited using a 423 nm laser that is frequency stabilised. A 375 nm laser then excites an electron into the continuum. This laser does not need to be stabilised as the wavelength is well below the threshold value of 389 nm.

For the experiments performed in this thesis lasers at 397 nm, 850 nm, 854 nm and 866 nm are required see Figure 3.8. 397 nm laser light is produced by frequency doubling a laser at 793 nm. The IR lasers are all passed through tampered amplifiers (TA) to significantly increase the output power. The lasers all pass through acousto-optic modulators (AOMs) which allows for precise control over the power and frequency of the laser, while also providing a fast switching time allowing for accurate pulse sequences. Voltage-controlled oscillators (VCOs) generate rf signals which are used to drive the AOMs. Two control voltages can be applied for modulating the amplitude and frequency of the rf drive. These control voltages are controlled via a PC and produced with a digital-analogue converter

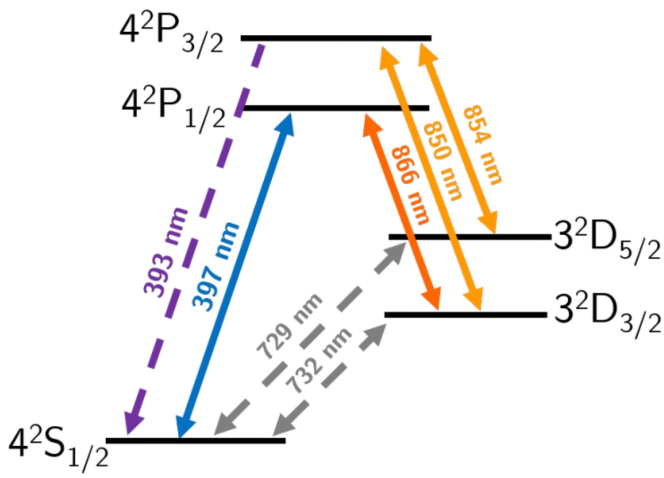

Figure 3.8: Reduced energy level scheme. Solid arrows indicate transitions addressed by lasers experimentally, dotted lines indicate transitions not used. Zeeman splitting has not been indicated. Image from [1].

(DAC). Arbitrary laser pulse shapes can be produced by controlling the amplitude of the VCO with a waveform generator. Each rf voltage passes through an rf switch with an extinction ratio of 50 dB and controlled by TTL pulses. This allows an FPGA or other sequencer to control laser pulses. The 850 nm and 854 nm lasers used for repumping the ion in the cooling cycle are overlapped and passed through the same AOM in a single-pass setup, and then coupled into a polarisation maintaining (PM) fibre, see Figure 3.9 B). A half-waveplate is used to align the laser polarisation to the fibre core. The 397 nm and 866 nm use a double pass AOM configuration see Figure 3.9 A), this significantly reduces the beam diffraction angle dependence on the modulation frequency [41], allowing us to scan the laser frequency without modulating the power of the laser by way of changing the fibre coupling. Trap side, the beams are collimated and focused to pass through the trap centre without scattering light off of the electrodes. This decreases background counts on the PMT and electrically charging the electrodes. Each beam can pass through an assortment of beam cubes and waveplates, used to set the polarisation of the beams. The types used vary from beam to beam, depending on the experimental requirements.

The wavelength of these lasers is critical and needs to be stabilised. For rough stabilisation, a wavemeter is used. It reads the wavelength of a laser and passes it to a LABVIEW VI, which compares it against a set value. If the value is different, a virtual PID circuit calculates a feedback voltage for the lasers piezos that adjust the external cavity. With this method the lasers can be frequency stabilised to ≈10 MHz. For better stabilisation, a caesium frequency reference combined with a scanning cavity lock is employed, these systems are described in Sections 3.2.1 and 3.2.2 respectively.

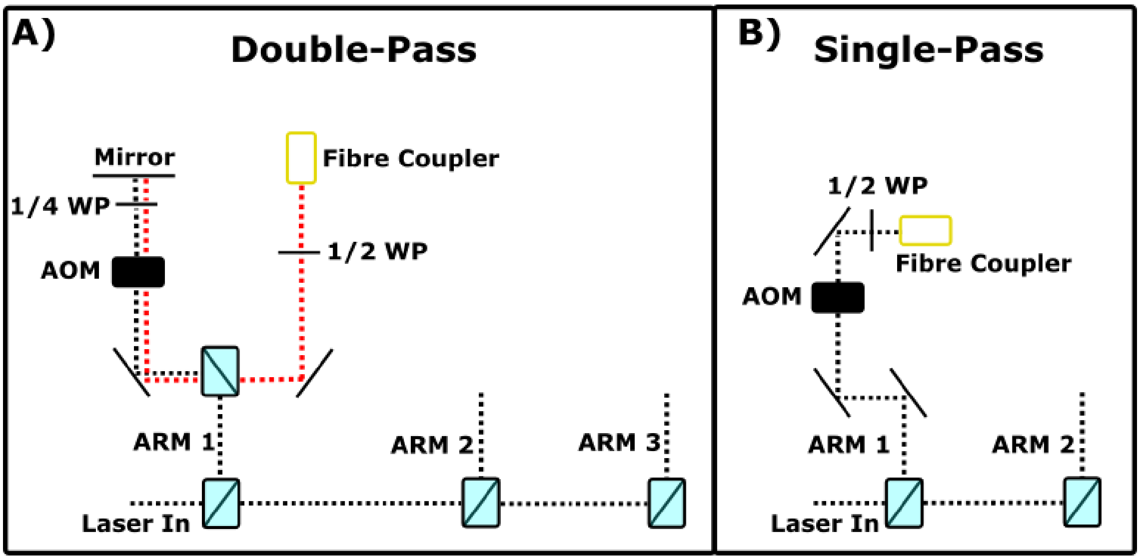

Figure 3.9: General configurations for AOM setups. A) A double-pass configuration. A chosen amount of laser power is directed down each AOM arm. The beam reflects off a PBS cube and is aligned into an AOM. The diffracted beam is reflected off a mirror and passed back into the AOM. A $\lambda/4$ waveplate counters the polarisation rotation caused by the mirror. The beam then passes through the PBS before alignment into a PM fibre, with a $\lambda/2$ to align the polarisation to the fibre core. B) A single-pass configuration. In this setup, the diffracted beam is simply coupled straight into the PM fibre.

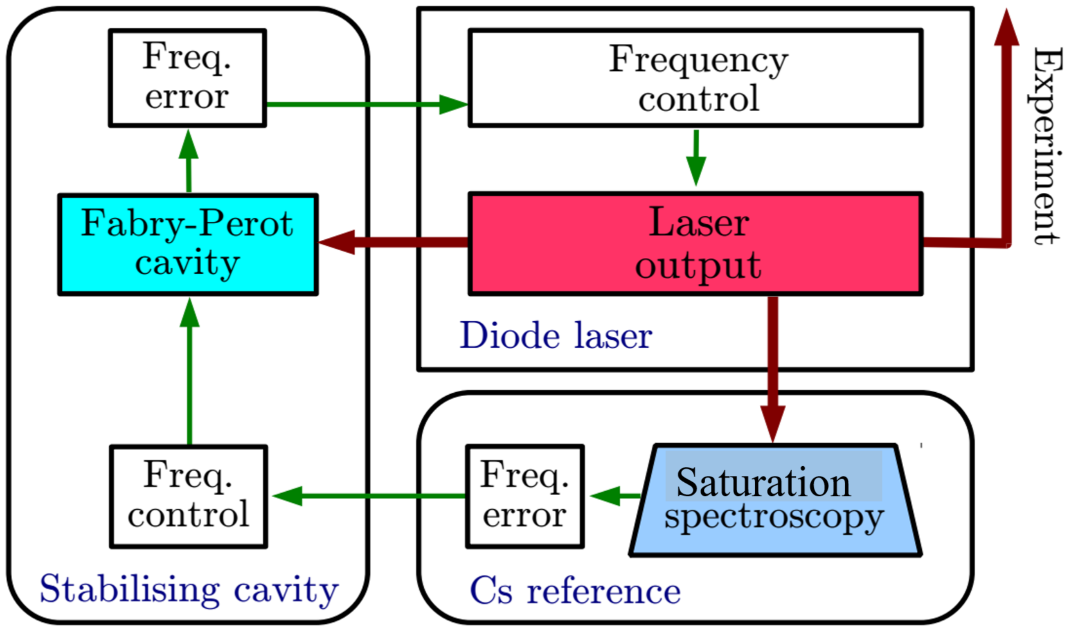

Figure 3.10: Diagram of the locking procedure for the frequency reference laser. The laser is first locked on resonance with an optical cavity, which is in turn locked to a transition in the Caesium reference cell. Image from [3].

3.2.1 Stabilised Frequency Reference

A reference laser at 894 nm is used to stabilise the lasers and the experimental cavity used in this thesis. A two step locking technique is used to stabilise the frequency and narrow the linewidth of this laser via absorption spectroscopy and an optical cavity. A diagram of the locking procedure can be seen in figure 3.10 and the optical setup in figure 3.11. The setup was originally built by Nic Seymour-Smith and Peter Blyth [4] and was later modified by Ezra Kassa and Hiroki Takahashi. The quality of the locks are measured to be 40kHz, well below the necessary requirements of the experimental cavity and laser parameters.

The 894 nm laser output is sent through an optical isolator for stability and to protect the laser diode from back reflections. A wedge plate siphons a small amount of power that is coupled to a fibre and connected to a wavemeter to monitor the wavelength. The remaining power is split between several arms by polarising beam-splitter (PBS) cubes and $\lambda/2$ wave-plates.

The first arm is the cavity locking circuit. Laser light passes through a PBS and is polarisation transformed using a $\lambda/4$ waveplate. The circularly polarised light is then coupled into a Fabry-Perot cavity. Avalanche photodiodes (APDs) are used to monitor the reflected and transmitted signals. The reflected signal is used to create the PDH error signal. This error signal is sent to two PID circuits, one controlling feedback to the laser current controller and one controlling feedback to the laser grating, these both adjust the laser frequency but on different timescales.

The second arm is the spectroscopy circuit. Here, the light is reflected by a PBS and passed through a vapour reference cell containing caesium. A transition in the vapour cell is saturated by the 894 nm light. The light then passes through a $\lambda/4$ waveplate to transform its polarisation into circular polarisation. Around half of the power in this beam is retro-reflected by a mirror, the other half is discarded. The reflected light passes back through the cell, is transmitted by the PBS and detected using a photodetector. An error signal is created using the Lamb dip produced in the emission spectrum by saturating the atomic transition. A PID circuit is then used to control the feedback on the piezo of one of the cavity mirrors, keeping the cavity length resonant with the atomic transition, this in turn keeps the laser stabilised as it was locked to the cavity in the previous step.

The other arms of the system are directly coupled to optical fibres. One is used sent to a wavemeter to monitor wavelength. Another is sent directly to the trap, to be used to lock the experimental cavity. Another fibre is sent to the scanning cavity lock, to be used as a reference to the lock the experimental lasers to.

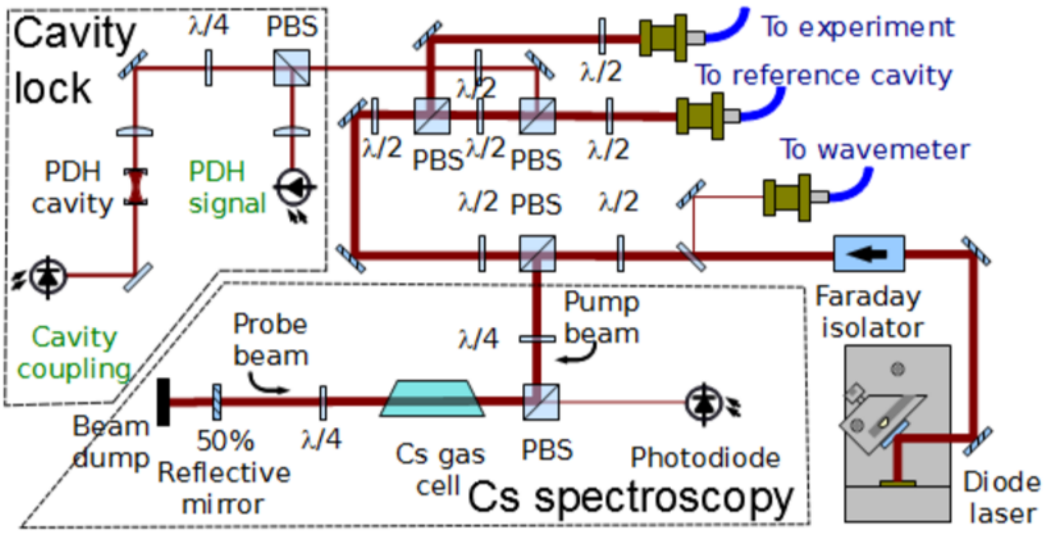

Figure 3.11: Optical setup for the frequency reference system. The stabilised laser is coupled into several optical fibres and used to stabilise other lasers or experimental cavities. Image from [3].

The locking procedure for this system is as follows; the laser frequency is locked to resonance with the optical cavity using the cavity locking circuit, the cavity is then locked to

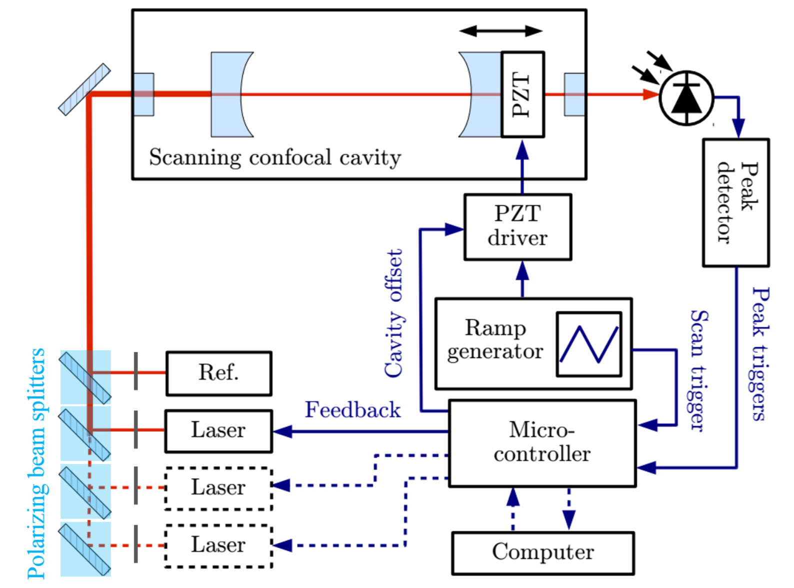

Figure 3.12: Optical/Electronic setup for the scanning cavity lock. Image from [4].

resonance with the atomic transition in the vapour cell. Through this, the laser frequency is is given long-term stability by the atomic reference, while the cavity provides feedback on a faster scale.

3.2.2 Scanning-cavity Lock

The lasers are required to be stabilised below the linewidth of the cavity in order to drive cavity-assisted Raman transitions. In the case of our experimental cavity this is 470 kHz. The commercial wavemeters used in the lab to stabilise the lasers are only rated for a standard deviation of 10 MHz. It is therefore necessary to introduce another method of frequency stabilisation.

To achieve this level of stabilisation we must transfer the stability of the caesium reference laser described in section 3.2.1 to the experimental lasers. The system used to achieve this is called the scanning cavity lock (SCL) and was once again designed and built by Nic Seymour-Smith et al. [4]. The optical setup can be seen in figure 3.12.

The operating principle is as follows, a given wavelength of light will reflect off of a highly reflective cavity unless the cavity length matches the resonance condition. This is met when the cavity length is equal to an integer number of $\lambda/2$ wavelengths, allowing the formation of a standing wave inside the cavity. The reference and experimental lasers are all coupled into the same cavity and the length scanned repeatedly over slightly longer than a single free spectral range using a piezo. A photodiode can be placed in transmission of the cavity which will detect the different resonant conditions for each wavelength of laser.

The time at which the photodiode detects the resonances then becomes a function of laser frequency. The photodiode voltage is sent through a peak detector which produces a TTL pulse whenever the photodiode detects a peak. These can then be monitored by an FPGA which can distinguish each peak with respect to the start of the scan by a trigger signal. The trigger signal and laser peaks are also viewed on an oscilloscope, an offset voltage can be applied to the piezo to change the free spectral range that is being scanned, in order to minimise overlap between peaks. The time difference between two peaks of the reference laser, τ_0 is dependent on the average length of the cavity, this is kept constant by the FPGA calculating a compensating voltage which is then sent to one of the mirror piezos. This transfers the stability of the reference laser to the scanning cavity. The distance between an experimental laser peak and the reference peak is τ_1, to protect against drifts in the scan frequency the ratio $r_1 = \tau_1/\tau_0$ is calculated and can then be kept constant by a voltage generated by the FPGA. This stabilises the frequency of the laser to the same level as the reference lasers stability. A representation of this peak separation is in Figure 3.13. A LABVIEW VI is used to label each peak and determine their ordering, and provide appropriate PID feedback settings for individual lasers, you can also manually adjust r_1 allowing for precise frequency control of the lasers. Using this system the linewidth of the experimental lasers can be reduced to 40 kHz, the level of the reference beam and well below the requirements for the experiment. This system is capable of locking many lasers of different wavelengths in the same cavity. However, increasing the number of lasers increases the difficulty of finding a FSR where none of the peaks overlap. To counteract this, the system is separated into two channels. All lasers are sent through a single cavity, but now the transmitted light is split by a PBS and sent to two photodiodes and peak detector circuits. The experimental lasers can then be given different input polarisations into the cavity to distinguish them. The TTL pulses from the peak detectors are monitored by the same FPGA and can be fed back to without interference from another channel if the time of the peaks overlap. This effectively doubles the capacity of the system. An in-depth description of the system, electronics and programming can be found in [4].

3.3 Experimental Cavity

Two concave mirrors with a radius of curvature R = 25 mm are separated by a distance L = 5.75 mm to form the experimental Fabry-Perot cavity designed to couple with the 866 nm $D_{3/2} \leftrightarrow P_{1/2}$ transition in $^{40}Ca^{+}$. The cavity substrates are slightly recessed inside the DC endcap electrodes, to prevent disturbance of the trapping potential. The axis of the

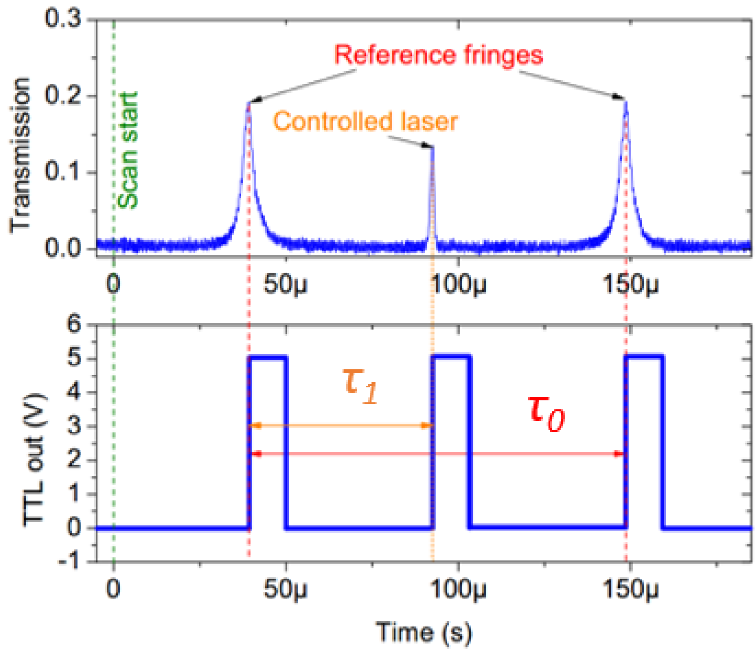

Figure 3.13: Top: Photodiode detection of transmission through the cavity, with two reference laser peaks and a laser peak to be stabilised. Bottom: TTL output of peak detector. τ_0 is kept constant via feedback to the cavity length. τ_1/τ_0 kept constant through feedback to laser frequency. Image from [4]

cavity is set to be co-linear with the trap axis, allowing the coupling of many ions to the same cavity mode in multi-ion experiments [3]. Coatings that are highly reflective at 866 nm are applied to fused silica substrates to form the mirrors. Each mirror is mounted on a ring piezo-electric transducer (PZT) with a 2 μm travel allowing the length and position of the cavity to be changed. This range allows access to approximately 6 free spectral ranges (FSR). An in-depth description of the cavity mounting procedure can be found in [4]. The cavity mirrors built into the trap have specified transmissivities of 100 ppm and 5 ppm. This gives a high degree of directionality to the cavity emission so it can be collected efficiently.

3.3.1 Parameters

The ion-cavity coupling strength g, is one of the main parameters of the optical cavity and is given by

$$g = \sqrt{\frac{d_{PD}^2 \omega_c}{2\hbar\epsilon_0 V}} \tag{3.9}$$

where V is the mode volume and d_{PD} is the transition dipole moment between the

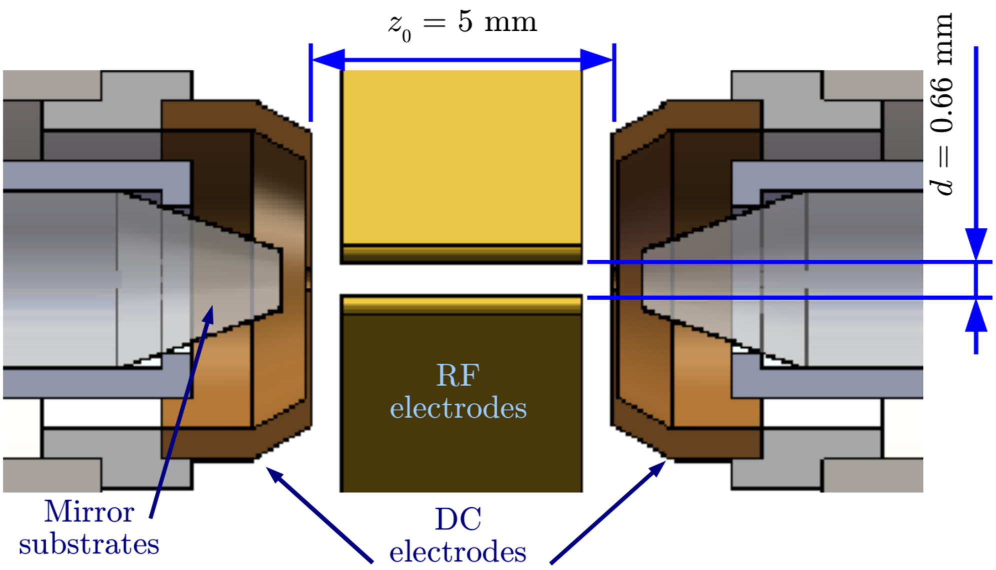

Figure 3.14: Design of trap structure with cavity substrates mounted. Image from [4].

transition states $D_{3/2}$ and $P_{1/2}$. The fundamental Gaussian modes volume V is

$$V = \frac{\pi L \omega_0^2}{2} \tag{3.10}$$

with the cavity waist ω_0 given by[42]

$$\omega_0 = \sqrt{\frac{\lambda}{2\pi}(L(2R-L))^{\frac{1}{2}}} \tag{3.11}$$

For the experimental cavity this gives a value of $\omega_0 = 47$ μm. Inputting this into Eq 3.9 gives a value of $g_0 = 2\pi\times$ 0.795 MHz.

The cavity decay rate is another important parameter of the cavity. The electric field inside the cavity decays due to mirror losses at a rate κ and the intensity decays at a rate 2κ. κ can be calculated from measuring the FSR and calculating the finesse of the cavity. The FSR is defined as

$$FSR = \frac{c}{2L} \tag{3.12}$$

where c is the speed of light and L is the length of the cavity. The procedure for measuring the FSR is as follows; Lock the cavity length with the frequency reference beam, couple laser light at a known wavelength into the cavity and tune to resonance, continue to tune the laser wavelength until it reaches a second resonance with the next longitudinal node. The difference in wavelength is then the FSR. A FSR of 26.04(4) GHz was measured for this cavity leading to a cavity length L = 5.75(1) mm.

The finesse of an optical cavity is a measure of loss in the cavity, either through leakage or being absorbed by the mirror itself. It can be defined either in terms of the fractional losses per round trip or the ratio between the free spectral range and the linewidth of the resonant peaks:

$$F = \frac{2\pi}{1-\rho} = \frac{FSR}{\delta} \tag{3.13}$$

where ρ is the fractional power left in the cavity after one round trip, and δ is the linewidth of the cavity measured at FWHM. Using the specified mirror transmissivities leads to a cavity finesse of $\approx$ 60,000.

Using the relation:

$$\kappa = \frac{2\pi\delta}{2} \tag{3.14}$$

and substituting in:

$$\delta = \frac{FSR}{F} \tag{3.15}$$

We obtain the cavity decay rate in terms of the free spectral range and finesse:

$$2\kappa = 2\pi\frac{FSR}{F} = 2\pi \times 0.434 \text{ MHz} \tag{3.16}$$

The value of 2κ may also be experimentally verified using a cavity ringdown measurement. Laser light is coupled into the cavity and allowed to reach a steady state, the laser is then switched off and the cavity emission observed and recorded. The cavity decay rate can then be obtained by fitting an exponential curve to the recorded cavity emission and obtaining the lifetime. Figure 3.15 shows such a measurement with a witnessed lifetime of 296(8) ns, equating to $2\kappa = 2\pi \times 0.537(7)$ MHz. The higher than expected decay rate can be caused by multiple issues, such as higher than specified transmissivities, fluctuating cavity length or mirror losses. These losses can be caused by imperfections in the mirror surface causing scattering, coating non-uniformity or absorption by the mirror itself.

3.3.2 Cavity Stabilisation

Cavity stabilisation is important in ion-cavity experiments for a number of reasons. Firstly, it is necessary to maintain resonance with the transition you wish to couple to. Furthermore, keeping the linewidth of the cavity small with regards to the optical transitions is important to keep the many, closely spaced transitions resolvable and increase efficiency without the need to use an excessive magnetic field to achieve the desired splitting. The cavity in this thesis is locked to the caesium reference laser, described in section 3.2.1.

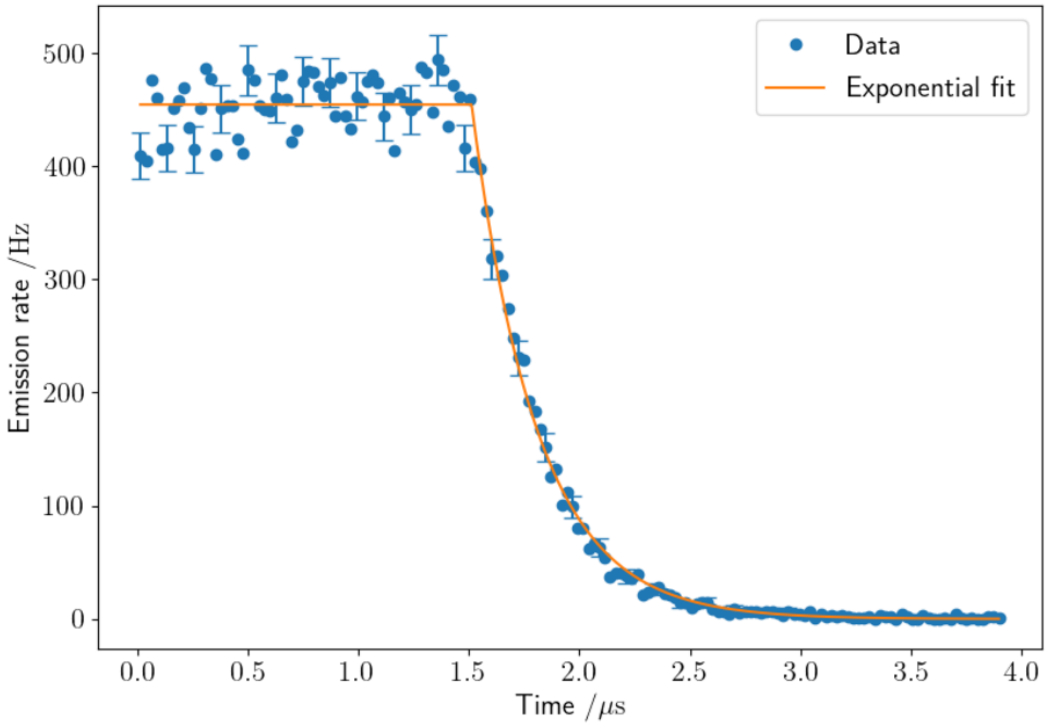

Figure 3.15: Cavity ringdown measurement, plotting cavity emission over time. Data fitted to an exponential decay. Image from [1].

Another important feature to have, is the ability to adjust the cavity length, and therefore the frequency of the transition being coupled. The frequency of the reference laser used to stabilise the cavity is fixed, it is therefore necessary to implement sideband locking, by applying tunable sidebands to the laser being injected into the cavity. The cavity is locked to the TEM_{70} mode of the reference laser to the reduce the intensity of light at the ion position which would cause Stark shifts.

The electronics and optical components for the locking system are shown in Figure 3.16. The Pound-Drever-Hall (PDH) technique is used to stabilise the cavity. First, the reference laser is passed through a fibre integrated electro-optical modulator (EOM) allowing rf signals to be added to the carrier frequency of the light. A tunable rf frequency from a generator with a range of 500 Hz to 500 MHz is added to a 10 MHz modulation signal and sent to the EOM. This produces sidebands at the selected frequency, which allow us to tune the length of the cavity, with secondary sidebands at 10 MHz which are used to produce the error signal. The light is then passed through a $\lambda/2$ waveplate and a PBS, with the waveplate set to maximise transmission through the cube. A $\lambda/4$ waveplate transforms the polarisation into circularly polarised. The beam is then reflected off of the 5 ppm mirror, is transformed back into linear polarised light by the $\lambda/4$ waveplate and

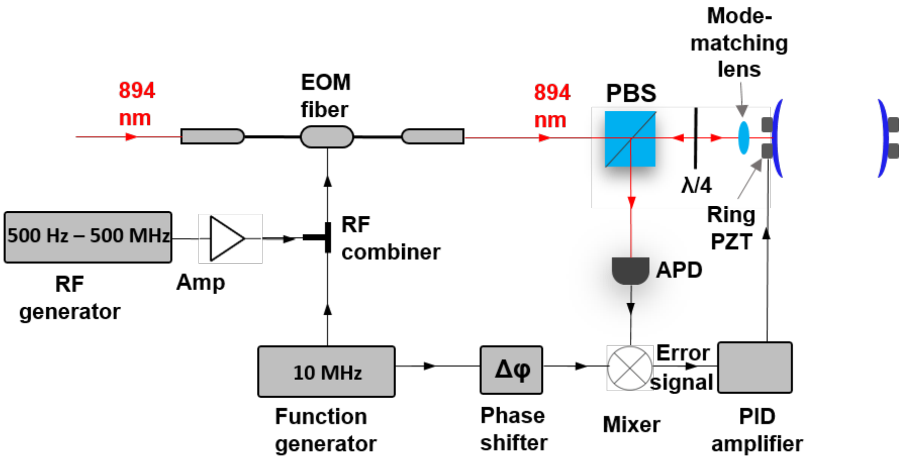

Figure 3.16: Cavity locking electronics and optical systems. Image from [3].

reflected by the PBS. The light is then coupled into an avalanche photodiode detector (APD), the output of which is mixed with the 10 MHz modulation signal producing a PDH error signal. This signal is fed to a PID controller which provides a feedback voltage to one of the cavity mirror piezos via a high-voltage supply. This stabilises the length of the cavity with reference to one of the sidebands of the reference laser.

3.3.3 Optimisation of ion-cavity coupling

The ion-cavity coupling is dependent upon the amplitude of the cavity field at the ions' position. To optimise the coupling, we must therefore move the ion or translate the cavity mirrors to sit on the maxima of the mode. Experimentally this is done by measuring the cavity emission rate. The cavity is locked to resonance with the $\mathrm{D}_{3/2} \leftrightarrow \mathrm{P}_{1/2}$ transition. The ion is continuously driven by 397 nm light and repumped back to the $S_{1/2}$ via 850 nm & 854 nm lasers. This provides a continuous stream of 866 nm photons in the cavity mode. The rate of cavity emission R_{em} is proportional to g^2. The ion can be moved in the trap radially by adjusting the rf electrode voltages and the cavity mode can be moved axially by translating the mirrors with the attached piezos. These two parameters can then be adjusted until the cavity emission rate is maximised.

In order to obtain an accurate description of the dynamics, the ion must no longer be treated as a point particle with a determined position. Instead, its thermal motion causes the ion to probe a region of the cavity field over time. Its spatial distribution then determines the effective coupling to the cavity mode. In this description, the radial motion of the ion can be neglected as its deviation from the trap centre with respect to the mode diameter is small, we then only need to consider motion in the axial direction.

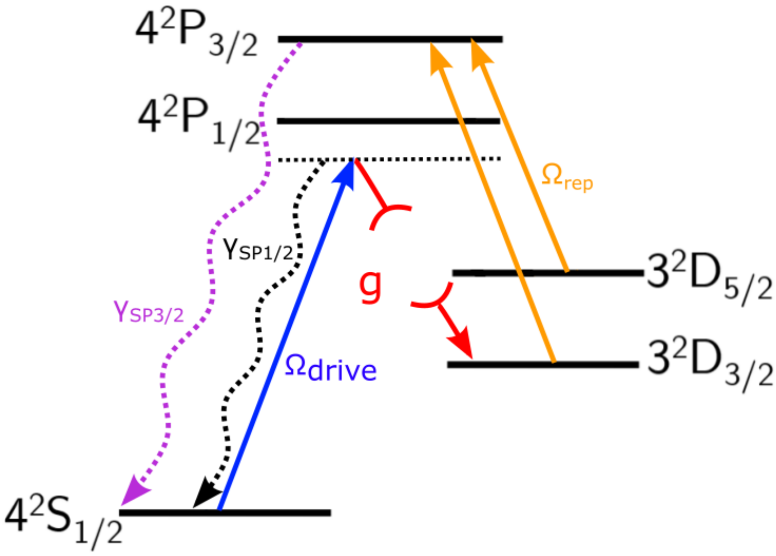

Figure 3.17: Level diagram for the ion-cavity coupling process. The drive laser with Rabi frequency Ω_{drive} drives the ion into the $P_{1/2}$ state. Here, the ion can spontaneously decay back to the S state with a rate $\gamma_{\text{SP1/2}}$ or emit a photon into the cavity with coupling rate g, where lasers with Rabi frequency Ω_{rep} re-pump the ion population back into the S state via a spontaneous emission channel with rate $\gamma_{\text{SP3/2}}$.

The coupling rate g between an ion and the cavity field varies with the strength of the field at the ion position. It can be written as a standing wave along the cavity axis (z)

$$g(z) = g_0 \cos(kz) \tag{3.17}$$

with $2g_0$ equal to the vacuum Rabi frequency and k is the wave number of the cavity field. The absolute square of the ion's position wavefunction can be written as

$$|\Psi(z)|^2 = \sqrt{\frac{1}{\pi \Delta z^2}} \quad e^{-\frac{z^2}{\Delta z^2}} \tag{3.18}$$

with the variance of the ion's position

$$\Delta z^2 \approx \frac{2k_B T}{m\omega_{\text{sec}}^2} \tag{3.19}$$

where ω_{sec} is the axial secular frequency, m is the ion mass, T is the temperature of the ion and k_B is Boltzmann's constant. The average cavity emission R_{em} is proportional to the position averaged coupling which is equivalent to the convolution of $|\Psi(z)|^2$ and $g(z)^2$, the cavity field intensity.

$$R_{em}(z) \propto \int_{-\infty}^{\infty} |\Psi(z')|^2 \, g(z-z')^2 \, dz' = g_0^2 \int_{-\infty}^{\infty} |\Psi(z')|^2 \cos^2(k(z-z')) \, dz' \tag{3.20}$$

A solution to this integral is found in [3], which results in

$$R_{em}(z) \propto \frac{g_0^2}{2}\left(1 + e^{-k^2\Delta z^2}\cos(2\mathrm{kz})\right) \tag{3.21}$$

This shows that as the cavity field is translated over the ions' position, the cavity emission changes sinusoidally, with the amplitude being determined by the ions' position distribution i.e its thermal motion. Using this, we can determine the ions' temperature by relating the visibility of the emission rate to the ions' spatial profile

$$V = \frac{R_{Max} - R_{Min}}{R_{Max} + R_{Min}} = e^{-k^2\Delta z^2} \tag{3.22}$$

and rearranging Eq 3.19 for T. The highest achievable visibility with this trap is around 60%, using only laser Doppler cooling. This leads to ion temperatures of $750\mu K$, roughly 1.4 times the Doppler limit. This may be improved by introducing further cooling methods such as EIT[43] or sideband cooling[44].

3.3.4 Cavity Emission

Cavity emission is collimated by a lens and then optionally filtered using a $\lambda/4$ waveplate and a PBS, allowing selection of σ^+ or σ^- polarised photons. The emission then passes through two band pass filters which block the 894 nm locking light and allow the transmittance of 866 nm with 90% efficiency each. The emission is then coupled into a PM fibre, using a $\lambda/2$ waveplate to match the polarisation of the emission to the fibre. Superconducting nanowire single-photon detectors (SSPDs)(PhotonSpot Inc.) detect the cavity emission and output a TTL for each photon, which is then counted by a DAC or FPGA. The SSPDs have a rated quantum efficiency of >80% at 850 nm with a dark count of 1 cps.

Chapter 4

Improving Indistinguishability of Single Photons

Single photons are a key requirement for many quantum networking schemes. For probabilistic schemes, entanglement between two systems is generated by interfering photons at a beam splitter. If the photons are in any way distinguishable, a loss in the visibility of the interference pattern results, leading to losses of fidelity in the entanglement. Distinguishability can be introduced in the single photon by decoherence processes in the quantum system or via differences in the conditions of how the photon was generated, for example changes in laser frequency. This chapter investigates how we can negate a significant amount of the dominant decoherence process in single photon generation in trapped ions (spontaneous emission). The effect of noise on experimental parameters is also investigated via simulations.

A typical scheme for producing single photons using $^{40}\mathrm{Ca}^+$, with an ion in the initial state $\mathrm{S}_{1/2}$ and driven into the metastable $\mathrm{D}_{3/2}$ states is referred to as the S-to-D scheme throughout this thesis. This scheme has been used successfully in other experiments [45, 46, 47]. In this chapter, we will discuss this scheme in-depth and identify causes for distinguishability to be introduced to the generated photons. We will then introduce a new scheme which is less susceptible to these errors and compare the two using a Hong-Ou-Mandel interference measurement. The beamsplitter relations and the correlation functions required to describe and simulate this effect will also be derived.

4.1 Scheme Comparison - Photon Distinguishability

Figure 4.1 shows the S-to-D single photon generation scheme. A cavity-STIRAP process is used to drive the ions population from the $|S_{1/2}; m_j = -1/2\rangle$ ground state to the $|D_{3/2}; m_j = 3/2\rangle$ state, with a photon collected by the cavity and emitted into the detection setup. In order to individually address the Zeeman sublevels a magnetic field is applied, the cavity frequency can then be tuned on resonance with the desired transition.

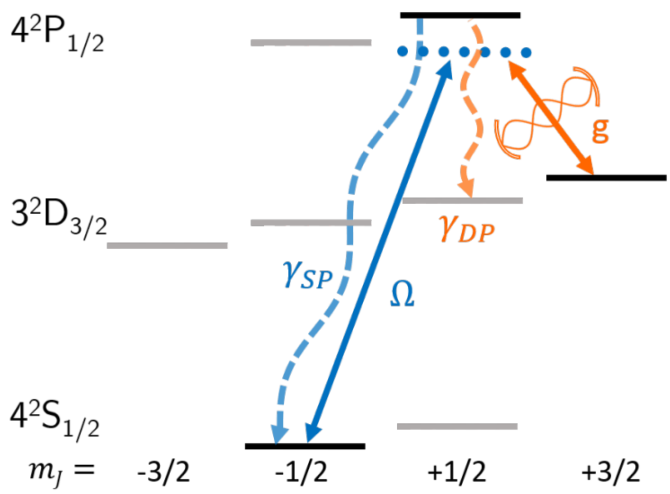

Figure 4.1: S-to-D scheme for single photon generation. Dashed lines represent spontaneous decays to all Zeeman sublevels. Taken from [1].

A major source of distinguishability for the emitted single photons is caused by the spontaneous decay channel γ_{SP}. The state population driven towards the $P_{1/2}$ state is much more likely to decay back to the $S_{1/2}$ state rather than $D_{3/2}$ ($\gamma_{SP} = 10.8$MHz $>>$ $\gamma_{DP} = 0.744$MHz). This results in state population returning to the initial state. This is excellent for maximising single photon efficiency, as the population recycling means several attempts to make the transition during the drive cycle. However, the coherence time of the emitted photon is significantly reduced due to the 'time-jitter' that is introduced. The beams used to drive these transitions typically have a time-dependent Rabi frequency ($\Omega_{driv}(t)$), usually in the form of a Gaussian shape. This shape is specifically chosen to aid adiabatic transfer of the state population. If the state population is reset via a spontaneous emission event, the time-dependent drive beam is no longer at its initial state, resulting in an altered temporal profile of the emitted photon. This effect worsens with the number of decay events. The emitted photon can now be thought of as the probabilistic mixture of many photons produced after N different spontaneous emission events. With the inability to control these spontaneous emission events and the increase in distinguishability, this leaves the S-to-D scheme unsuitable for quantum networking.

To improve the coherence and indistinguishability of the single photons, we must reduce the impact of spontaneous emission. The most effective way to do this is changing the initial state of the ion, so that spontaneous emission events do not recycle population into the drive cycle. We achieve this by introducing a new single photon generation scheme, shown in Figure 4.2.

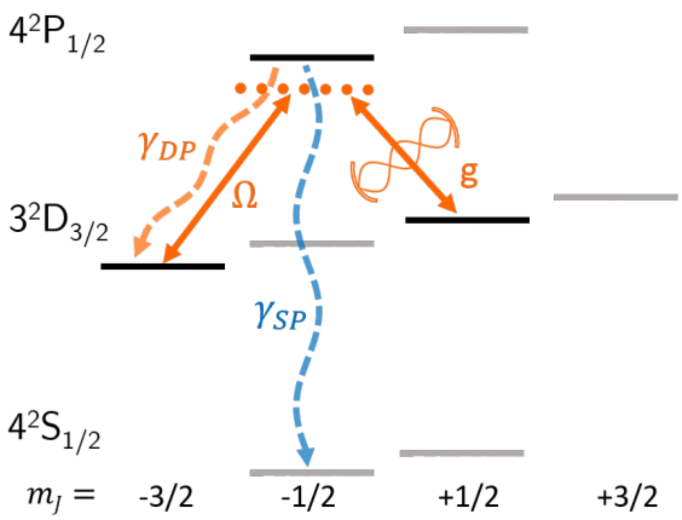

Figure 4.2: D-to-D scheme for single photon generation. Dashed lines represent spontaneous decays to all Zeeman sublevels. Image from [1].

In this scheme, a cavity-STIRAP is driven between two Zeeman sublevels in the $D_{3/2}$ manifold, specifically between the initial state $|D_{3/2}; m_j = -3/2\rangle$ and $|D_{3/2}; m_j = 1/2\rangle$. This scheme will be referred to as the D-to-D scheme throughout the rest of this thesis. By preparing the ion in this way and driving the transition between Zeeman sublevels, the dominant spontaneous decay channel γ_{SP} no longer recycles population into the initial state. While the γ_{DP} decay channel does link to the initial state its strength is much weaker, therefore population recycling is significantly reduced. To compare the number of spontaneous emission events in each scheme a Monte Carlo simulation of the system can be performed and the number of times the ion decays back to the initial state before emitting a photon can be extracted. To gather a statistically significant amount of data, 20,000 runs of the system are performed for each scheme, the distribution of the number of decays is shown in Figure 4.3. The results of this simulation show that for the D-to-D scheme 90% of runs emit the single photon before a decay back to the initial state occurs,

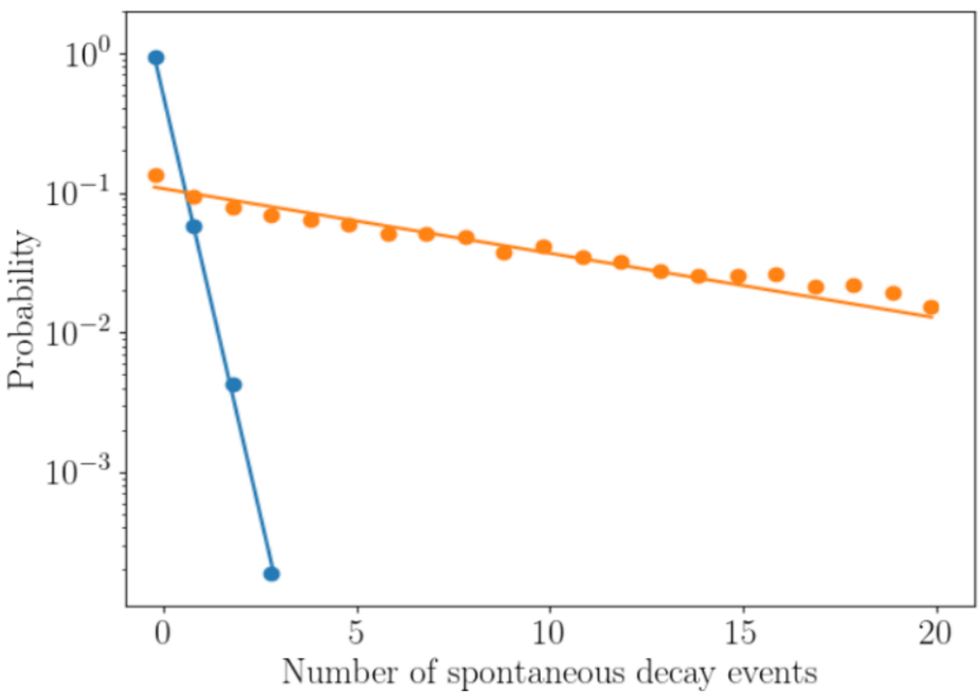

Figure 4.3: Number of spontaneous decay events that occur before a photon is emitted in the S-to-D (orange) and D-to-D (blue) schemes. Obtained from Monte Carlo simulations of the system with 20,000 trajectories per scheme. Taken from [1].

this is in stark contrast to the S-to-D scheme which shows that a significant amount of runs only result in an emitted photon after several decay events, in extreme cases this can be up to 20 events. It should be obvious from this, how the photon state can be corrupted by this uncertainty of emission time. For the D-to-D scheme the γ_{SP} decay channel must still be considered, but instead of harming fidelity it significantly reduces efficiency. This causes the scheme to be unsuitable for deterministic networks, but well suited for probabilistic ones where efficiency is traded for fidelity.

Other experimental factors can affect the distinguishability of single photons. An important property of the photons being interfered is the polarisation, this is fixed by the transition that is chosen, however time-dependent birefringence in optical components such as beam splitters and optical fibres can cause the polarisation of photons to be shifted, in this experiment's case this is generally caused by temperature fluctuations or external vibrations causing stress on the components. Other factors affecting the distinguishability are laser or cavity frequency fluctuations caused by electrical or mechanical noise. Furthermore, magnetic field noise can shift the Zeeman sublevels and the relevant laser and cavity detunings, although this is shown to be a small effect in section 4.7.

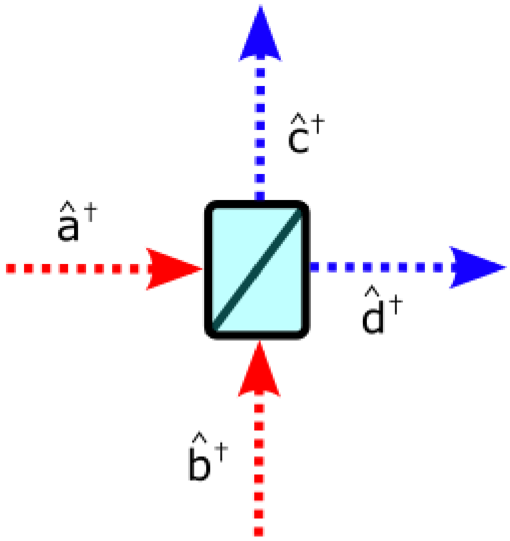

Figure 4.4: Diagram of incident modes $\hat{a}^\dagger$ and $\hat{b}^\dagger$ on a 50:50 beamsplitter, with output modes $\hat{c}^\dagger$ and $\hat{d}^\dagger$.

4.2 Two-photon interference - The Hong-Ou-Mandel Effect

The Hong-Ou-Mandel (HOM) interference effect [48] can be used to measure the distinguishability of two single photons. By treating the description of a beam splitter quantum mechanically a phenomenon occurs, where two identical photons meeting at a balanced beam splitter at the same time will always leave the same exit port. To start, we must consider two identical single photons incident on two input modes $\hat{a}^\dagger$ and $\hat{b}^\dagger$ of a beam splitter see Figure 4.4, described by

$$\hat{a}^\dagger \hat{b}^\dagger |0,0\rangle_{a,b} = |1,1\rangle_{a,b} \tag{4.1}$$

The input modes are transformed into output modes $\hat{c}^\dagger$ and $\hat{d}^\dagger$ by

$$\begin{bmatrix} \hat{a}^\dagger \\ \hat{b}^\dagger \end{bmatrix} = \frac{1}{\sqrt{2}} \begin{bmatrix} 1 & 1 \\ 1 & -1 \end{bmatrix} \begin{bmatrix} \hat{c}^\dagger \\ \hat{d}^\dagger \end{bmatrix} \tag{4.2}$$

Substituting the input modes $\hat{a}^\dagger$ and $\hat{b}^\dagger$ in equation 4.1 for the output modes gives us the following input state

$$\hat{a}^\dagger \hat{b}^\dagger |0,0\rangle_{a,b} \rightarrow \frac{1}{2}\left(\hat{c}^\dagger + \hat{d}^\dagger\right)\left(\hat{c}^\dagger - \hat{d}^\dagger\right)|0,0\rangle_{cd} \tag{4.3a}$$

$$= \frac{1}{2}\left(\sqrt{2}|2,0\rangle_{cd} + |1,1\rangle_{cd} - |1,1\rangle_{cd} - \sqrt{2}|0,2\rangle_{cd}\right) \tag{4.3b}$$

$$= \frac{1}{\sqrt{2}}\left(|2,0\rangle_{cd} - |0,2\rangle_{cd}\right) \tag{4.3c}$$

This shows that due to a π phase-shift in the reflection of the $\hat{b}^\dagger$ mode the probability amplitudes for the photons to leave separate ports cancels out. This results in the photons

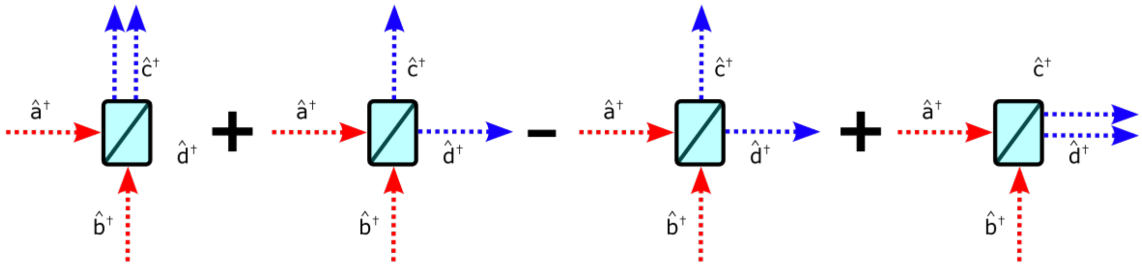

Figure 4.5: Physical representation of Equation 4.3c.

always exiting via the same output mode, see Figure 4.5. If instead, the photons are not completely identical, there will be some probability of the photons occupying both output modes, this probability increases with the level of distinguishability up to a maximum of 50%, where the photons are completely distinguishable. These probability amplitudes can be measured by placing detectors at each output mode and detecting cross correlation events. A conventional way to perform this experiment is to perform two measurement runs, one where the two photons are identical and one where the polarisation of one photon is purposefully rotated perpendicular, in this case no interference occurs. The difference between these interference patterns then directly measures the distinguishability between the two photons. Typically, this difference is referred to as the HOM visibility and is defined

$$V = 1 - \frac{P_{par}}{P_{perp}} \tag{4.4}$$

where P_{par} and P_{perp} refer to the probability of a coincidence count within a time window for parallel and perpendicular polarisation's of the two input fields.

A Hong-Ou-Mandel interferometer is used to measure the distinguishability and determine a sources ability to produce identical single photons. A general interferometry setup, seen in Figure 4.6, is the basis for the two experiments performed in this thesis. Photons are emitted from the source, in this case an ion, at regular intervals separated by a time T. A beam splitter diverts photons down one of two arms, which are recombined at a 50:50 beam splitter where the interference occurs. One arm has a delay of T introduced which ensures the photons meet at the beam splitter at the same time. A detector is then placed on each output mode and a cross correlation measurement is performed.

4.2.1 Time-resolved two-photon interference

To describe and simulate the interference patterns that occur in the experiment we follow [49] to derive the necessary second order correlation functions and use the built in two time correlation functions in QuTiP by [50] to simulate the patterns.

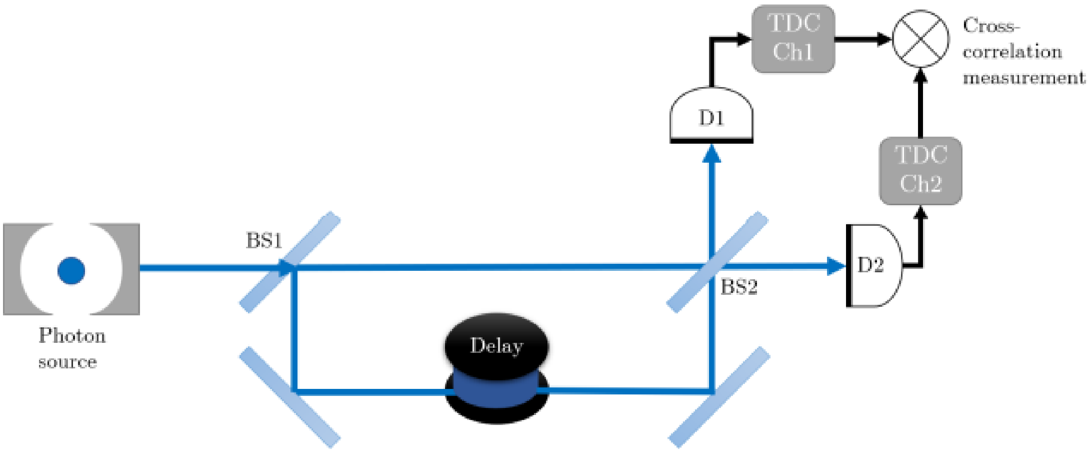

Figure 4.6: A generalised Hong-Ou-Mandel interferometer. Image from [1].

Initially, we rewrite the beam splitter relations so that the output fields $\hat{c}(t)$ and $\hat{d}(t)$ are written in terms of the time-dependent input fields $\hat{a}(t)$ and $\hat{b}(t)$.

$$\begin{bmatrix} \hat{c}(t) \\ \hat{d}(t) \end{bmatrix} = \frac{1}{\sqrt{2}} \begin{bmatrix} 1 & -1 \\ 1 & 1 \end{bmatrix} \begin{bmatrix} \hat{a}(t) \\ \hat{b}(t) \end{bmatrix} \tag{4.5}$$

For our purposes, we are interested in the photon statistics of the output modes, described by correlation functions of the number operator i.e $\hat{n}_c = \hat{c}^\dagger(t)\hat{c}(t)$. The normally ordered correlation functions of the output mode number operators are then

$$\langle \hat{n}_a(t+\tau)\hat{n}_r(t)\rangle = \langle \hat{r}^\dagger(t)\hat{a}^\dagger(t+\tau)\hat{a}(t+\tau)\hat{r}(t)\rangle \tag{4.6}$$

where $\hat{r}$ represents either $\hat{a}$ for the output intensity auto-correlation, or $\hat{b}$ for the output intensity cross-correlation. By substituting equation 4.5 into equation 4.6 we obtain the intensity correlation functions in terms of the input fields

$$\begin{aligned} \langle \hat{n}_a(t+\tau)\hat{n}_{a(b)}(t)\rangle = \frac{1}{4} \sum_{(\hat{c},\hat{d})\in\Pi(\hat{a}',\hat{b}')} &[\langle \hat{c}^\dagger(t)\hat{c}^\dagger(t+\tau)\hat{c}(t+\tau)\hat{c}(t)\rangle + \langle \hat{c}^\dagger(t)\hat{c}(t)\rangle\langle \hat{d}^\dagger(t+\tau)\hat{d}(t+\tau)\rangle. \\ &\pm \langle \hat{c}^\dagger(t+\tau)\hat{c}(t)\rangle\langle \hat{d}^\dagger(t)\hat{d}(t+\tau)\rangle \pm \langle \hat{c}^\dagger(t+\tau)\hat{c}^\dagger(t)\rangle\langle \hat{d}(t+\tau)\hat{d}(t)\rangle \\ &+ \langle \hat{d}(t)\rangle\langle \hat{c}^\dagger(t)\hat{c}^\dagger(t+\tau)\hat{c}(t+\tau)\rangle + \langle \hat{d}^\dagger(t)\rangle\langle \hat{c}^\dagger(t+\tau)\hat{c}(t+\tau)\hat{c}(t)\rangle \\ &\pm \langle \hat{d}(t+\tau)\rangle\langle \hat{c}^\dagger(t+\tau)\hat{c}^\dagger(t)\hat{c}(t)\rangle \pm \langle \hat{d}^\dagger(t+\tau)\rangle\langle \hat{c}^\dagger(t)\hat{c}(t+\tau)\hat{c}(t)\rangle] \end{aligned} \tag{4.7}$$

where +/- correspond to the auto and cross correlation functions respectively. The summation is over the set of permutations of the input mode operators i.e $\Pi(\hat{a}', \hat{b}') \equiv \{(\hat{a}', \hat{b}'), (\hat{b}', \hat{a}')\}$. Terms four to eight in this equation are phase dependent correlation functions, as described in [49]. The contribution of these terms can be neglected assuming either a single photon source or that any phase relation between the two input fields vanishes over repeated runs of the experiment, equation 4.7 then reduces to

$$\begin{aligned}\langle\hat{n}_a(t+\tau)\hat{n}_{a(b)}(t)\rangle = \frac{1}{4}\sum_{(\hat{c},\hat{d})\in\Pi(\hat{a}'\hat{b}')}&[\langle\hat{c}^\dagger(t)\hat{c}^\dagger(t+\tau)\hat{c}(t+\tau)\hat{c}(t)\rangle\\ +\langle\hat{c}^\dagger(t)\hat{c}(t)\rangle\langle\hat{d}^\dagger(t+\tau)\hat{d}(t+\tau)\rangle &\pm \langle\hat{c}^\dagger(t+\tau)\hat{c}(t)\rangle\langle\hat{d}^\dagger(t)\hat{d}(t+\tau)\rangle]\end{aligned} \tag{4.8}$$

Assuming that the two input fields derive from the same source and exhibit identical statistics ($\hat{a}(t) = \hat{b}(t)$) we can simplify this equation further, writing purely in terms of the input operator $\hat{a}$ now

$$\begin{aligned}\langle\hat{n}_a(t+\tau)\hat{n}_{a(b)}(t)\rangle &= \frac{1}{2}[\langle\hat{a}^\dagger(t)\hat{a}^\dagger(t+\tau)\hat{a}(t+\tau)\hat{a}(t)\rangle\\ +\langle\hat{a}^\dagger(t)\hat{a}(t)\rangle\langle\hat{a}^\dagger(t+\tau)\hat{a}(t+\tau)\rangle &\pm \langle\hat{a}^\dagger(t+\tau)\hat{a}(t)\rangle\langle\hat{a}^\dagger(t)\hat{a}(t+\tau)\rangle]\end{aligned} \tag{4.9}$$

This output intensity correlation function is dependent on two detection times t and t+τ. We may obtain the second order correlation functions, giving the likelihood of detecting a photon at time τ after some detection at time zero. To do this, we integrate the two time correlation functions over all times t

$$G^{(2)}_{cd}(\tau) = \int \mathrm{d}t\,\langle\hat{n}_c(t+\tau)\hat{n}_d(t)\rangle \tag{4.10}$$

$$G^{(2)}_{aa}(\tau) = \int \langle\hat{a}^\dagger(t)\hat{a}^\dagger(t+\tau)\hat{a}(t+\tau)\hat{a}(t)\rangle dt \tag{4.11}$$

Additionally, the auto correlation of the field intensity

$$\begin{aligned}G^{(1)}_n(\tau) &= \int \langle\hat{a}^\dagger(t)\hat{a}(t)\rangle\langle\hat{a}^\dagger(t+\tau)\hat{a}(t+\tau)\rangle dt\\ &= \int \langle\hat{n}(t)\rangle\langle\hat{n}(t+\tau)\rangle dt\end{aligned} \tag{4.12}$$

And finally

$$|G^{(1)}_a(\tau)|^2 = \int \langle\hat{a}^\dagger(t+\tau)\hat{a}(t)\rangle\langle\hat{a}^\dagger(t)\hat{a}(t+\tau)\rangle dt \tag{4.13}$$

We have now obtained the second order correlation function of the beam splitter output

$$G^{(2)}_{cd}(\tau) = G^{(2)}_{aa}(\tau) + G^{(1)}_n(\tau) - |G^{(1)}_a(\tau)|^2 \tag{4.14}$$

where we have dropped the $\pm$ sign for +, as we are only interested in cross correlation events. The first term in this equation is commonly called the g_2 of a source, it is a measure of a sources ability to produce single photons, for a pure single photon source this always equals zero. The individual components for this function are easily calculated following the method in Chapter 2. A consequence of this treatment of the beam splitter relations is the fact that, at $\tau = 0$, zero coincidence counts are observed, even for completely distinguishable photons. A typical interference pattern is shown in Figure 4.7, simulated using the equations derived in Chapter 2 with the width of the dip at the centre narrowing for more distinguishable photons.

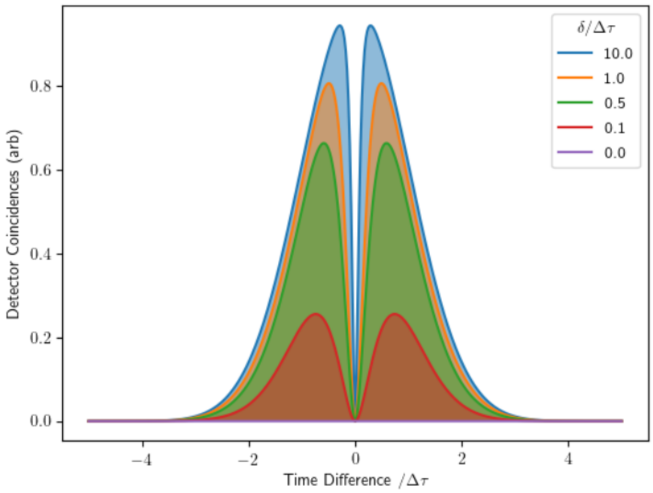

Figure 4.7: HOM interference pattern for spectrally distinguishable photons. With laser linewidth δ as a fraction of pulse width $\Delta\tau$. Image from [1].

4.2.2 Polarisation Distinguishability

In the previous derivation for the second order correlation function we assumed perfectly identical single photons, in the real world however there is some uncertainty introduced by the optical components in the interference and detection setup. We extend the previous analysis to include this uncertainty, in particular for the polarisation of the photons. First, we may decompose the two input fields into two orthogonal polarisation modes. Defining the polarisation of input mode $\hat{a}$ to be horizontal, and that of mode $\hat{b}$ to be rotated by some angle ϕ, we may write the fields as

$$\hat{a}(t) = \hat{a}_H(t) \tag{4.15}$$

$$\hat{b}(t) = \cos(\phi)\hat{b}_H(t) + \sin(\phi)\hat{b}_V(t) \tag{4.16}$$

Substituting this into Equation 4.6, we get

$$G^{(2)}_{cd}(\tau) = G^{(2)}_{aa}(\tau) + G^{(1)}_{n}(\tau) - \cos^2\phi|G^{(1)}_{a}(\tau)|^2 \tag{4.17}$$

Clearly, when the photons polarisations are orthogonal ($\phi = \pi/2$), no interference occurs, with the amount of interference increasing as the polarisations become more parallel.

4.3 Experimental Setup

The experimental setup is shown in Figure 4.8. A repeated sequence of laser pulses, controlled via a FPGA, cause an ion to emit a single photon through the cavity at a regular interval. The cavity emission polarisation is rotated from circular to linear polarisation

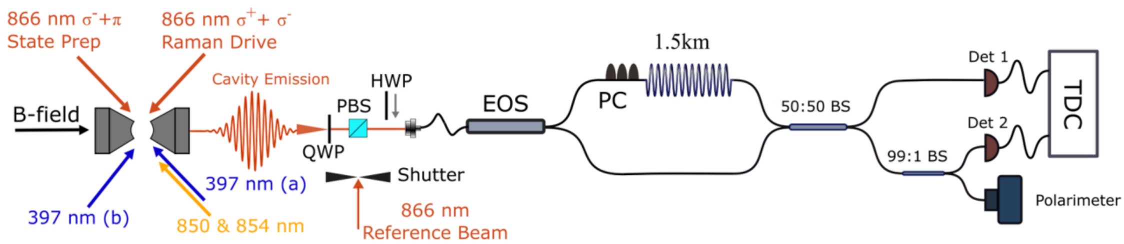

Figure 4.8: The experimental setup. Orientation and polarisation of the lasers are depicted. The cavity emission is then coupled to a fully fibre based HOM interferometer.

via a $\lambda/4$ waveplate. A PBS filters any unwanted polarisation. Two bandpass filters remove the 894 nm cavity locking light, while a $\lambda/2$ waveplate matches the emission polarisation to the collection fibre and the HOM interferometer. In our case, the entire interferometer is fibre based with no free space travel. Instead of an initial beamsplitter to direct the photons down one of two paths, a PM fibre-coupled electro optical switch (EOS) is used instead. This switch is controlled by the FPGA and allows us to direct consecutive photons down different arms. One arm of the setup couples directly to the PM 50:50 fibre beamsplitter (FBS) and is referred to as the direct arm. The other arm couples first to a spool of single mode fibre, 1.5 km in length and then to the other port of the FBS, this arm is referred to as the delay arm. A set of polarisation control paddles are fitted to the delay fibre to allow control over the birefringence and therefore the output polarisation. The outputs of the FBS are sent to individual superconducting single photon detectors (SSPDs). A 99:1 FBS taps off a small portion of one outputs power and delivers it to an external polarimeter. All fibre-fibre connections are spliced to reduce losses.

As discussed earlier, polarisation drift of the single photons leads to a loss in HOM visibility. Because the delay fibre is not polarisation maintaining, photons travelling through the fibre will experience a time-dependent drift in the birefringence of the fibre and will therefore exit the fibre with a rotated polarisation. This is mainly due to mechanical noise and temperature changes. The fibre spool itself is kept within a padded box to dampen vibrations, but there is no active mechanical or temperature stabilisation. Due to the length of the fibre, these changes in birefringence need to be corrected every few minutes of the experiment running. To do this, a reference 866 nm laser is coupled into the setup as the polarimeter is not sensitive enough to detect the experimental single photons. This beam is blocked by a shutter during data collection and overlapped at the PBS with the cavity emission. A $\lambda/2$ waveplate is moved in front of the bandpass filters in order to match the polarisation to the fibre. The polarisation is then viewed on the polarimeter for each arm by manually selecting an output arm for the EOS, and the polarisation of the delay arm

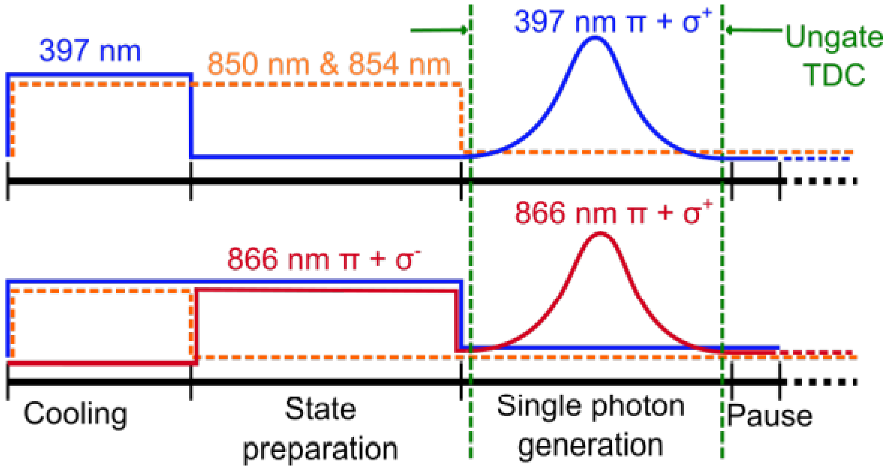

Figure 4.9: Laser pulse sequences for S-to-D (Top) and D-to-D (Bottom) schemes. Relevant polarisation information is depicted.

is adjusted to be either parallel (interference measurement) or perpendicular (reference measurement) to the direct arm. The polarisation drift is on the order of a degree per minute, but this varies greatly day-to-day. This drift would be fixed by replacing the delay fibre with a PM fibre, but this would harm the efficiency (greater attenuation) and we would lose the ability to rotate the polarisation to perform a reference measurement.

4.4 Single photon generation sequence

The laser pulse sequence for each scheme is depicted in Figure 4.9. An FPGA controls the lasers by sending TTLs to RF switches which turn on/off the controlling AOMs. The sequence length is 7.38μs, determined by the length of the delay fibre. The sequence for both schemes can be broken down into three sections, 1.5μs of cooling, 2.5μs of state preparation and finally a 2.5μs drive period where the single photon is created. A 500 ns and 380 ns pause is inserted before and after the drive period respectively, this ensures that no other lasers are on during the generation and that the cavity decays completely before the next cycle. The TDCs are also gated to only accept counts during a certain period, reducing the noise and amount of post-processing necessary to extract the information. To split the Zeeman sublevels a magnetic field of 4.9 G is applied along the cavity axis. This separates the $D_{3/2}$ Zeeman sublevels by 5 MHz. The linewidth of the Raman transition combined with the cavity linewidth is much smaller than this spacing, meaning we can resolve the individual transitions and selectively couple to one of them by tuning the frequency of the cavity. Both schemes begin with a cooling stage, the 397 (a) beam is blue-detuned $\Delta_{cool} = 2\gamma_{SP}$ from resonance and Doppler cools the ion while a combined

850/854 nm beam repumps the ion back into the ground state from the metastable $D_{3/2}$ and $D_{5/2}$ levels. During this process the ion is cooled to 1.4 T_D, which is maintained through the rest of the sequence.

The state preparation and single photon generation are different for each scheme. For the S-to-D scheme the ion is state prepared into a mixture of the $S_{1/2}$ Zeeman sublevels. This is done by removing the 397 (a) beam and allowing the repumpers (850 & 854 nm) to pump the ion back into the ground state. In the single photon generation stage, the 397 (b) beam, detuned $\Delta_{drive} = 2\gamma_{SP}$ from resonance, drives the cavity-STIRAP transition with a Gaussian shape, given by connecting a function generator to the AM (amplitude modulation) input of a VCO (voltage controlled oscillator). This Gaussian has a width $\Delta\tau = 450$ ns and amplitude $\Omega_{drive} = \gamma_{SP}$. The D-to-D scheme meanwhile, is state prepared into the $|D_{3/2}, m_j = -3/2\rangle$ stretch state. To do this, an on-resonance 866 nm beam with σ^+ and π polarisation, along with a 397 nm beam blue-detuned by $\Delta_{prep} = 2\gamma_{SP}$ with mixed polarisation pump the ion population into the designated state as it is a dark state for the selected polarisations of lasers. Given enough time the entire ion population will be prepared in $|D_{3/2}, m_j = -3/2\rangle$. Simulations show the length of time required to do this is $\approx 10\mu$s. With only 2.5μs available for state preparation, roughly 70% of the state population is in the desired state. The single photon is then driven by a σ^+ & σ^- polarised 866 nm beam, red-detuned by $\Delta_{drive} = 2\gamma_{SP}$ with a Gaussian pulse shape of width $\Delta\tau = 450$ ns and amplitude $\Omega_{drive} = 0.5\gamma_{SP}$.

The selected parameters are chosen to optimise the single photon efficiency given the sequence length imposed by the delay fibre. In general, these stages would be better performed at lower power for a longer amount of time, this would reduce any potential heating of the ion as well as maintaining adiabaticity of the process. Optimal parameters were first found using simulations, and then fine tuned experimentally.

4.5 Results

The raw data for this experiment is the photon arrival times detected by the two channels on the TDC, gated during the single photon window. A histogram, spanning several sequence periods, τ_{seq} is built from the differences in arrival time of the photons on the two detectors. This histogram is proportional to the second order correlation function derived in Section 4.2. The histograms for the S-to-D and D-to-D schemes are shown in Figures 4.10 and 4.11 respectively. The histograms consist of evenly spaced peaks separated by the sequence period. Due to the use of the EOS, photons cannot arrive an

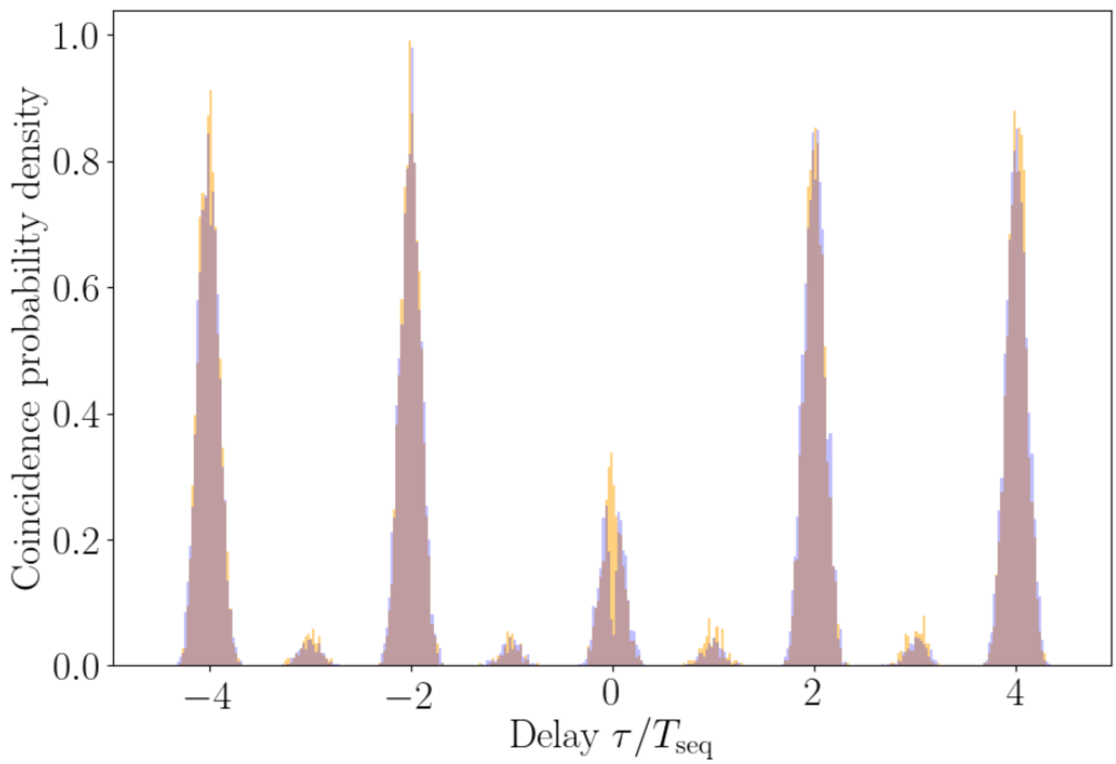

Figure 4.10: Coincidence probability density Histogram for S-to-D scheme with parallel (blue) and perpendicular (orange) polarisation. Bin width = 200 ns.

odd number of sequence lengths apart, as such, these peaks are heavily suppressed and instead give us an indication of the experimental noise, caused by coincidences between a signal photon and background (detector dark count), background and background or leakage of a signal photon through the switch to the other arm.

4.5.1 Single Photon generation efficiency

The photon detection probability histograms for both schemes can be seen in Figure 4.12 and corresponds to the overall photon shape that is the average over the entire measurement period. These histograms are created by comparing the arrival times of photons to a reference trigger pulse generated every 256 cycles and detected by a third channel of the TDC. The S-to-D scheme's probability of a single photon being detected by either detector was $P_{det,SD} = 0.360(3)\%$. The total emission probability can then be extracted by estimating the transmission efficiencies in the system. Each optical component has an associated loss, the largest of which is the delay fibre with a measured $\eta_{\text{spool}} = 44\%$ output efficiency. The total probability of emitting a photon can be calculated as

$$P_{\text{emit}} = \frac{2P_{\text{det}}}{\eta_{\text{filter}}\eta_{\text{coupling}}\eta_{\text{BS}}\eta_{\text{det}}\eta_{\text{splice}}^2(1+\eta_{\text{spool}}\eta_{\text{splice}})(B+A\eta_{\text{splice}}\eta_{\text{tap}})} \tag{4.18}$$

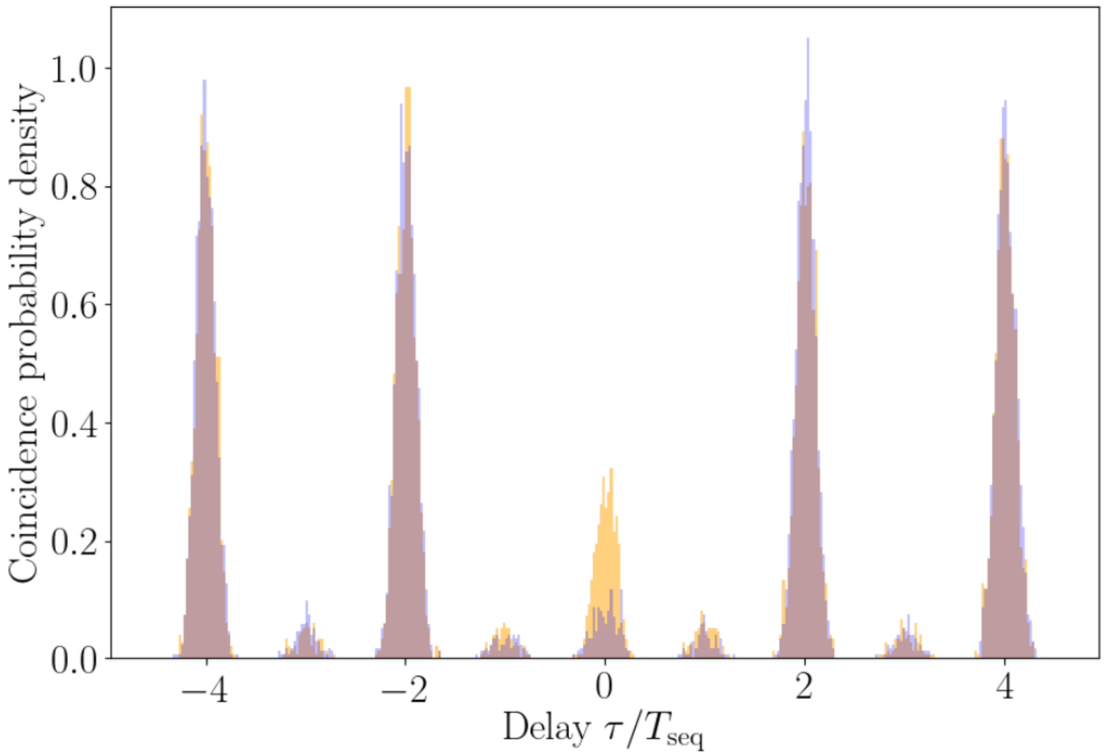

Figure 4.11: Coincidence probability density Histogram for D-to-D scheme with parallel (blue) and perpendicular (orange) polarisation. Bin width = 200 ns.

where η_{filter}, η_{coupling}, η_{det}, η_{splice}, η_{BS} and η_{tap} are the measured efficiencies of the cavity bandpass filters, collection fibre coupling, single photon detectors, fibre splices, 50:50 beamsplitter and 99:1 beamsplitter (total loss includes 1% tapped power) respectively. A and B are the branching fractions of the 50:50 beamsplitter. Using this equation, the probability of emitting a photon with the S-to-D scheme is $P_{\mathrm{emit}} = 1.61\%$. Simulations show an efficiency of 1.8%. The lower measured efficiency is likely due to worse than expected fibre coupling and drift throughout the experimental runs. In addition, the rated detector efficiency is also specified for 850 nm photons, and is likely slightly less than indicated for the emitted 866 nm photons.

For the D-to-D scheme a detection probability of $P_{\mathrm{det,DD}} = 0.05904(3)\%$ is measured, resulting in an emission efficiency of $P_{\mathrm{emit,DD}} = 0.27\%$. An emission efficiency of 0.75% is simulated, meaning there is a different source of loss for this scheme compared to S-to-D. The most likely cause of this is inefficient state preparation. The 397 nm power is kept low to reduce heating, and with the limited time to state prepare, much of the ions population is likely left in the ground state.

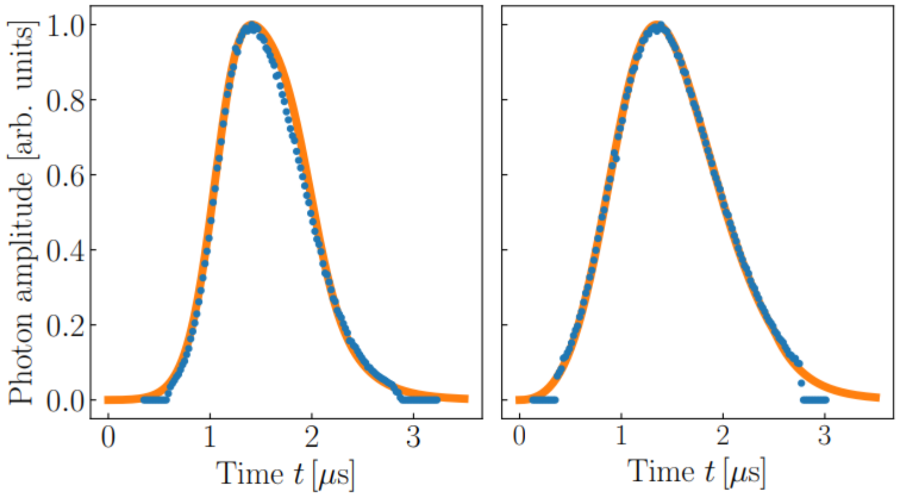

Figure 4.12: Temporal probability distribution of detecting single photons for S-to-D (left and D-to-D (right) schemes. Blue dots show experimental data extracted by sorting photon arrival times into 20 ns time bins with respect to a reference pulse. Both histograms are normalised to unity. Orange solid lines are obtained from numerical simulations of the system.

4.5.2 HOM interference Patterns

To calculate the HOM visibility for each scheme we must normalise the parallel and perpendicular measurements due to differing measurement times. Moreover, the fibre-coupled components have polarisation dependent losses, meaning the overall detection efficiency will be lower for one set of measurements over the other. This must be accounted for in the normalisation as well. The parallel polarisation in this case is set by the direct arm of the experiment, and perpendicular is defined to be orthogonal to that polarisation. The fibre beamsplitter has transmissions of ($\eta_{\mathrm{BS},\parallel} = 0.86$) and ($\eta_{\mathrm{BS},\perp} = 0.63$) for parallel and perpendicular polarisations respectively. We then define the combined transmission efficiency through the delay fibre and beam splitter as $\rho_{\parallel} = 0.38$ and $\rho_{\perp} = 0.28$. The branching ratio of the beamsplitter also changes depending on the polarisation, for parallel polarisation $A_{\parallel} = 0.53$ and $B_{\parallel} = 0.47$. For perpendicular polarisation, $A_{\perp} = 0.75$ and $B_{\perp} = 0.25$.

First, to account for the different measurement times the histograms are scaled such that the area under the peaks is unity. The perpendicular histogram is then scaled to correct for the difference in transmission and branching ratios using the scale factor

$$R = \frac{2A_{\parallel}B_{\parallel}\rho_{\parallel}}{(A_{\parallel}B_{\perp} + A_{\perp}B_{\parallel})\rho_{\perp}} \tag{4.19}$$

The normalised histograms are shown in Figure 4.13, here only the central peak is shown.

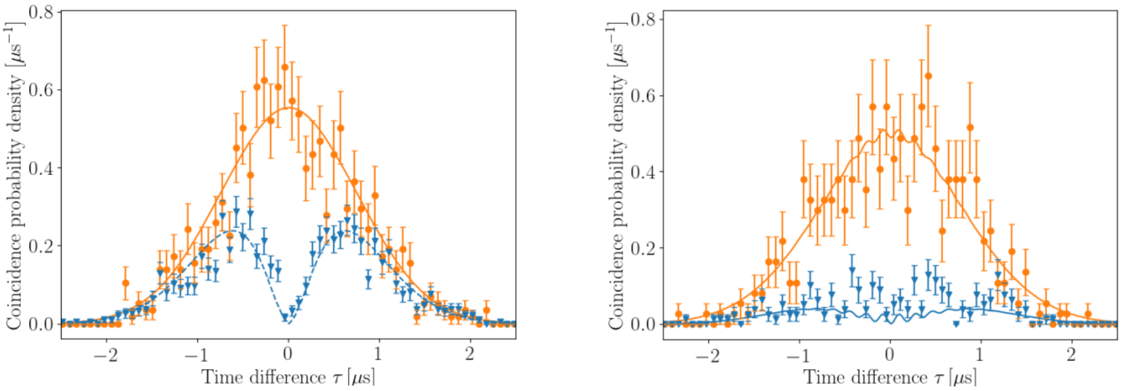

Figure 4.13: HOM interference pattern for S-to-D (left) and D-to-D (right) schemes. Experiment data for parallel (blue) and perpendicular (orange) measurements are shown, along with error bars. Simulations are shown as dashed and solid lines.

The HOM visibility is defined as

$$V = 1 - \frac{\int_{-T/2}^{T/2} C_{\parallel} d\tau}{\int_{-T/2}^{T/2} C_{\perp} d\tau} \tag{4.20}$$

where T/2 is the photon generation period and $C_{\parallel}$ and $C_{\perp}$ are the total normalised coincidence counts for the parallel and perpendicular measurements respectively. A visibility of 50(2)% is calculated for the S-to-D scheme, in close agreement with the simulated value of 53%. For the D-to-D scheme, a visibility of 81(2)% is measured. While this is an obvious improvement on the S-to-D scheme, the simulations show a visibility of 92.2% is achievable. A contribution to this difference is the aforementioned state preparation fidelity. Another source is likely the polarisation drift in the delay fibre. While the measured value for the drift was acceptable, this value is likely to change based on external conditions. By fitting a value for the polarisation offset ϕ in the simulations, we find an average difference of $\phi = 12$. Taking this into account, the measured visibilities increase to 54(2)% and 89(2)% for the S-to-D and D-to-D respectively. The visibility demonstrated in this experiment represents the best reported HOM visibility for an ion-cavity system to our knowledge.

4.6 Scheme Comparison

We will now compare the two schemes based on their usage in probabilistic entanglement schemes. A lot of the analysis done in this section was performed by Tom Walker [1]. For probabilistic entanglement schemes we are interested in two characteristics, the heralded entanglement rate R_{ent} and the fidelity F of the operation. For entanglement schemes such as [51], entanglement is generated between two separated ions' electronic state and the polarisation state of their emitted photons. The photons are interfered on a beam splitter and entanglement is detected by coincidence detection of the photons due to perpendicularly polarised photons. Photons with parallel polarisation that are still distinguishable, results in false positives, it is therefore important that the single photons are as indistinguishable as possible.

The fidelity of the entanglement operation for a single photon source can be written in terms of the HOM visibility as follows [52]

$$F = \frac{1+V}{2} \tag{4.21}$$

For quantum communication between devices the initial fidelity of an operation needs to be as high as possible, as fidelity of transmission of the entanglement tends to be very low. This can be improved by employing entanglement purification [53] in shorter sections of the channel via entanglement swapping. This can be extended to an arbitrarily long communication channel, with an overhead cost in both time and resources. It is therefore important to maintain a high initial fidelity to reduce the negative impact of these purification techniques. In this experiment, we demonstrate how careful selection of the initial state for a cavity-STIRAP transition can significantly increase the HOM visibility and therefore the fidelity of entanglement operations, this is at the cost of emission rate however. In this section we will discuss other ways to increase HOM visibility and compare these to the new scheme presented here.

Many experiments employ a temporal filtering technique [54, 55] to improve the visibility of a HOM interference pattern. By inspecting the typical HOM interference patterns for parallel and perpendicular photons, it can be seen, that by narrowing the maximum detection time T between photons, the amount of coincidences in the parallel case significantly reduces, while the perpendicular case is less affected, this increases the visibility. An example of this trade-off is seen in Figure 4.14 for the S-to-D scheme. To match the experimentally achieved visibility by the D-to-D scheme (81%) a window of T = 400 ns is needed, this cuts the coincidence counts down to 41% of the total collected during the whole measurement window. In comparison, the D-to-D scheme produces coincidences at a rate of 3% of the S-to-D scheme pre-temporal filtering. Therefore the S-to-D scheme seems preferable. However, if we instead look at the simulated results i.e disregarding the technical limitations that reduced the D-to-D visibility the situation changes. To match the expected 92.2% visibility of the D-to-D (higher visibilities have since been obtained, $> 97\%$), a window of T = 210 ns is required. This cuts the coincidence rate down to 23% of

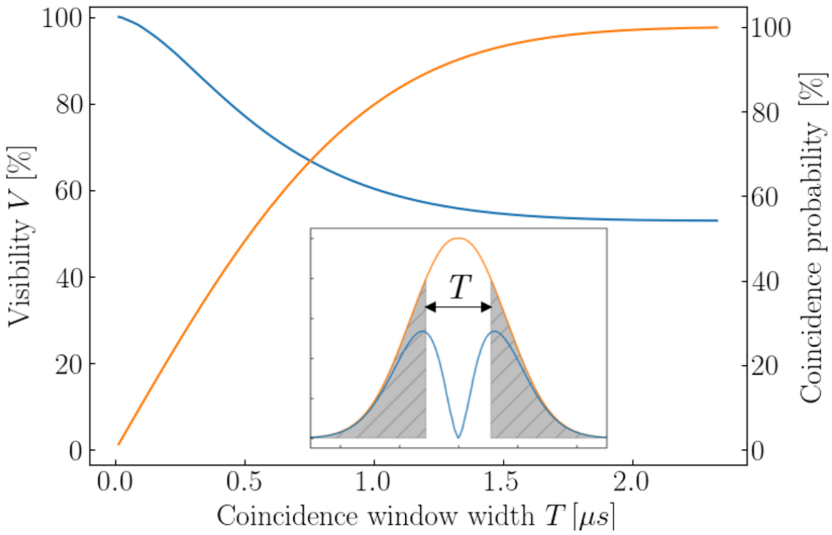

Figure 4.14: Comparison between visibility (blue) and coincidence count rate (orange) with a varying window size T for S-to-D scheme. The insert shows an example of temporal filtering, grey shaded areas are ignored increasing the HOM visibility. Image from [1].

the experimental S-to-D coincidence rate. Meanwhile, simulating the D-to-D scheme with optimal state preparation has an expected coincidence rate of 53% of the experimental S-to-D scheme, a 2x increase. We can clearly see in this case that for any arbitrarily selected target visibility, the D-to-D scheme will outperform the S-to-D in terms of efficiency for all cases when the D-to-D scheme has optimal state preparation. It is for these reasons that we can say temporal filtering only presents a better visibility with regards to technical limitations, such as state preparation fidelity and signal-noise ratio.

The experimental parameters used to generate single photons is also a major factor. For this experiment, these parameters were chosen to maximise the photon emission rate and not the visibility. Heat maps for simulated visibilities and single photon efficiency are shown in Figure 4.15, over a range of laser intensities and detunings. It is seen that for both schemes, further detuning the laser and reducing drive power increases the visibility. We can compare these heat maps in Python. By selecting a random point on the visibility graph for the S-to-D scheme we can obtain an emission probability by looking at the same point on the emission probability heatmap. We can then compare the emission probability for the same visibility (or closest) in the D-to-D heatmap. For all cases, the D-to-D scheme retains a higher emission probability than the S-to-D scheme, making it a better choice in all scenarios. It is also apparent that the HOM visibility of the D-to-D scheme is less sensitive to changes in the laser parameters, this means we can expect a more consistent

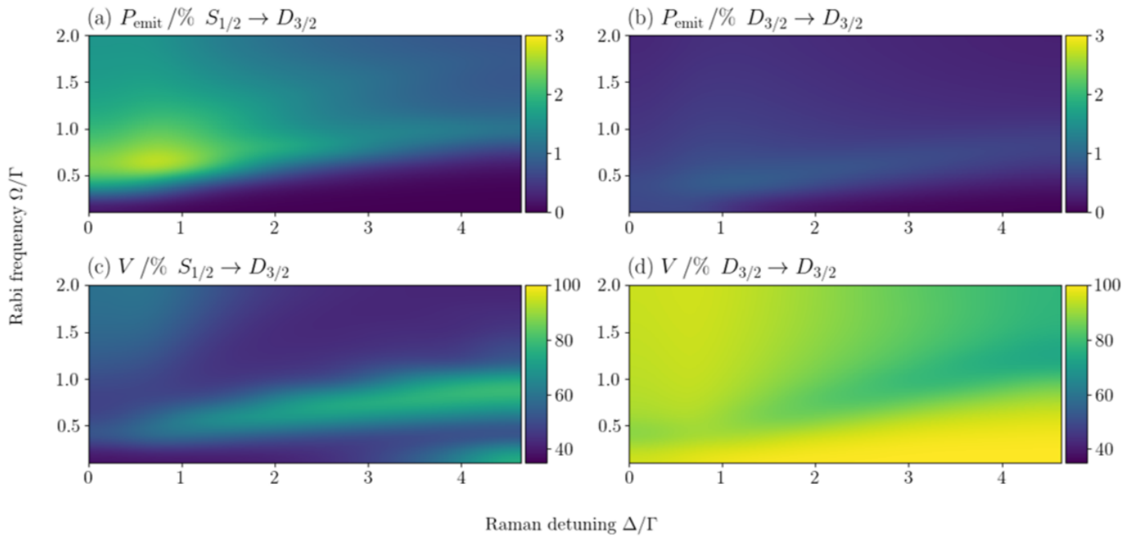

Figure 4.15: Simulated visibility and emission probability heatmaps for the S-to-D and D-to-D scheme, varying Raman detuning and laser power in units of the transition linewidth Γ_{SD}. (a,b) S-to-D and D-to-D efficiency. (c,d) S-to-D and D-to-D visibility.

result with regard to experimental noise, as shown in Section 4.7. Working in the far detuned limit ($\Delta >> \gamma_{SP}$) is a typical way to reduce the amount of population in the excited state ($P_{1/2}$) close to zero. In a recent experiment [56], the far detuning method was used to produce single photons in a $^{40}Ca^{+}$ ion-cavity system, convert them to telecom and measure the HOM interference. In this case a visibility of $V_{SD} = 0.472(8)\%$ was obtained, primarily limited by the spontaneous emission rate. While the two experiments cannot be directly compared due to different parameters, it shows that even when the drive beam is far detuned, the spontaneous emission in the S-to-D scheme is the main severely limiting factor.

Finally, the efficiency achieved in this experiment for the D-to-D scheme is mainly limited by the state preparation fidelity and the Clebsch-Gordan coefficient for the selected transition. By choosing a different initial state with a more favourable Clebsch-Gordan coefficient ($|D_{3/2}; m_j = -1/2\rangle$ we can improve the efficiency. Simulating the system with this initial state, the D-to-D scheme matches the S-to-D generation efficiency if we have perfect state preparation and we choose laser parameters to optimise the emission rate. Doing this, the visibility rises to 96% for D-to-D and 54% for S-to-D, meaning the D-to-D scheme is strictly better in all cases. To achieve this level of efficiency with the D-to-D scheme we would need to employ a new state preparation technique. A STIRAP process has been used to achieve 95% state preparation fidelity in under 10μs [57]. This technique could not be implemented in this experiments case due to the sequence length being limited by the delay fibre.

4.7 Sources of Distinguishability

Discussed earlier in this chapter, the HOM visibility was predominantly limited by the polarisation drift in the delay fibre. In principle, there are other sources of distinguishability that directly affect the single photons being produced. In this section, we will compare sources of noise within the experiment, simulate them and predict their impact on the experimental visibilities.

With the laser linewidths already included within the simulations, we look at drifts in the magnetic field and in laser/cavity detunings between two photon emission events. This would produce photons with slightly differing frequencies, and could represent some noise on experimental equipment where the same source is used to produce both photons with one being delayed by a cycle length or differences between two separate sources. To calculate the HOM interference patterns, we take an 'expected' photon and use that as a common mode input for all of the interference patterns. The other mode input is the photon produced by the various parameter sets (B, Δ_{cav}, Δ_{las}). These interference patterns are then summed, weighted by a Gaussian distribution, centred on the point where the parameter value matches that of the "expected" photon. The overall visibility is then calculated against the summed reference signal using the same Gaussian distribution. The comparison in visibility from two identical single photons to this weighted average of non-identical photons gives us an indication of how sensitive the two-photon interference is to noise variations of certain parameters.

4.7.1 Magnetic Field

We begin by varying the magnetic field that each photon is produced under. This changes the Zeeman splitting and results in photons of differing frequencies, this in turn changes how the photon couples to the cavity. The centre B-field used was 4.89 Gauss, this corresponds to a 3A current through the Helmholtz coils. The photon produced under this condition is used as the common mode input for the beam-splitter between all interference patterns calculated. Figure 4.16 shows the individual results for a few different photons produced under different B-fields interfering with the common photon, along with the summed results for all parameters. Clearly, photons produced under different magnetic fields affect the indistinguishability of the single photons produced. The visibility loss is

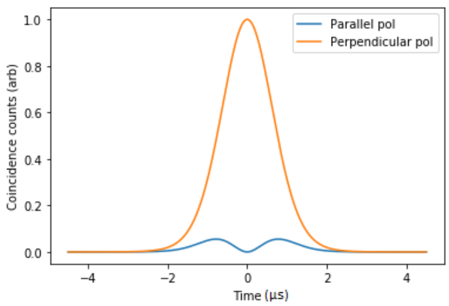

(a) $\Delta B = 0.17$ Gauss

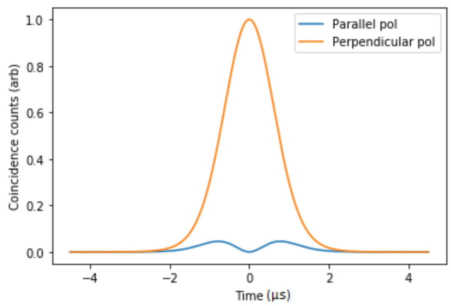

(b) $\Delta B = -0.17$ Gauss

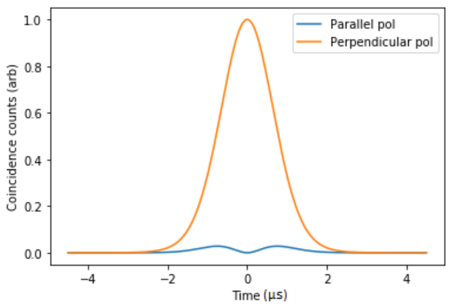

(c) $\Delta B = 0$ Gauss

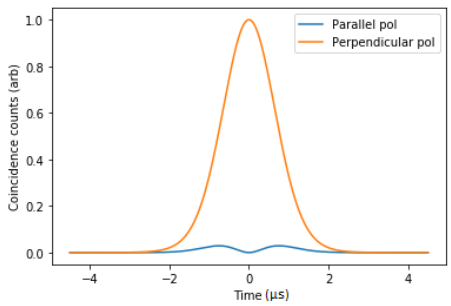

(d) Summed

Figure 4.16: HOM interference patterns for photons produced under different magnetic fields. (a,b) are photons produced under 4.72 and 5.06 Gauss, interfered with the centre photon, with V = 92.8% and 93.9% respectively. (c) shows the normal interference pattern between two photons produced at the centre value 4.893 Gauss, with V = 96.5%. (d) shows the weighted average over all possible combinations, with V = 96.4%.

small however, compared to the change in magnetic field. For example, Figure 4.16 a) is the interference pattern between a centre photon at 4.8934 G and a photon produced at 4.72 G, this difference in magnetic field is equivalent to a 100 mA change in the current in the Helmholtz coils and thus far exceeds any electrical noise that could be seen on the power supply, this along with the relatively small decrease in visibility of just 3.7% means that any noise we would reasonable have on the magnetic field should be negligible in terms of two photon interference.

To test this further, it should be possible to observe a quantum beat note in the interference pattern if the frequency difference between two photons is large enough [58]. Going to extreme values of the B-field, upwards of 8 G shows us a clear quantum beat note effect as can be seen in Figure 4.17.

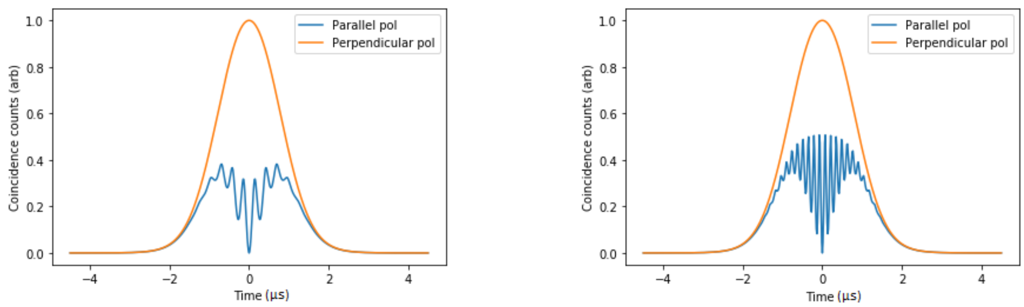

(a) $\Delta B = 1.72$ Gauss

(b) $\Delta B = 3.44$ Gauss

Figure 4.17: HOM interference patterns demonstrating a quantum beat note between two single photons of different frequencies.

4.7.2 Laser and Cavity Detunings

Another parameter which could introduce distinguishability between photons is the laser detuning used for the beam that drives the transition as well as the detuning for the cavity. It is common for some noise to be present on the laser frequency introduced by imperfect stability locking of the laser or through a noisy rf source used for the AOMs. Cavity mirrors can also drift over time. A difference in the detuning of the drive beam or the cavity will lead to photons produced at different frequencies, as was the case with changing the B-field. As shown in Figure 4.18, this leads to similar results.

For the actual experimental setup, the difference in detuning between two subsequent photons is significantly smaller than the maximum difference tested here, due to good stability locking of the laser and clean rf signals used for the AOMs. The cavity is also stability locked to the same system as the laser, meaning drifting over short time scales,

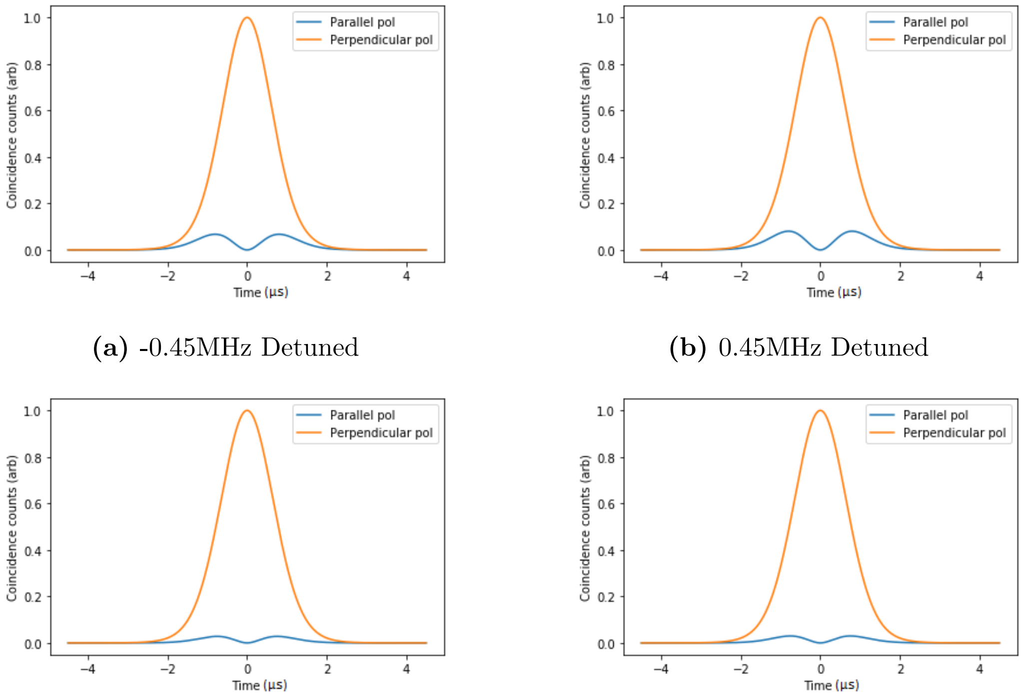

(a) -0.45MHz Detuned

(b) 0.45MHz Detuned

(c) Same Detuning

(d) Summed

Figure 4.18: HOM visibilities for photons of differing frequency due to cavity or laser detuning. (a,b) are produced with photons that are ± 0.45 MHz detuned from the centre photon with V = 90.8% and 89.4%. (c) is photons produced using the same detuning with V = 96.5% (d) is the weighted average over all possible combinations, with V = 96.3%

such as the length of a few drive cycles can be neglected when comparing two subsequent photons. If however, a large frequency shift has occurred, due to equipment malfunctioning etc. the resultant visibility is not impacted heavily, especially when averaged over many runs of the experiment.

Once again, going to extreme values of detuning, we observe a quantum beat note in the interference pattern as shown in Figure 4.19.

4.8 Conclusion

We have shown how careful selection of the initial state in a cavity-assisted Raman transition can significantly improve the indistinguishability of single photons. The improvement in visibility for the D-to-D scheme is useful in many quantum systems and networking, including probabilistic entanglement schemes and time-bin encoding. Through numerical simulations of the system, we have demonstrated that by reducing the effects of spontan-

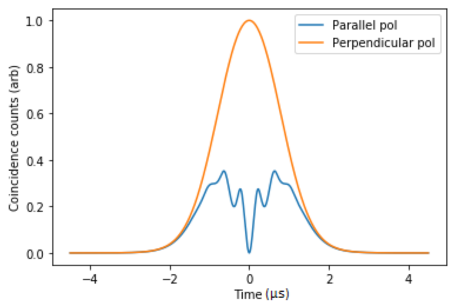

(a) -0.585MHz Detuned

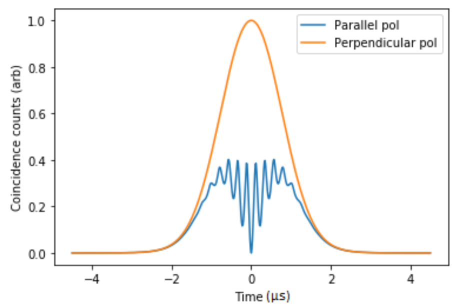

(b) -0.676MHz Detuned

Figure 4.19: HOM interference patterns demonstrating a quantum beat note between two single photons of different frequencies.

eous emission we can far outperform the commonly used S-to-D scheme in terms of both efficiency and visibility over the entire parameter space, with and without temporal filtering. To do this experimentally, coherent state transfer (STIRAP) must be implemented to increase state preparation fidelity, and allow us to prepare in a state with a more favourable Clebsch-Gordan coefficient. A visibility of 81(2)% is measured in this experiment and represents the highest visibility obtained experimentally by an ion-cavity system without subtracting background counts or applying temporal filtering.

Neutral atoms have previously held an advantage over trapped ions due to the ability to enter the strong coupling regime for optical cavities. With visibilities on the order of 80% [59, 60], this experiment brings a weakly-coupled ion-cavity system in line with neutral atoms. A combination of our scheme and a strongly coupled ion-cavity system such as [29] could lead to near unity HOM visibilities being possible, while also increasing single photon efficiencies.

Chapter 5

Time-bin encoding with an ion-cavity system

Quantum information encoding is an important aspect of quantum communication networks. Many encoding schemes exist, but suffer from decoherence effects and noise when implemented for long-distance communication. A typical scheme used in experiments such as quantum-key distribution (QKD) [61], encodes the quantum information in the polarisation state of a photon [62, 63]. Unfortunately, thermal or mechanical stress induces a time-dependent birefringence in optical fibres, which serves to scramble the intended quantum state. Other effects such as polarisation mode dispersion [64] also change the polarisation state of the photons. For this reason, time-bin phase encoding is regarded as the optimal choice for long-distance communication networks as it is much more robust to environmental factors [65, 66, 67, 68] and does not suffer from false heralding unlike photon number encoding, where the absence of a photon corresponds to a state.

In this chapter, we demonstrate the ability to produce accurately prepared arbitrary photonic qubit states straight from an ion-cavity system using time-bin phase encoding. A HOM interference measurement is performed again, this time to measure the applied phase difference to a time-bin of one photon. Similar to chapter 4, two schemes will be compared and the effect of spontaneous emission on the output qubit state will be shown.

5.1 Time-bin Encoding

In typical experiments which employ time-bin phase encoding, a single photon source is connected to a short, unbalanced Mach-Zehnder (MZ) interferometer see Figure 5.1. This

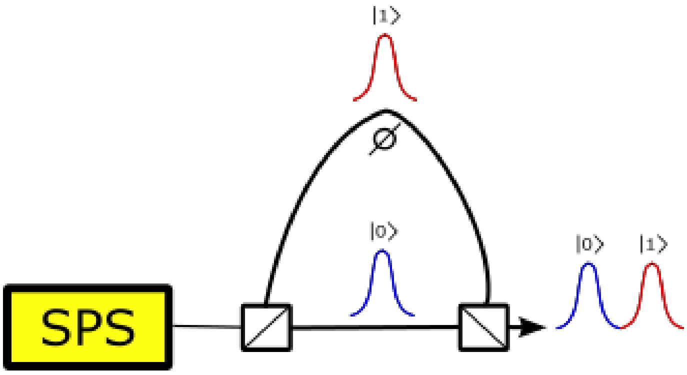

Figure 5.1: An example of a general, short, unbalanced Mach-Zehnder interferometer to produce time-bin encoded photons. A single photon source releases a photon into the setup where it is split into two paths. A direct path leads straight to the output splitter and represents the time-bin $|0\rangle$. A second arm, elongated compared to the first, delays the photon before entering the output splitter and represents the time-bin $|1\rangle$. An optional phase ϕ can be applied to this arm to create a unique qubit state described by Equation 5.2.

produces a photon in a superposition of two time bins. We can write this state

$$|\psi\rangle = \alpha\,|0\rangle + \beta\,|1\rangle \tag{5.1}$$

where α and β are the amplitudes for each state. In general, it is difficult to alter these amplitudes as they are set by the optical components chosen. To gain control over this superposition, a phase shift along one path of the MZ interferometer can be implemented, allowing arbitrary control over the qubit state. This new state can be written

$$|\psi\rangle = \frac{|0\rangle + e^{i\phi}\,|1\rangle}{\sqrt{2}} \tag{5.2}$$

where ϕ is a chosen phase. This phase is used in many applications, such as QKD, whereby using a second MZ interferometer on the receiver end you can select a measurement basis [68, 69], although the specifics for any implementations will not be discussed in this thesis. In this experiment, we remove the need for a MZ interferometer on the sender side of a quantum communication link. Instead, the single photon itself is generated with two distinct time-bins by shaping the amplitude of the laser beam driving a cavity-assisted Raman transition. An arbitrary phase can be applied during the photon generation process to reproduce the same qubit state in Equation 5.2. It should be noted any number of time-bins can be generated, with individual phases applied, resulting in qutrit and ququad etc states such as in [70].

5.2 Phase Dependent HOM Interference Patterns

To perform entanglements or use communication protocols we must verify the qubit state we are producing and compare against the intended output. Measuring the amplitudes of the qubits states $|0\rangle$ and $|1\rangle$ is trivial. We must simply repeat the single photon generation sequence and record photon arrival times. Doing this, we can reconstruct the photons probability distribution, such as in Chapter 4, and compare the size of the two time-bins, we may then alter the parameters to achieve any intended distribution, although this normally remains as 50:50.

A more complicated measurement, is that of the applied phase shift to the second time-bin. Following [70], we can use a HOM interference experiment to extract this phase information. To do this, a reference photon, with no applied phase shift, is interfered at a 50:50 beamsplitter with a signal photon, one which has a chosen phase applied to the second time-bin. To predict the outcome of this experiment we must follow a similar procedure followed in Chapter 4. We start by defining the two input modes of the beamsplitter

$$\hat{a}^\dagger = \frac{1}{\sqrt{2}}(\hat{a_1}^\dagger + \hat{a_2}^\dagger) \tag{5.3}$$

$$\hat{b}^\dagger = \frac{1}{\sqrt{2}}(\hat{b_1}^\dagger + e^{i\phi}\hat{b_2}^\dagger) \tag{5.4}$$

where $\hat{a}^\dagger$ and $\hat{b}^\dagger$ represents the input mode for the reference and signal photon respectively, and the subscripts (1,2) refer to the time-bin. Using this we write the input state as

$$\hat{a}^\dagger\hat{b}^\dagger |00\rangle_{BS} = \frac{1}{2}(\hat{a_1}^\dagger + \hat{a_2}^\dagger)(\hat{b_1}^\dagger + e^{i\phi}\hat{b_2}^\dagger) |00\rangle_{BS} \tag{5.5}$$

We can use the beamsplitter input-output relations (Equation 4.1) to write $\hat{a}^\dagger$ and $\hat{b}^\dagger$ in terms of the output modes $\hat{c}^\dagger$ and $\hat{d}^\dagger$

$$\hat{a_1}^\dagger = \frac{1}{\sqrt{2}}(\hat{c_1}^\dagger + \hat{d_1}^\dagger) \qquad \hat{a_2}^\dagger = \frac{1}{\sqrt{2}}(\hat{c_2}^\dagger + \hat{d_2}^\dagger) \tag{5.6}$$

$$\hat{b_1}^\dagger = \frac{1}{\sqrt{2}}(\hat{c_1}^\dagger - \hat{d_1}^\dagger) \qquad \hat{b_2}^\dagger = \frac{e^{i\phi}}{\sqrt{2}}(\hat{c_2}^\dagger - \hat{d_2}^\dagger) \tag{5.7}$$

Substituting these into the input state Equation 5.5 we obtain

$$\hat{a}^\dagger\hat{b}^\dagger |00\rangle_{BS} = \frac{1}{4}\left((\hat{c_1}^\dagger + \hat{d_1}^\dagger) + (\hat{c_2}^\dagger + \hat{d_2}^\dagger)\right)\left((\hat{c_1}^\dagger - \hat{d_1}^\dagger) + e^{i\phi}(\hat{c_2}^\dagger - \hat{d_2}^\dagger)\right) \tag{5.8}$$

Expanding this out and grouping relevant terms together we obtain

$$\begin{aligned}\hat{a}^\dagger\hat{b}^\dagger |00\rangle_{BS} =& \frac{1}{4}\left((\hat{c_1}^\dagger)^2 - (\hat{d_1}^\dagger)^2\right) + e^{i\phi}\left((\hat{c_2}^\dagger)^2 - (\hat{d_2}^\dagger)^2\right) \\ &+ \left(\hat{c_1}^\dagger\hat{c_2}^\dagger - \hat{d_1}^\dagger\hat{d_2}^\dagger\right)\left(1 + e^{i\phi}\right) \\ &- \left(\hat{c_2}^\dagger\hat{d_1}^\dagger - \hat{d_2}^\dagger\hat{c_1}^\dagger\right)\left(1 - e^{i\phi}\right)\end{aligned} \tag{5.9}$$

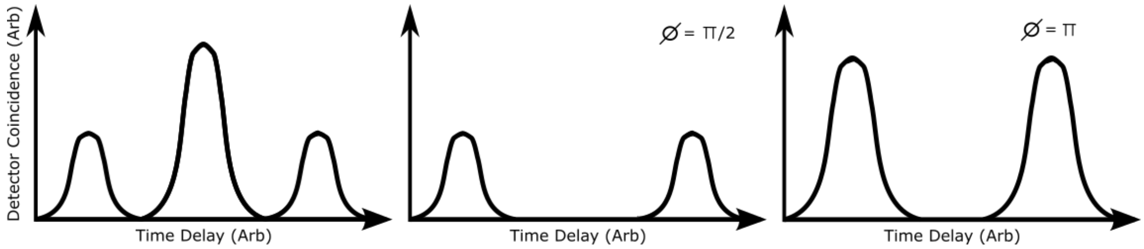

Figure 5.2: A representation of three scenarios resulting HOM interference patterns. A reference measurement (left) performed with distinguishable single photons takes the form of the auto correlation of the photon shape. Two measurements, performed with identical single photons and a varying phase on time-bin two of one single photon, with $\phi = \pi/2$ (Middle) and $\phi = \pi$ (Right) show differing amplitudes for the satellite peaks depending in the phase applied.

The first line of this equation corresponds to the times when both photons are detected within the same time bin, in this case they coalesce and are always detected in the same output port. The second and third lines correspond to the times where the photons are detected in different time bins. It is apparent that in this case the detections rely on the applied phase difference. With $\phi = 0$, no cross-correlations are detected, as expected with HOM interference. If however $\phi = \pi$, the photons are instead forced into opposite output ports.

The interference patterns produced by this are then a direct measure of the phase that has been applied. For distinguishable photons (i.e polarisations are perpendicular), the shape takes the form of the auto-correlation of the photon shape, in this case a triple peak structure. The centre peak of which, are photons detected in the same time-bin, while the two smaller satellite peaks are those of photons in different time-bins. A representative set of graphs for varying applied phases is presented in Figure 5.2. This allows us to compare the interference patterns and extract the phase applied, thereby confirming the preparation of our qubit state.

5.3 Experimental Setup

The experimental setup is largely identical to that of the previous chapter. Some modifications were implemented to improve several aspects of the experiment. The setup can be seen in Figure 5.3. Firstly, the 866 nm Raman drive beam for the D-to-D scheme was moved to be perpendicular to the cavity axis (magnetic field direction), this improves the purity of the polarisation seen by the ion and reduces driving unwanted transitions. Furthermore, this laser and the 397 nm drive beam for the S-to-D scheme are switched

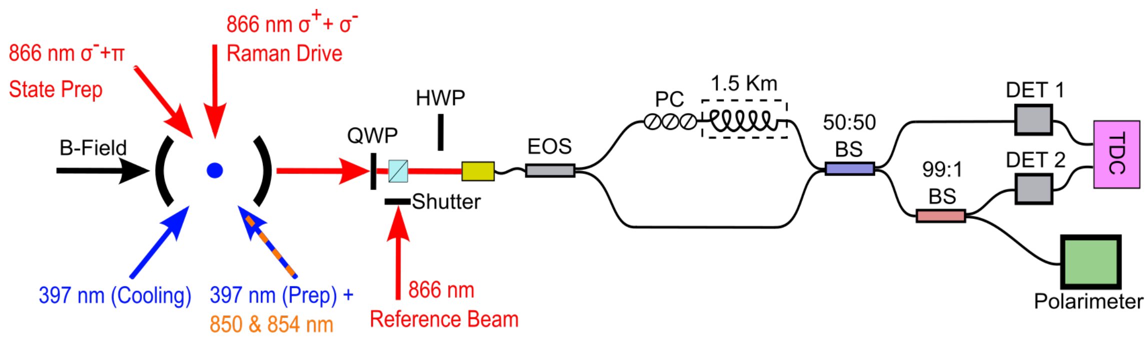

Figure 5.3: Ion trap and HOM interference setup. Orientation and polarisation of the lasers is indicated for the D-to-D scheme.

to being driven by a DDS (direct digital synthesizer) board and an amplifier. The DDS board allows fast switching between different profiles, this can be used to quickly change the driving frequency or amplitude, but in this case is used to change the phase of the driving RF wave. The DDS chip is phase referenced and so it is possible to accurately shift the phase and maintain a phase relationship with the original RF signal. Lastly, the HOM interference setup was completely respliced with new fibre components. All PM beamsplitters were replaced with SM 780HP variants. This was to reduce the effects of polarisation mode dispersion caused by slight inaccuracies when splicing the fibres. Doing this means the polarisation in the direct arm drifts with respect to the delay arm now, but is easily compensated for during data collection with the polarisation altering paddles. Overall, this increased the DOP (degree of polarisation) as measured by the polarimeter and should aid with polarisation errors in the experiment.

5.4 Single photon generation sequence

The laser pulse sequence for each scheme is depicted in Figure 5.4. As in the previous experiment, an FPGA controls most of the lasers via RF switches. The Raman drive lasers for both schemes are driven by a DDS board in order to implement fast phase switching. To increase state preparation fidelity a dual-drive cycle has been implemented. This is where two single photons generation cycles occur for every one cooling cycle, this increases the amount of time we have to prepare the ion in the desired state. Cavity visibility measurements, as described in Chapter 3 were taken during this cycle and found no measurable increase in temperature. The new sequence length is 16.8 μs, the single photons are still generated 7.38 μs apart, as to arrive at the beamsplitter together. The TDCs are once again gated during the single photon emission, and the applied magnetic field remains at 4.9 G. Initially, the ion is Doppler cooled for 1.5μs with a 397 nm beam blue-detuned

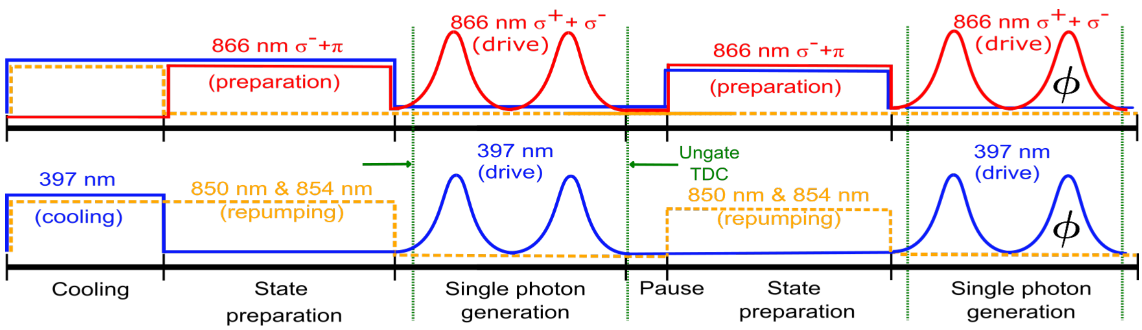

Figure 5.4: Laser pulse sequences for D-to-D (Top) and S-to-D (Bottom) schemes. Relevant polarisation information is depicted. A phase shift ϕ is applied to time-bin two of the second generated photon.

by $\Delta_{cool} = 2\gamma_{SP}$ from resonance. The population is repumped back into the cooling cycle using beams at 850 and 854 nm. For the D-to-D scheme, the repumpers are then switched off and an on-resonance 866 nm laser prepares the ion in the $|D_{3/2}, m_j = -3/2\rangle$ for 3.3μs while a 397 nm beam pumps any population lost to spontaneous emission back into the $|D_{3/2}\rangle$ manifold. The single photon is then generated with a second 866 nm beam, red-detuned by $\Delta_{drive} = 2\gamma_{SP}$, driving a cavity-assisted Raman transition between $|D_{3/2}, m_j = -3/2\rangle$ and $|D_{3/2}, m_j = 1/2\rangle$. A short delay is added before and after photon generation to ensure the cavity population has decayed, and no other lasers are on during the photon generation process. We then re-enter the state preparation phase and prepare the ion back into the $|D_{3/2}, m_j = -3/2\rangle$ state. A second photon is then generated using the same parameters, however during this generation the phase of the driving RF can be switched between time-bins. The intensity of the drive laser for the cavity-assisted Raman transition is given a dual-Gaussian temporal shape, with 700ns wide peaks at FWHM and separated by 1.8μs, measured using a fast photodetector. Amplitudes of the first and second peak are $\Omega = 2\pi \times 1.56\,\text{MHz}$ and $\Omega = 2\pi \times 3.12\,\text{MHz}$ respectively. The parameters of the drive pulse are chosen to produce photons with equal probabilities of residing in either time-bin. This shaping is achieved by mixing the output of a Rigol DG4162 function generator with the DDS output. An overall detection efficiency of $\approx 0.061\%$ is achieved.

For comparison, we also use the more conventional S-to-D scheme. First, the ion is Doppler cooled as in the D-to-D scheme. The ion is then state prepared for 3.3μs into a mix of the $|S_{1/2}\rangle$ states by turning the cooling 397 nm beam off and allowing the repumpers to completely populate the ground states. The single photon is then generated through a cavity-assisted Raman transition between $|S_{1/2}, m_j = -1/2\rangle$ and $|D_{3/2}, m_j = 1/2\rangle$ using a 397 nm beam for 3.3μs. The intensity of this laser is given a dual Gaussian temporal

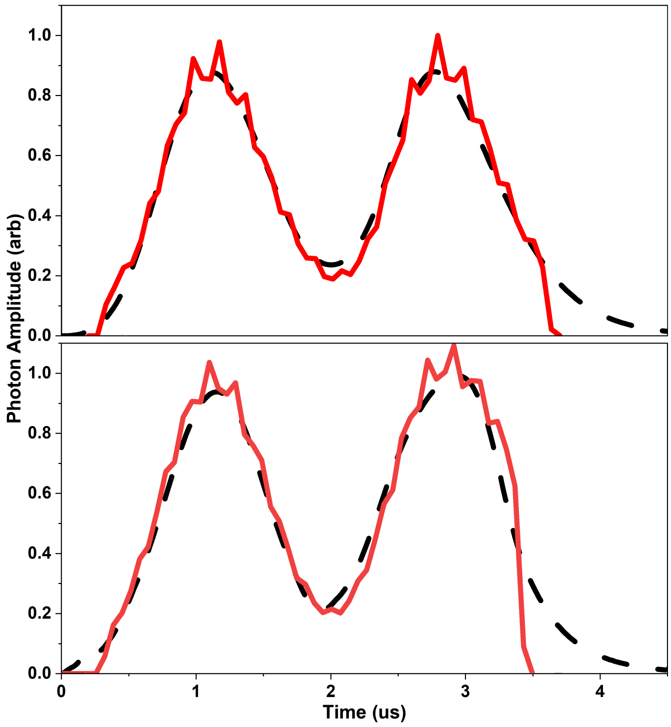

Figure 5.5: Temporal probability distribution of detecting single photon shown as a solid line for the D-to-D scheme (Top) and S-to-D (Bottom). To extract this plot, all the photon arrival times with respect to the sequence trigger during the measurements are sorted into 60 ns time bins and the resulting histograms are normalised. The dashed lines are obtained by numerical simulation.

shape, with 700 ns wide peaks (FWHM) and amplitudes of $\Omega = 2\pi \times 5.93\,\text{MHz}$ and $\Omega = 2\pi \times 11.86\,\text{MHz}$ for the first and second peak respectively, red detuned 24 MHz from resonance. An overall detection efficiency of $\approx 0.37\%$ is achieved.

5.5 Results

As in Chapter 4, the raw data is the photon arrival times detected by the TDC and gated during the generation window. For this experiment, due to the newly implemented dual drive cycle, photons no longer arrive in multiples of the sequence length and we instead focus on the centre of the produced histogram. Once again we implement a trigger signal every 256 cycles which allows us to reconstruct the photons temporal shape, these can be seen for both schemes in Figure 5.5. It should be noted that the second time-bin for the S-to-D photon is wider by roughly 150 ns. This is due to slightly different photon generation dynamics, although this will not effect the interference patterns produced by this scheme.

5.5.1 HOM interference patterns

After changing the interferometry components the polarisation dependent branching ratios and losses become negligible and we no longer need to consider this when normalising the data. Instead, we simply scale the data based on the number of photons detected for each scenario. The interference patterns for the D-to-D scheme can be seen in Figure 5.6. The histograms are plotted with 450 ns bin widths and the error bars are the counting statistics error.

As expected, for completely distinguishable photons (perpendicular polarisation) a triple peak structure is witnessed corresponding to the classical statistics of detecting the photons in either time-bin. As seen in chapter 4, identical single photons ($\phi = 0$) interfering on a beamsplitter, results in no cross-correlations being observed. Due to the constraints of the delay fibre, imperfect state preparation leads to an increase in visibility and thus coincidence counts. A state preparation fidelity of 85% is estimated. The overall structure agrees well with the simulated coincidences, however the experimental data points lie consistently above the simulated values. This is suspected to be due to drifts in both the state preparation fidelity and polarisation mismatch over long measurement times needed to gather sufficient statistics. The final scenario, where a phase flip ($\phi = \pi$) is applied to time-bin two of the second photon shows good agreement between simulation and experiment. Here, we can see the effect of the satellite peaks increasing in size over the perpendicular measurement as the photons are forced into opposite output ports, as predicted by Equation 5.9. This feature combined with the absence of a centre peak clearly indicates that we have accurately applied a phase shift and it demonstrates our ability to create arbitrary photonic qubit states of the form in equation 5.2.

Unfortunately, due to the limited time we have to produce single photons, the interference patterns become less resolved as the triple peak shape comes closer together. This effect could be reduced by either making the delay line longer, or making each time-bin narrower and separating the time-bins by a larger amount. This however, negatively impacts our photon detection efficiency and thus significantly reduces the coincidence detection rate, so instead the parameters were chosen to maximise this efficiency while keeping the structure somewhat resolvable.

To demonstrate the detrimental effect of spontaneous emission on the single photon emission process, we perform the same three scenarios but with the S-to-D scheme. The HOM interference patterns can be seen in Figure 5.7. The histograms are scaled as in the D-to-D scheme and are plotted with 200 ns bin widths, with error bars of the counting

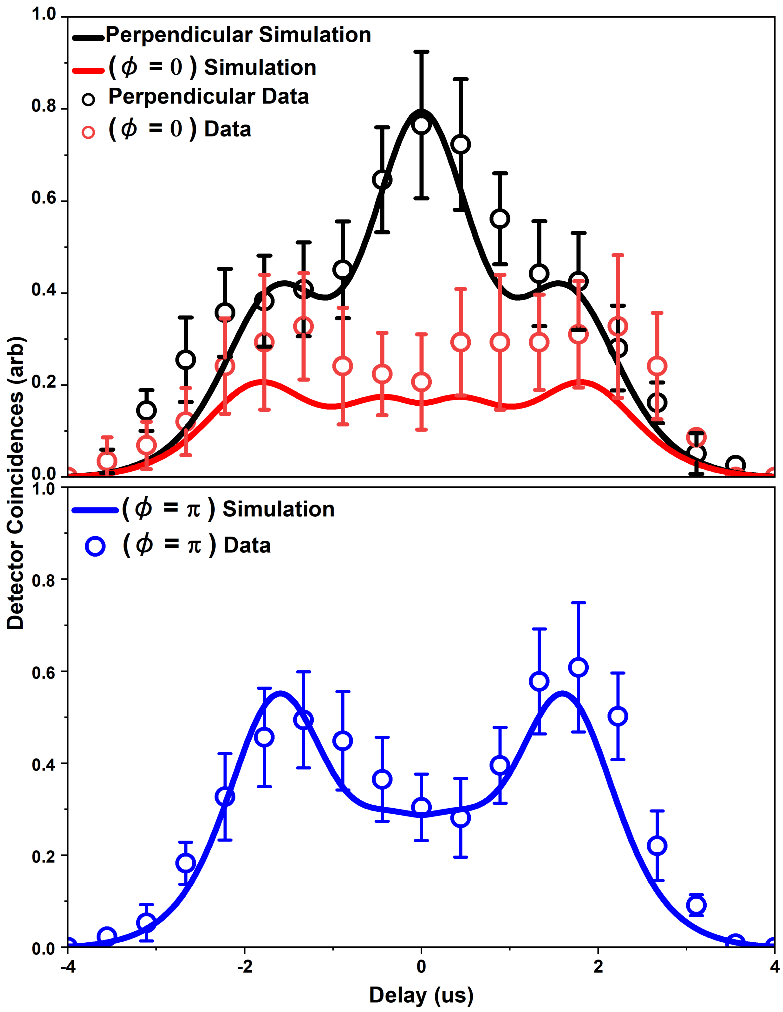

Figure 5.6: Hong-Ou-Mandel interference patterns for D-to-D scheme. Solid lines are obtained from numerical simulations of the system. Experimental data for parallel polarised photons, $\phi = 0$ (Top, Red) and $\phi = \pi$ (Bottom, Blue) is then scaled to the simulations and smoothed using an adjacent-averaging technique. Perpendicular polarised photons (Top, Black) are plotted for reference, using the same technique as before.

statistics. It can be seen that due to the slightly wider photons being produced in this scheme the three peak structure is less resolved. However, there is no statistical difference between the scenarios with and without a phase flip. This agrees well with the simulations that indicate the interference patterns should be exactly the same. This indicates that the coherence time of the generated photons in this scheme are much shorter than the time bin separation. During the generation process, many spontaneous decay events can occur, this resets the cavity emission process and destroys any phase relationship that exists between the time-bins. In comparison, the D-to-D schemes chance of spontaneous emission back to the initial state is small and a phase relationship across the entire photon is easily maintained.

5.6 Conclusion

We have shown full control of the single photon generation process in an ion-cavity system for the first time. In addition to polarisation and temporal profile control, we have shown the ability to control phase during the generation process and the possibility of creating arbitrary qubit states. It has been shown that due to spontaneous emission, a conventional scheme such as S-to-D has a reduced coherence time and is unsuitable for time-bin phase encoding. By carefully selecting the initial state of our scheme to reduce the impact of the decay events, we are able to demonstrate a coherence time longer than the temporal length of the photons, this maintains the phase relationship between time-bins. With this, we have shown that time-bin phase encoding schemes are possible with ion-cavity systems for the first time.

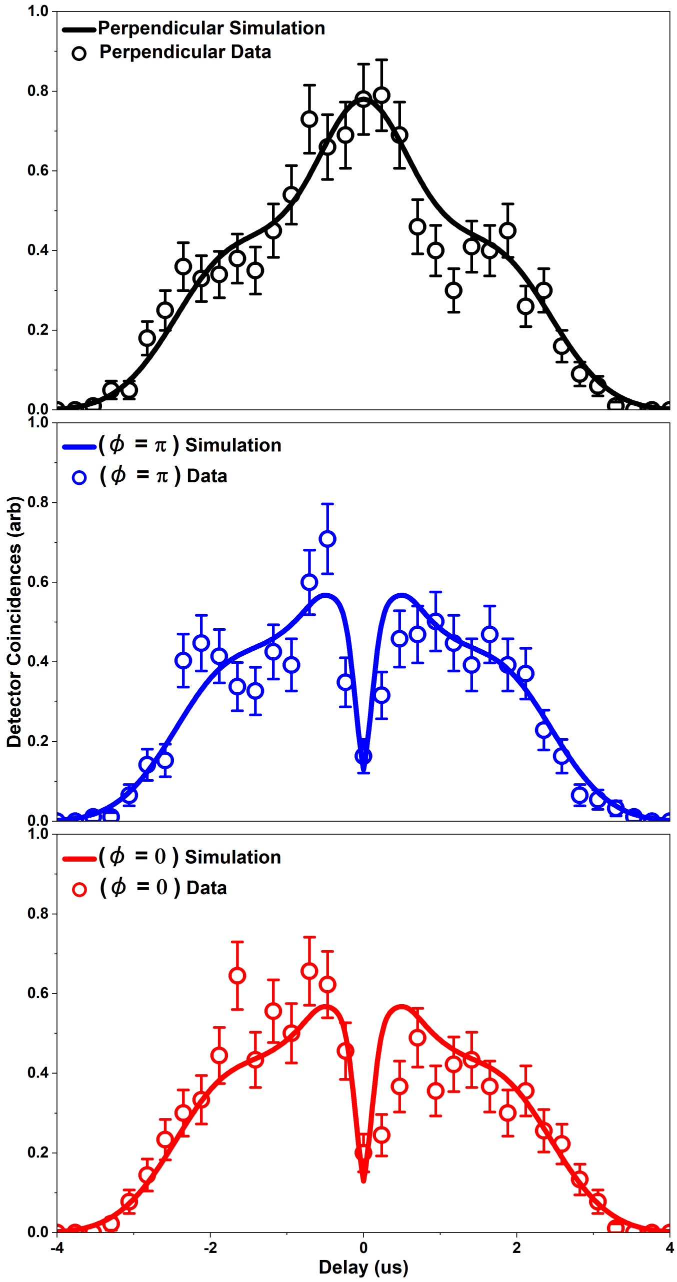

Figure 5.7: Hong-Ou-Mandel interference patterns for S-to-D scheme. Solid lines are the numerical simulations of the system. Experimental data for perpendicularly polarised photons (Top, Black) and parallel polarised photons with $\phi = \pi$ (Middle, Blue) and without $\phi = 0$ (Bottom, Red) phase flip is then scaled to the simulations.

Chapter 6

Conclusion

At the start of my doctoral work the trap and associated systems were already built and functioning, with several experiments [25] and theses [38, 4, 3] already completed. During my work several adjustments were made, including introducing new laser systems and implementing tapered amplifiers to increase available power, improvements to the stable frequency reference and implementing FPGA control over the laser sequences and photo-detection events. The motivation of this work was to develop and demonstrate a trapped ion-cavity network node and show improvements to the single photon generation process and the ability to create arbitrary qubit states for time-bin-phase encoding techniques. This was achieved over two experiments where the analysis of HOM interference signals was used.

In the first experiment, it was shown that through careful selection of the initial state of the ion in a cavity-assisted Raman transition, the indistinguishability can be significantly improved. This new technique mitigates the harmful effects of spontaneous emission, which drastically hampers the photons coherence time. A HOM visibility of 81(2)% is achieved with this new scheme, while a more conventional scheme using the same trap achieved a visibility of only 50(2)%. Comparing these results to techniques that limit the time-window in which you look at the coincidences counts results in a clear win for our new technique, for every possible combination of parameters, the new technique outperforms the more conventional scheme. This technique is easily applied to other ion species and leads the way for ion-cavity systems in general to produce better single photons.

The second experiment demonstrates the systems use as an arbitrary qubit state generator for time-bin-phase encoding techniques. It is shown that photons can be selectively produced with equal probability of residing in either time-bin and with an applied phase to one time-bin. This was demonstrated by another HOM interference measurement, where we showed accurate and coherent control over this applied phase. The generation of this qubit state was then compared to a state generation using the more conventional scheme, which showed no clear distinction between any applied phase shift, thus indicating the destruction of any phase relationship. A similar experiment has been performed with neutral atom systems [70], but this is the first demonstration with an ion-cavity system. This experiment lays the foundation for ion-cavity systems to replace more standard setups for generating time-bin encoded photons such as Mach-Zender interferometers, due to their superior control, stability and ability to change the output state without physically replacing parts of a setup.

There are several paths the current trap setup could take moving into the future. Currently an ion-photon entanglement experiment is being set up and tested, I have heavily contributed to the system changes and implementations of this system. After this, ion-ion entanglement between this and another distant trap remains a sensible near term goal, where long distance entanglement of an ion and photon has already been demonstrated in [47]. In this case, the previously performed frequency conversion [1, 25] would be a useful addition to re-implement in this case. Other future options include returning to the coupling of multiple ions to the optical cavity and using this to generate multi-ion cluster states, useful in both computing and networking.

The field of trapped ions is expanding rapidly, with many exciting new experiments being developed and start-up companies being spun out. I am in no doubt that trapped ions for both quantum computing and networking will compete fiercely with other qubit modalities. It is an incredibly exciting time to be working in the field and I look forward to seeing all the new innovation being developed.

Bibliography

[1] Thomas Walker. *Single photons from a trapped-ion cavity-QED system.* PhD thesis, University of Sussex, March 2021. viii, ix, x, xi, 4, 5, 6, 7, 11, 19, 21, 26, 35, 40, 41, 42, 45, 47, 54, 56, 75

[2] Philipp Müller and Jürgen Eschner. Single calcium-40 ion as quantum memory for photon polarization: a case study. *Applied Physics B*, 114(1-2):303–306, nov 2013. viii, 6

[3] Markus O Vogt. *Toward coherent ion-cavity coupling.* PhD thesis, University of Sussex, May 2017. viii, ix, x, 4, 16, 17, 20, 28, 29, 32, 36, 38, 74

[4] Nicolas R Seymour-Smith. *Ion-trap cavity QED system for probabilistic entanglement.* PhD thesis, University of Sussex, May 2012. viii, ix, x, 4, 16, 18, 20, 28, 30, 31, 32, 33, 74

[5] S. W. Hawking. The quantum mechanics of black holes. *Scientific American*, 236(1):34–42, 1977. 1

[6] Maulik Parikh, Frank Wilczek, and George Zahariade. Quantum mechanics of gravitational waves. *Phys. Rev. Lett.*, 127:081602, Aug 2021. 1

[7] Johnjoe Mcfadden and Jim Al-Khalili. The origins of quantum biology. *Proceedings of the Royal Society A: Mathematical, Physical and Engineering Sciences*, 474, 12 2018. 1

[8] F. Giustino, J. H. Lee, F. Trier, M. Bibes, S. M. Winter, R. Valentí, Y.-W. Son, L. Tailleferand C. Heil, A. I. Figueroa, B. Plaçais, Q. S. Wu, O. V. Yazyev, E. P. Bakkers, J. Nygård, P. Forn-Díazand S. De Franceschi, J. W. McIver, L. E. Torres, T. Low, A. Kumar, R. Galceran, S. O. Valenzuela, M. V. Costache, A. Manchon, E.-A. Kim, G. R. Schleder, A. Fazzio, and S. Roche. The 2021 quantum materials roadmap. *J. Phys. Mater*, 3, 01 2021. 1

[9] Thomas Coussens, Christopher Abel, Aikaterini Gialopsou, Mark G. Bason, Tim M. James, Fedja Orucevic, and Peter Kruger. Modular optically-pumped magnetometer system, 2021. 1

[10] Yu-Ming Huang, Konthoujam James Singh, An-Chen Liu, Chien-Chung Lin, Zhong Chen, Kai Wang, Yue Lin, Zhaojun Liu, Tingzhu Wu, and Hao-Chung Kuo. Advances in quantum-dot-based displays. *Nanomaterials*, 10(7), 2020. 1

[11] Nishi Shah. Moore's law is ending: What's next after finfets. In Kohei Arai, Supriya Kapoor, and Rahul Bhatia, editors, *Proceedings of the Future Technologies Conference (FTC) 2020, Volume 2*, pages 340–346. Springer International Publishing, 2021. 1

[12] Richard P. Feynman. Quantum mechanical computers. *Foundations of Physics*, 16(6):507–531, 1986. 1

[13] Peter W. Shor. Polynomial-time algorithms for prime factorization and discrete logarithms on a quantum computer. *J.Sci.Statist.Comput*, 26, 1995. 1

[14] Ivan Kassal, Stephen P. Jordan, Peter J. Love, Masoud Mohseni, and Alá n Aspuru-Guzik. Polynomial-time quantum algorithm for the simulation of chemical dynamics. *Proceedings of the National Academy of Sciences*, 105(48):18681–18686, dec 2008. 1

[15] A Perdomo-Ortiz, N Dickson, M Drew-Brook, G Rose, and A Aspuru-Guzik. Finding low-energy conformations of lattice protein models by quantum annealing. *Scientific Reports*, 2, 8 2012. 1

[16] L.-M. Duan, M. D. Lukin, J. I. Cirac, and P. Zoller. Long-distance quantum communication with atomic ensembles and linear optics. *Nature*, 414(6862):413–418, nov 2001. 1, 3

[17] M. Aspelmeyer, T. Jennewein, M. Pfennigbauer, W.R. Leeb, and A. Zeilinger. Long-distance quantum communication with entangled photons using satellites. *IEEE Journal of Selected Topics in Quantum Electronics*, 9(6):1541–1551, nov 2003. 1

[18] C. Monroe, R. Raussendorf, A. Ruthven, K. R. Brown, P. Maunz, L.-M. Duan, and J. Kim. Large-scale modular quantum-computer architecture with atomic memory and photonic interconnects. *Phys. Rev. A*, 89:022317, Feb 2014. 1

[19] David P. DiVincenzo. The physical implementation of quantum computation. *Fortschritte der Physik*, 2 2000. 1

[20] A. H. Myerson, D. J. Szwer, S. C. Webster, D. T. C. Allcock, M. J. Curtis, G. Imreh, J. A. Sherman, D. N. Stacey, A. M. Steane, and D. M. Lucas. High-fidelity readout of trapped-ion qubits. *Phys.Rev.Lett*, 100, 5 2008. 2

[21] T.P. Harty, D.T.C. Allcock, C.J. Ballance, L. Guidoni, H.A. Janacek, N.M. Linke, D.N. Stacey, and D.M. Lucas. High-fidelity preparation, gates, memory, and readout of a trapped-ion quantum bit. *Phys.Rev.lett*, 113, 11 2014. 2

[22] S. Crain, C. Cahall, G. Vrijsen, E. Wollman, M. Shaw, V. Verma, S. Nam, and J. Kim. High-speed, low-crosstalk detection of a trapped 171 yb+ ion ancilla qubit using superconducting nanowire single photon detectors. *Nature*, 2 2019. 2

[23] K. R. Brown, A. C. Wilson, Y. Colombe, C. Ospelkaus, A. M. Meier, E. Knill, D. Leibfried, and D. J. Wineland. Single-qubit-gate error below $10^-4inatrappedion. Phys.Rev.A, 42011. 2$

[24] V. M. Schafer, C. J. Ballance, K. Thirumalai, L. J. Stephenson, T. G. Ballance, A. M. Steane, and D. M. Lucas. Fast quantum logic gates with trapped-ion qubits. *Nature*, 9 2017. 2

[25] Thomas Walker, Koichiro Miyanishi, Rikizo Ikuta, Hiroki Takahashi, Samir Vartabi Kashanian, Yoshiaki Tsujimoto, Kazuhiro Hayasaka, Takashi Yamamoto, Nobuyuki Imoto, and Matthias Keller. Long-distance single photon transmission from a trapped ion via quantum frequency conversion. *Physical Review Letters*, 120(20), may 2018. 2, 74, 75

[26] Anaïs Dré au, Anna Tcheborateva, Aboubakr El Mahdaoui, Cristian Bonato, and Ronald Hanson. Quantum frequency conversion of single photons from a nitrogen-vacancy center in diamond to telecommunication wavelengths. *Physical Review Applied*, 9(6), jun 2018. 2

[27] Paul Fisher, Robert Cernansky, Ben Haylock, and Mirko Lobino. Single photon frequency conversion for frequency multiplexed quantum networks in the telecom band. *Phys. Rev. Lett.*, 127:023602, Jul 2021. 2

[28] J. I. Cirac, P. Zoller, H. J. Kimble, and H. Mabuchi. Quantum state transfer and entanglement distribution among distant nodes in a quantum network. *Physical Review Letters*, 78(16):3221–3224, apr 1997. 2

[29] Hiroki Takahashi, Ezra Kassa, Costas Christoforou, and Matthias Keller. Strong coupling of a single ion to an optical cavity. *Physical Review Letters*, 124(1), jan 2020. 3, 62

[30] A. D. Boozer, A. Boca, R. Miller, T. E. Northup, and H. J. Kimble. Reversible state transfer between light and a single trapped atom. *Physical Review Letters*, 98(19), may 2007. 3

[31] L.-M. Duan and H. J. Kimble. Efficient engineering of multiatom entanglement through single-photon detections. *Physical Review Letters*, 90(25), jun 2003. 3

[32] L. J. Stephenson, D. P. Nadlinger, B. C. Nichol, S. An, P. Drmota, T. G. Ballance, K. Thirumalai, J. F. Goodwin, D. M. Lucas, and C. J. Ballance. High-rate, high-fidelity entanglement of qubits across an elementary quantum network. *Physical Review Letters*, 124(11), mar 2020. 3

[33] S. Pirandola, U. L. Andersen, L. Banchi, M. Berta, D. Bunandar, R. Colbeck, D. Englund, T. Gehring, C. Lupo, C. Ottaviani, J. L. Pereira, M. Razavi, J. Shamsul Shaari, M. Tomamichel, V. C. Usenko, G. Vallone, P. Villoresi, and P. Wallden. Advances in quantum cryptography. *Advances in Optics and Photonics*, 12(4):1012, dec 2020. 3

[34] Hitesh Singh, D.L. Gupta, and A.K Singh. Quantum key distribution protocols: A review. *IOSR Journal of Computer Engineering*, 16:01–09, 01 2014. 3

[35] Eleni Diamanti, Hoi-Kwong Lo, Bing Qi, and Zhiliang Yuan. Practical challenges in quantum key distribution. *npj Quantum Information*, 2(1), nov 2016. 3

[36] J Robert Johansson, Paul D Nation, and Franco Nori. Qutip 2: A python framework for the dynamics of open quantum systems. *Computer Physics Communications*, 184(4):1234–1240, 2013. 4

[37] Daniel Manzano. A short introduction to the lindblad master equation. *AIP Advances*, 10(2):025106, feb 2020. 10

[38] Stephen Patrick Begley. *Optimisation of the coupling of ion strings to an optical cavity.* PhD thesis, University of Sussex, June 2016. 16, 22, 74

[39] P F Herskind, A Dantan, M Albert, J P Marler, and M Drewsen. Positioning of the rf potential minimum line of a linear paul trap with micrometer precision. *Journal of Physics B: Atomic, Molecular and Optical Physics*, 42(15):154008, jul 2009. 19

[40] D Berkeland, J Miller, James Bergquist, Wayne Itano, and David Wineland. Minimization of ion micromotion in a paul trap. *Journal of Applied Physics*, (83), 1998-01-01 00:01:00 1998. 22

[41] E. A. Donley, T. P. Heavner, F. Levi, M. O. Tataw, and S. R. Jefferts. Double-pass acousto-optic modulator system. *Review of Scientific Instruments*, 76(6):063112, 2005. 26

[42] Ezra Kassa. *Single ion coupled to a high-finesse optical fibre cavity for cQED in the strong coupling regime*. PhD thesis, University of Sussex, July 2017. 33

[43] F. Schmidt-Kaler, J. Eschner, G. Morigi, C.F. Roos, D. Leibfried, A. Mundt, and R. Blatt. Laser cooling with electromagnetically induced transparency: application to trapped samples of ions or neutral atoms. *Applied Physics B*, 73(8):807–814, dec 2001. 38

[44] E. Peik, J. Abel, Th. Becker, J. von Zanthier, and H. Walther. Sideband cooling of ions in radio-frequency traps. *Phys. Rev. A*, 60:439–449, Jul 1999. 38

[45] A. Stute, B. Casabone, P. Schindler, T. Monz, P. O. Schmidt, B. Brandstätter, T. E. Northup, and R. Blatt. Tunable ion–photon entanglement in an optical cavity. *Nature*, 485(7399):482–485, may 2012. 39

[46] Matthias Bock, Pascal Eich, Stephan Kucera, Matthias Kreis, Andreas Lenhard, Christoph Becher, and Jürgen Eschner. High-fidelity entanglement between a trapped ion and a telecom photon via quantum frequency conversion. *Nature Communications*, 9(1), may 2018. 39

[47] V. Krutyanskiy, M. Meraner, J. Schupp, V. Krcmarsky, H. Hainzer, and B. P. Lanyon. Light-matter entanglement over 50 km of optical fibre. *npj Quantum Information*, 5(1), aug 2019. 39, 75

[48] C. K. Hong, Z. Y. Ou, and L. Mandel. Measurement of subpicosecond time intervals between two photons by interference. *Phys. Rev. Lett.*, 59:2044–2046, Nov 1987. 43

[49] M J Woolley, C Lang, C Eichler, A Wallraff, and A Blais. Signatures of hong–ou–mandel interference at microwave frequencies. *New Journal of Physics*, 15(10):105025, oct 2013. 44, 45

[50] Kevin A Fischer, Kai Müller, Konstantinos G Lagoudakis, and Jelena Vučković. Dynamical modeling of pulsed two-photon interference. *New Journal of Physics*, 18(11):113053, nov 2016. 44

[51] D Moehring, Peter Maunz, S Olmschenk, Kelly Younge, Dzmitry Matsukevich, L.-M Duan, and C Monroe. Entanglement of single-atom quantum bits at a distance. *Nature*, 449:68–71, 10 2007. 55

[52] A. N. Craddock, J. Hannegan, D. P. Ornelas-Huerta, J. D. Siverns, A. J. Hachtel, E. A. Goldschmidt, J. V. Porto, Q. Quraishi, and S. L. Rolston. Quantum interference between photons from an atomic ensemble and a remote atomic ion. *Physical Review Letters*, 123(21), nov 2019. 55

[53] W. Dür, H.-J. Briegel, J. I. Cirac, and P. Zoller. Quantum repeaters based on entanglement purification. *Physical Review A*, 59(1):169–181, jan 1999. 55

[54] Yoshiaki Tsujimoto, Kentaro Wakui, Mikio Fujiwara, Masahide Sasaki, and Masahiro Takeoka. Ultra-fast hong-ou-mandel interferometry via temporal filtering. *Optics Express*, 29(23):37150, oct 2021. 55

[55] Ruibo Jin, Thomas Gerrits, Mikio Fujiwara, Ryota Wakabayashi, Taro Yamashita, Shigehito Miki, Hirotaka Terai, Ryosuke Shimizu, Masahiro Takeoka, and Masahide Sasaki. Spectrally resolved hong-ou-mandel interference between independent sources. *Optics Express*, 23, 07 2015. 55

[56] M. Meraner, A. Mazloom, V. Krutyanskiy, V. Krcmarsky, J. Schupp, D. A. Fioretto, P. Sekatski, T. E. Northup, N. Sangouard, and B. P. Lanyon. Indistinguishable photons from a trapped-ion quantum network node. *Physical Review A*, 102(5), nov 2020. 57

[57] Jens L Sørensen, Ditte Møller, Theis Iversen, Jakob B Thomsen, Frank Jensen, Peter Staanum, Dirk Voigt, and Michael Drewsen. Efficient coherent internal state transfer in trapped ions using stimulated raman adiabatic passage. *New Journal of Physics*, 8(11):261–261, nov 2006. 57

[58] Thomas Legero, Tatjana Wilk, Markus Hennrich, Gerhard Rempe, and Axel Kuhn. Quantum beat of two single photons. *Phys. Rev. Lett.*, 93, August 2004. 60

[59] H. P. Specht, J. Bochmann, M. Mücke, B. Weber, E. Figueroa, D. L. Moehring, and G. Rempe. Phase shaping of single-photon wave packets. *Nature Photonics*, 3(8):469–472, jul 2009. 62

[60] Peter B R Nisbet-Jones, Jerome Dilley, Daniel Ljunggren, and Axel Kuhn. Highly efficient source for indistinguishable single photons of controlled shape. *New Journal of Physics*, 13(10):103036, oct 2011. 62

[61] Valerio Scarani, Helle Bechmann-Pasquinucci, Nicolas J. Cerf, Miloslav Duš ek, Norbert Lütkenhaus, and Momtchil Peev. The security of practical quantum key distribution. *Reviews of Modern Physics*, 81(3):1301–1350, sep 2009. 63

[62] Fadri Grünenfelder, Alberto Boaron, Davide Rusca, Anthony Martin, and Hugo Zbinden. Simple and high-speed polarization-based QKD. *Applied Physics Letters*, 112(5):051108, jan 2018. 63

[63] G B Xavier, N Walenta, G Vilela de Faria, G P Temporã o, N Gisin, H Zbinden, and J P von der Weid. Experimental polarization encoded quantum key distribution over optical fibres with real-time continuous birefringence compensation. *New Journal of Physics*, 11(4):045015, apr 2009. 63

[64] Jörg-Peter Elbers, Christoph Glingener, M. Duser, and E. Voges. Modelling of polarisation mode dispersion in singlemode fibres. *Electronics Letters*, 33:1894 – 1895, 11 1997. 63

[65] Shuang Wang, Wei Chen, Jun-Fu Guo, Zhen-Qiang Yin, Hong-Wei Li, Zheng Zhou, Guang-Can Guo, and Zheng-Fu Han. 2 GHz clock quantum key distribution over 260 km of standard telecom fiber. *Optics Letters*, 37(6):1008, mar 2012. 63

[66] Nurul T. Islam, Charles Ci Wen Lim, Clinton Cahall, Jungsang Kim, and Daniel J. Gauthier. Provably secure and high-rate quantum key distribution with time-bin qudits. *Science Advances*, 3(11), nov 2017. 63

[67] Alberto Boaron, Boris Korzh, Raphael Houlmann, Gianluca Boso, Davide Rusca, Stuart Gray, Ming-Jun Li, Daniel Nolan, Anthony Martin, and Hugo Zbinden. Simple 2.5 GHz time-bin quantum key distribution. *Applied Physics Letters*, 112(17):171108, apr 2018. 63

[68] A. Alarcó n, J. Argillander, G. Lima, and G.B. Xavier. Few-mode-fiber technology fine-tunes losses in quantum communication systems. *Physical Review Applied*, 16(3), sep 2021. 63, 64

[69] Ilaria Vagniluca, Beatrice Da Lio, Davide Rusca, Daniele Cozzolino, Yunhong Ding, Hugo Zbinden, Alessandro Zavatta, Leif K. Oxenløwe, and Davide Bacco. Efficient time-bin encoding for practical high-dimensional quantum key distribution. *Physical Review Applied*, 14(1), jul 2020. 64

[70] Peter B R Nisbet-Jones, Jerome Dilley, Annemarie Holleczek, Oliver Barter, and Axel Kuhn. Photonic qubits, qutrits and ququads accurately prepared and delivered on demand. *New Journal of Physics*, 15(5):053007, may 2013. 64, 65, 75